

AD-A285 090



0

SHOTGUN/DROP-WEIGHT INITIATION OF ENERGETIC MATERIALS

FINAL REPORT

---

K.P. Duffy, J.E. Miller and A.M. Mellor

June 30, 1994

U.S. ARMY RESEARCH OFFICE

CONTRACT DAAL03-89-K-0061

COMBUSTION AND PROPULSION GROUP  
VANDERBILT UNIVERSITY



DTIC QUALITY INSPECTED

APPROVED FOR PUBLIC RELEASE;  
DISTRIBUTION UNLIMITED

11485 94-30963

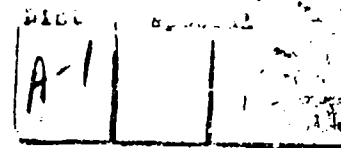


94 3 2

3

# SECTION 1.0 TABLE OF CONTENTS

<u>Section</u>	<u>Page</u>
1.0 Table of Contents	1-1
2.0 List of Figures and Tables	2-1
3.0 Acknowledgements	3-1
4.0 Statement of Problem Studied / Background	4-1
4.1 General	4-1
4.2 Review of Drop-Weight Program	4-3
4.3 Past Shotgun Test Methods	4-6
5.0 Vanderbilt Shotgun Impact Experiment	5-1
5.1 Experimental Apparatus	5-1
5.1.1 Anvil and Mounting System	5-1
5.1.2 Projectile Characteristics	5-4
5.1.3 Propellant Sample Characteristics	5-4
5.1.4 Stress Measurement	5-5
5.1.5 Laser Obscuration System	5-6
5.1.6 Detection of Reaction	5-8
5.1.7 Data Acquisition System	5-8
5.2 Finite Element Model of the Shotgun Test	5-10
5.2.1 Stress Wave Propagation	5-12
5.2.2 Stress Correlations	5-14
5.2.3 Energy Distribution	5-16
5.2.4 Stress Localization	5-22
5.3 Experimental Results	5-26
5.3.1 Capabilities of the Laser Obscuration System	5-26
5.3.1.1 Spacing Constraints	5-26
5.3.1.2 Beam Divergence	5-29
5.3.1.3 Non-Parallel Surfaces	5-32
5.3.1.4 Beam Transmission Measurements	5-32
5.3.1.5 Chopper Wheel Calibrations	5-35



5.3.2	PVDF Stress and Reaction Intensity Results	5-45
5.3.2.1	Inert Samples at $V_0 \approx 150$ m/s	5-47
5.3.2.2	Inert Samples at $V_0 \approx 200$ m/s	5-52
5.3.2.3	Arcadene-360 Propellant at $V_0 \approx 150$ m/s	5-54
5.3.2.4	Arcadene-360 Propellant at $V_0 \approx 200$ m/s	5-54
5.3.2.5	P3 Baseline Research Propellant at $V_0 \approx 150$ m/s	5-55
5.3.2.6	P3 Baseline Research Propellant at $V_0 \approx 200$ m/s	5-55
5.3.2.7	P8 Research Propellant at $V_0 \approx 150$ m/s	5-55
5.3.2.8	P8 Research Propellant at $V_0 \approx 200$ m/s	5-56
5.3.2.9	Stress Gauge Correlations	5-56
5.3.3	Critical Energy Calculations	5-56
5.3.4	Summary of Important Results	5-65
5.3.5	Future Design Recommendations	5-66
6.0	List of Publications and Technical Reports	6-1
7.0	List of Participating Scientific Personnel and Degrees Awarded	7-1
8.0	List of Reportable Inventions	8-1
9.0	References	9-1
<u>Appendices</u>		
A	Test Bay Dimensions	A-1
B	Determination of Face Length and Centerline Beam Spacing	B-1
C	Stress and Reaction Histories	C-1
D	Derivation of Velocity from Stress History	D-1
E	Form SF298	E-1

## SECTION 2.0

### LIST OF FIGURES AND TABLES

<u>Figure</u>	<u>Page</u>
4.1 Schematic of spring loaded impact machine.	4-5
4.2 A 17.5 mm diameter by 18.5 mm long propellant cylinder is fired at an impact plate enclosed by a catch box (Gould, 1980).	4-7
4.3 A 17 mm diameter by 20 mm long propellant cylinder is fired at an impact plate. Light intensity-time and pressure-time profiles are obtained for velocities ranging from 180 to 370 m/s (Ho et al., 1989).	4-8
4.4 A 17 mm diameter by 20 mm long projectile is fired at an impact plate. A Cordin camera photographs the motion of the propellant, and blast pressure-time data are obtained. Velocity range is 670 to 1000 m/s (Jensen et al., 1981).	4-9
4.5 A PMMA projectile is fired at the propellant sample located on an anvil. Note the anvil is designed to absorb some of the impact by breaking away along the dotted lines. Velocity range is 50 to 225 m/s (Coffey et al., 1986).	4-10
5.1 Experimental arrangement for the shotgun impact test.	5-2
5.2 Anvil schematic for shotgun impact test.	5-3
5.3 Schematic of laser obscuration system.	5-7
5.4 Data acquisition circuitry for a) tests on inert samples and b) tests on live propellants.	5-9
5.5 Axisymmetric finite element mesh of shotgun test including enlarged propellant sample region.	5-11
5.6 Contour plots of von Mises stress at a) 10 $\mu$ s, b) 38 $\mu$ s, and c) 72 $\mu$ s.	5-13
5.7 Axial stress at the anvil surface for slideline a) Type 1 and b) Type 4.	5-17
5.8 Location of elements used in strain energy calculations for a) sample and b) PMMA projectile.	5-19
5.9 Calculated energy values for 100 m/s impact.	5-20
5.10 Deformation of sample mesh at three different times showing penetration between projectile and sample surfaces at 90 $\mu$ s ( $V_0 = 100$ m/s).	5-21
5.11 Calculated energy values for 150 m/s impact.	5-23
5.12 Calculated energy values for 50 m/s impact.	5-24

<u>Figure</u>		<u>Page</u>
5.13	Calculated energy values for 100 m/s impact on a smaller 6 mm long sample.	5-27
5.14	Optical components used to generate parallel beams.	5-28
5.15	Face length and centerline beam spacing as a function of incidence angle for three different spacers.	5-30
5.16	Parameters describing Gaussian beam characteristics (from Durst and Stevenson, 1977).	5-31
5.17	Beam diameter as a function of distance from waist location for waist diameters of a) 1.6 mm, b) 1.0 mm, and c) 0.5 mm. 500 mm corresponds to the approximate distance of the anvil surface from the laser aperture.	5-33
5.18	Resulting beam spacing if the spacer surfaces are not parallel.	5-34
5.19	Symbols corresponding to beam transmission measurements.	5-36
5.20	Schematic of chopper wheel used in laser obscuration calibration.	5-37
5.21	Calibration traces for three different chopper wheel rotation speeds.	5-39
5.22	Typical obscuration trace indicating data reduction method.	5-40
5.23	Raw data from chopper wheel calibration test at medium rotation speed.	5-42
5.24	Raw data from chopper wheel calibration test at maximum rotation speed.	5-44
5.25	Schematic of a split Hopkinson pressure bar (from Follansbee and Frantz, 1983).	5-46
5.26	Laser obscuration trace for shotgun impact at 153 m/s (case a217) indicating a planar impact.	5-48
5.27	Alignment of laser beams with reference to the top of the projectile.	5-49
5.28	Laser obscuration trace for shotgun impact (case d217) indicating an oblique impact.	5-50
5.29	Schematics of desired and tilted impacts. The latter results in an incomplete obscuration signal as in Fig. 5.28.	5-51
5.30	Typical calculated energy distribution (case f47).	5-59
5.31	Composite of all three signals shifted in time.	5-60

<u>Figure</u>	<u>Page</u>
5.32 Correlation of stress density and light intensity for all propellant data.	5-63
5.33 Correlation of stress density and light intensity for cases where reaction occurs before peak stress level is reached.	5-64
A-1 Diagram of test bay for shotgun impact. All dimensions in inches.	A-2
B-1 Close-up of optics indicating relevant lengths and angles for determining face length and centerline beam spacing.	B-2
C-1 Stress histories for inert samples at $\approx 150$ m/s.	C-3
C-2 Stress histories for inert samples at $\approx 200$ m/s.	C-3
C-3 Light traces for Arcadene-360 samples at $\approx 150$ m/s.	C-4
C-4 Stress histories for Arcadene-360 samples at $\approx 150$ m/s.	C-5
C-5 Light traces for Arcadene-360 samples at $\approx 200$ m/s.	C-6
C-6 Stress histories for Arcadene-360 samples at $\approx 200$ m/s.	C-7
C-7 Light traces for P3 samples at $\approx 150$ m/s.	C-8
C-8 Stress histories for P3 samples at $\approx 150$ m/s.	C-9
C-9 Light traces for P3 samples at $\approx 200$ m/s.	C-10
C-10 Stress histories for P3 samples at $\approx 200$ m/s.	C-11
C-11 Light traces for P8 samples at $\approx 150$ m/s.	C-12
C-12 Stress histories for P8 samples at $\approx 150$ m/s.	C-13
C-13 Light traces for P8 samples at $\approx 200$ m/s.	C-14
C-14 Stress histories for P8 samples at $\approx 200$ m/s.	C-15

<u>Table</u>	<u>Page</u>
5.1 Propellants tested in shotgun impact experiment.	5-5
5.2 Laser obscuration system information.	5-8
5.3 Material constants used in DYNA2D model.	5-12
5.4 Summary of stress correlations.	5-14

<u>Table</u>	<u>Page</u>
5.5 Strain energy density values (dyne/cm <sup>2</sup> ).	5-25
5.6 Beam transmission measurements.	5-35
5.7 Data corresponding to Fig. 5.22. $V_0 = 3.45$ m/s.	5-41
5.8 Data corresponding to Fig. 5.23. $V_0 = 8.3$ m/s.	5-41
5.9 Data corresponding to Fig. 5.24. $V_0 = 66.2$ m/s.	5-43
5.10 Summary of inert and Arcadene-360 cases.	5-53
5.11 Summary of research propellant cases.	5-53
5.12 Summary of energy calculations.	5-61

### SECTION 3.9

#### ACKNOWLEDGEMENTS

Appreciation is due to Dave Mann of the Army Research Office who provided the funding for this study. Robert Pitz of Vanderbilt and Don Johnson of KTECH provided valuable technical support. Pat Baker was instrumental in many technical aspects of the experiment. Vanderbilt undergraduates Jason Seay and Dave Everson performed much of the preliminary shotgun test design via finite element modeling. Appreciation also goes out to L.B. Thorn and Dave Dreitzler at U.S. Army MICOM for providing the laboratory space and loaning much of the equipment for the experiments. Additional support from the following people at MICOM is also greatly appreciated: Millard Snow, Robert Milton, Anita Swearingen, Eric Herring, Robert Sewada, David Huckaby, and Mike Bush. Finally, Myrna Martin assisted tremendously in preparing the interim technical reports and this final report.





## SECTION 4.0

### STATEMENT OF PROBLEM STUDIED / BACKGROUND

During the past 30 years, numerous military accidents have resulted in the loss of millions of dollars and, more importantly, thousands of lives. Thus, the design of low vulnerability munitions is important to all branches of the Armed Services. The importance is twofold: (1) to improve munition survivability, and (2) to reduce the possibility of accidental initiation. In 1985 the Department of Defense instituted the Insensitive Munitions (IM) Program (Mellor et al., 1988) which requires that all munitions pass several standardized tests by 1995 (Maykut, 1991). In several of these tests the munition is faced with a stimulus that is at least in part mechanical: e.g., shaped charge jet impact, bullet impact, multiple fragment impact, or sympathetic detonation. As a preliminary to these IM tests, small-scale screening tests are conducted on the energetic materials during the munition development phase.

A desirable feature of any screening test is applicability of the results to actual scenarios. One impact sensitivity test, the critical initiation energy drop-weight impact test, measures the work required to cause a reaction in an energetic material sample of mass 35–50 mg; the impact velocity is on the order of 10 m/s. A recently completed companion program funded by the Army Research Office applied this test to solid rocket propellants (Baker, 1994). Coffey et al. (1986) showed that when normalized by the sample mass, critical initiation energy is of the same order for a shotgun test with impact velocities greater than 100 m/s. However, experiments by Baker et al. (1990) and recent modeling by Baker and Mellor (1992) show that for some materials critical energy may indeed be a function of impact velocity. The results presented here are primarily for the one-year extension to the aforementioned drop-weight program. A shotgun impact test was used in concert with the previous drop-weight work to explore propellant response for an order of magnitude increase in impact velocity.

#### 4.1 General

In order to relate small-scale tests (such as the drop-weight impact or shotgun experiments) to real world scenarios, a quantitative determination of both the stimulus to, and response of, the energetic material is required. The tests examined in the present program can be applicable to bullet and fragment impact hazards if the correct data are measured and proper interpretation is achieved. Maximum desired impact velocities in the shotgun test (50 to 450 m/s) approach those of bullet and fragment impacts, and the small sample sizes in critical energy drop-weight impact tests cause strain rates  $> 10^4 \text{ s}^{-1}$ .

The drop-weight machine has been used as a screening tool for many years. Usually the 50% go/no go method is used for sensitivity analysis; the required drop height,  $H_{50}$ , to cause a reaction in 50% of the samples is recorded. Unfortunately, rankings for explosives from various

laboratories do not always agree, even when the same impact machine is used (e.g., Roth, 1975). Some variability in existing data can be explained by operator judgment of the various "go" criteria which are used, such as visible light, audible detection, or the presence of smoke. Also humidity and temperature are known to affect  $H_{50}$  results (Coffey and DeVost, 1986). However, the largest cause of variability is the machine dynamics: significant elastic energy deposited in the machine makes a quantitative sensitivity ranking impossible (Coffey et al., 1986). Coffey et al. (1986) proposed increasing the drop-weight impact velocity so that the effective drop height is well above  $H_{50}$  and the reaction probability approaches 100%. This allows one to neglect elastic energy deposited in the machine and directly determine the work on the sample by measuring the drop-weight kinetic energy change as a function of time. This work at the time of sample reaction is called the critical initiation energy. After impact on the sample and prior to reaction, an energy balance on the system gives

$$0 = \Delta E_{w,k} + \Delta E_{w,e} + \Delta E_{a,k} + \Delta E_{a,e} + \Delta E_{s,k} + W_s \quad (4.1)$$

Here  $\Delta E_{w,k}$ ,  $\Delta E_{a,k}$ , and  $\Delta E_{s,k}$  are the kinetic energy changes of the drop weight, anvil and sample, respectively;  $\Delta E_{w,e}$  and  $\Delta E_{a,e}$  are the elastic strain energies stored in the drop weight and anvil; and  $W_s$  is the work done on the sample.

For the materials tested by Coffey et al. (1986), the sample kinetic energy was negligible, and Baker and Mellor (1992) showed that even for a low friction case, the sample kinetic energy change is less than 8% of the sample work. The elastic energy of the machine is negligible when the drop-weight velocity change is small relative to its impact velocity (Coffey et al., 1986; Baker et al., 1990). Similarly, the anvil kinetic energy is also small when the velocity change is small. Thus, the critical energy  $E_c$  is

$$E_c = W_s = -\Delta E_{w,k} = -M_w (V_0 \Delta V + \frac{1}{2} \Delta V^2) \quad (4.2)$$

where  $M_w$  is drop-weight mass,  $V_0$  is the impact velocity,  $\Delta V$  (a negative value) is the drop-weight velocity change from impact to the first detectable chemical reaction, and  $|\Delta V| \ll V_0$ .

Critical energy is a quantitative measure of the stimulus applied to the energetic material. The critical energy drop-weight impact test was the main focus of the research program described in complete detail in Baker (1994). A brief review of those results is now presented. The method by which the critical energy is transferred to heat and the localization of heat into hot spots leading to initiation were subjects of research for that program since knowledge of the initiation mechanism is essential for application of critical energies to other scenarios.

## 4.2 Review of Drop-Weight Program

The previous research program entitled "Drop Weight Impact Initiation of Energetic Materials" was divided into three phases: experimental, analysis of experiment, and analysis of experimental data. A complete list of all publications and technical reports related to this work is given in Section 6. The objectives of the research were to: (1) use finite element calculations along with engineering analysis of test results to develop a fundamental understanding of deformation and ignition processes in drop-weight impact, (2) obtain a datum base of critical initiation energies for systematic variations of propellant formulations and environmental parameters, (3) compare critical initiation energy and 50% go/no go results to determine the better method of predicting impact sensitivity, (4) document the growth of reaction to ignition via microscopy of quenched samples, (5) examine the relation of the drop-weight test to other scenarios, e.g., Hopkinson bar and bullet and fragment impact. In the experimental phase, the effects of propellant formulation, sample size, and anvil friction were studied. The analytical modeling focused on temperature effects, boundary conditions, material property variations, and hot spot models. The model was capable of predicting trends in critical energy density using a critical temperature criterion and a frictional heating mechanism at the sample-machine interfaces.

The drop-weight test finite element modeling was conducted using the code DYNA2D (Hallquist, 1982). The modeling was divided into two areas. (1) a homogeneous propellant model, and (2) an inhomogeneous propellant model in which differing amounts of ammonium perchlorate (AP) oxidizer particles were inserted in the binder matrix to more realistically model the propellant deformation behavior. The results from (1) verified that parametric studies on important code inputs are essential in order to develop understanding of the results. Significant effects on the resulting sample stress state from changing the propellant mechanical properties were also found. If particles were included in the propellant model, the resulting stress state was significantly different from the homogeneous representation. Modeling restrictions posed by the default axisymmetric and alternative plane strain geometry were also discussed.

A set of research propellants designed specifically for the drop-weight program was formulated by the Atlantic Research Corporation (ARC). Mechanical properties tests were conducted on these propellants at ARC. Standard JANNAF tensile tests at 21° C and compression tests at 21 and -40° C were conducted. These results are indicated in Baker (1994). Approximately 0.227 kg (1/2 lb) of each of these propellants was available for testing.

Experimental results were obtained in two areas. First, critical energy tests were conducted at the Naval Surface Warfare Center (NSWC) under the direction of co-Principal investigator Coffey (see Baker et al., 1990). The results presented in this paper were attributed mainly to the changes in formulational variables among the propellants tested. However, later experimental drop-weight results indicated that friction plays an important role in this test. Second, a spring-loaded impact machine which uses different instrumentation was designed and

constructed and used for the majority of the tests at U.S. Army Missile Command (MICOM).

One of the goals of this research was to develop an experiment which could measure critical energy and reaction severity as a function of stimulus level. A schematic of the spring-loaded impact machine designed to accomplish this goal is shown in Fig. 4.1. The machine has an enclosed volume of approximately 5000 cm<sup>3</sup>. The maximum pressure expected from combustion of a 35 mg propellant sample in this chamber is less than 3 atm. The drop weight is steel and weighs  $\approx$  370 g. The spring used in the machine gives a maximum drop-weight impact velocity of  $> 15$  m/s. The steel anvil is 7.68 cm high, and rests on a 2.54 cm thick steel plate. Three photosensors are positioned in line with the top of the anvil in windows on the base of the machine. With these, light emission is detected from the sample when initiation occurs. A pressure transducer is connected to the side of the spring-loaded machine, and the machine is sealed off from the environment. In this way, the severity of the reactor could be determined. However, due to the large volume, it was not possible to examine the reaction growth.

The NSWC machine used previously to obtain data had an accelerometer mounted on the drop weight to monitor velocity as the sample deformed. Unfortunately, after initially designing the drop-weight machine, experimental results showed that accelerometers could not withstand multiple impacts at the desired velocities for the critical energy tests. Thus, the spring loaded machine was modified to use a different method to measure the drop-weight velocity following impact. Polyvinylidene fluoride (PVDF) stress gauges were located under the anvil and in the drop weight.

The spring-loaded impact machine also provides a measurement of the impact velocity for each test, as opposed to calibrating the spring for impact velocity as a function of spring compression. The velocity is obtained by using light emitting and light detecting diodes in a fixed location in the machine.

The major conclusions from this work as summarized in Baker (1994) are as follows:

(1) The PVDF stress gauges are acceptable substitutes for accelerometers in drop-weight critical energy testing, but require calibration with accelerometers which is possible only in the lower velocity range.

(2) AP composite propellant initiation is controlled by the solids loading and more specifically the size of the largest AP particles. The initiation mechanism is attributed to frictional heating of these AP particles at specimen interfaces with the drop weight and anvil that leads to AP thermal decomposition and subsequent exothermic chemical reactions.

(3) Material stress-strain behavior did not significantly affect critical energy, but friction and sample geometry did.

(4) Calculated values of critical energy density were not minimum energies or ignition energies, but instead were deemed initiation energies (Baker, 1994).

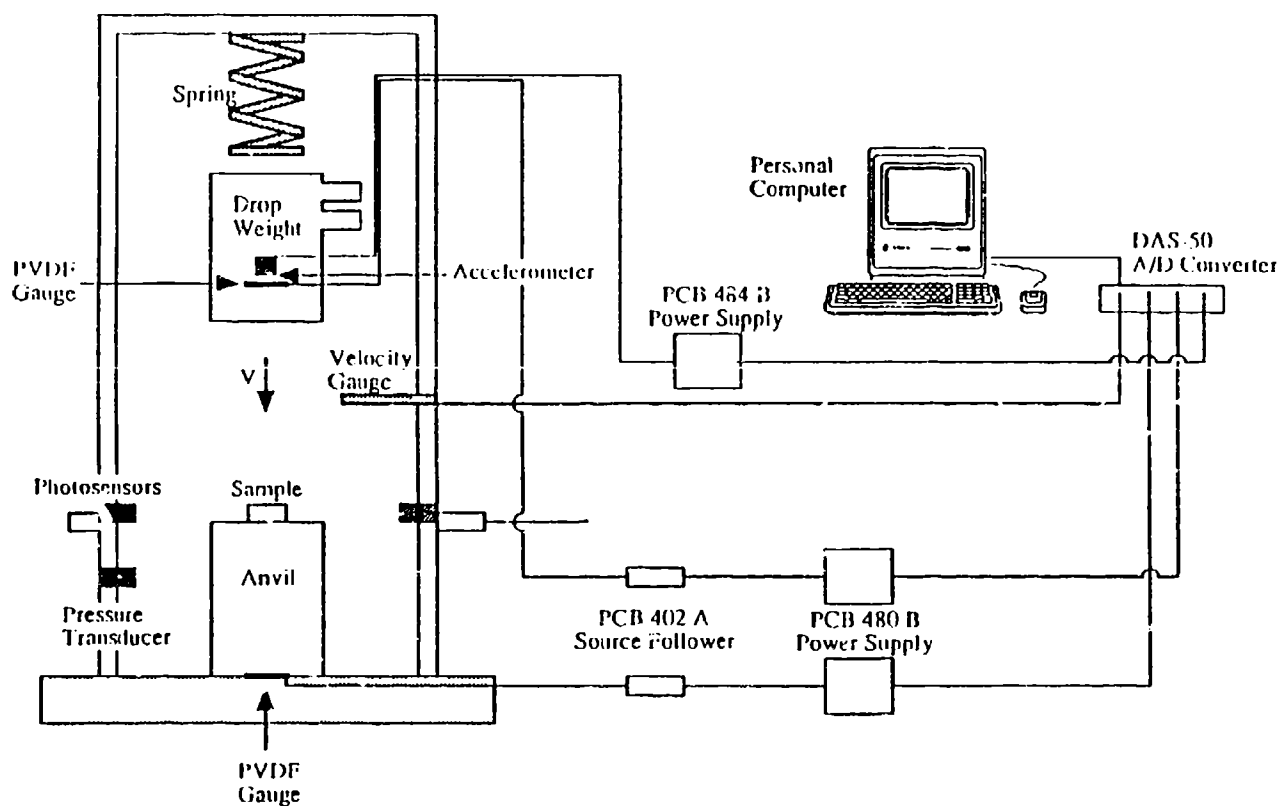


Figure 4.1. Schematic of spring loaded impact machine.

### 4.3 Past Shotgun Test Methods

Various shotgun tests have been employed to obtain a measure of propellant sensitivity. These past tests, with the exception of those performed by Coffey et al. (1986), have never been designed to measure the amount of energy required to cause a reaction. Ho et al. (1989) and Gould (1980) determined critical impact velocities and velocity thresholds for various degrees of reaction. Jensen et al. (1981) studied various reaction regimes, such as for shock-to-detonation and delayed detonation. Although these tests did not measure critical energy, the experimental arrangements were useful to examine.

All test methods except that of Coffey et al. (1986) employ a horizontally mounted shotgun, which fires a right circular cylinder of propellant onto an impact plate. In the Gould testing, the propellant cylinders fragmented upon impact, and the pieces were collected and burned in a combustion bomb. Using a piezoelectric pressure transducer, a pressure-time record of each test was used to determine the critical impact velocity (CIV) required to cause an initial  $dp/dt$  upon ignition in the bomb equal to that of a baseline propellant. CIV could then be utilized to rank the propellants tested with regard to friability. The experimental setup employed by Gould is shown in Fig. 4.2.

The major components of the Ho et al. shotgun test are a velocity-measuring system, light detectors, a force transducer, and a pressure transducer (Fig. 4.3). The visible emission intensity-time and pressure-time profiles for various propellants were measured in this test. For low velocity impacts, only a small peak was observed on the pressure and light intensity plots. As the impact velocity was increased, other reactions were noted, such as burning and explosions. Light intensity thus changed from a single peak to a peak followed by a broad region of high light intensity. The magnitude of the pressure peak was also found to increase at higher impact velocities. Ho et al. (1989) measured the critical impact velocity for ignition and initial burning (CV1) and for sustained burning and deflagration (CV2). The presence of a force transducer immediately behind the impact plate demonstrates that Ho et al. attempted some measurement of force or energy; however, no data from this gauge are presented in their paper.

Jensen et al. (1981) were mainly concerned with classifying three different types of reactions: deflagration, shock-to-detonation transition, and delayed detonation. The characteristics used to distinguish these reactions were impact velocity, resultant overpressure, time for decomposition of the sample, and damage inflicted to the target plate. As seen in Fig. 4.4, blast overpressure gages, a velocity measurement system, and a Cordin camera were the only instrumentation used in this test setup. Tests were also completed in which the propellant projectile first strikes a propellant disk suspended in front of the target plate. The motivation for these tests was to learn the effect of freshly damaged propellant on reaction rates and pressures.

The most applicable testing, for our purposes, was completed by Coffey et al. (1986). As shown in Fig. 4.5, in this apparatus, a shotgun aimed vertically downward fired a right circular

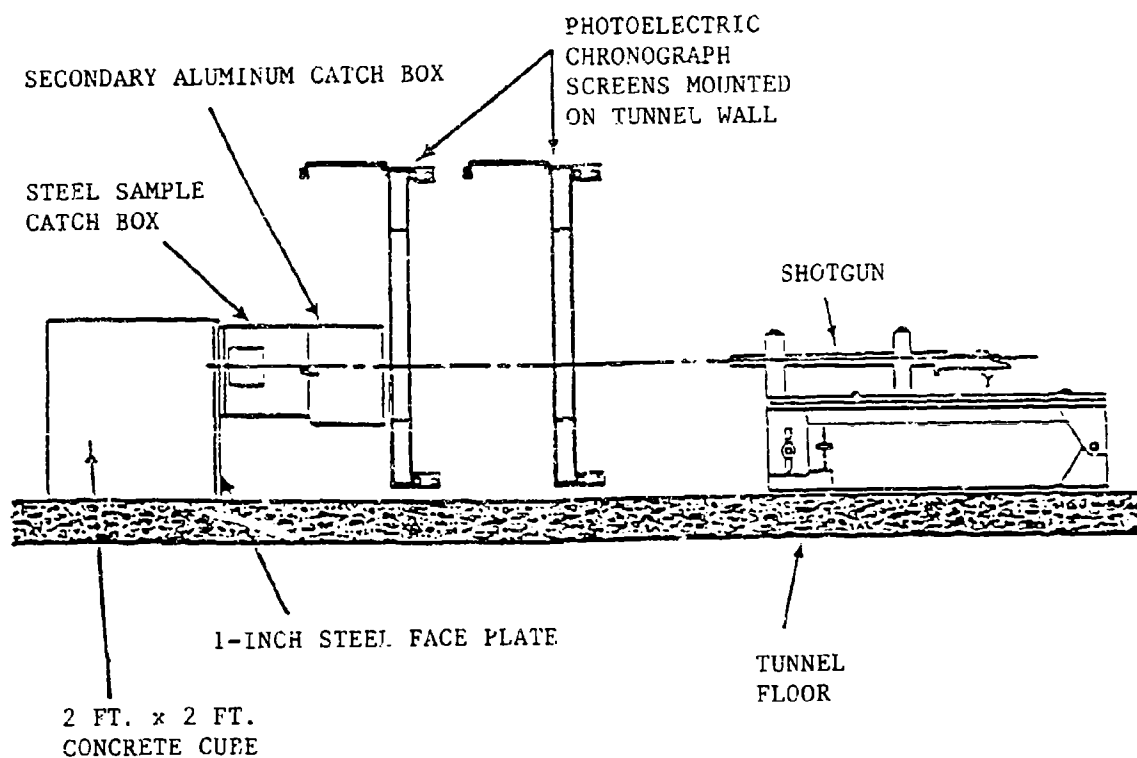


Figure 4.2. A 17.5 mm diameter by 18.5 mm long propellant cylinder is fired at an impact plate enclosed by a catch box (Gould, 1980).



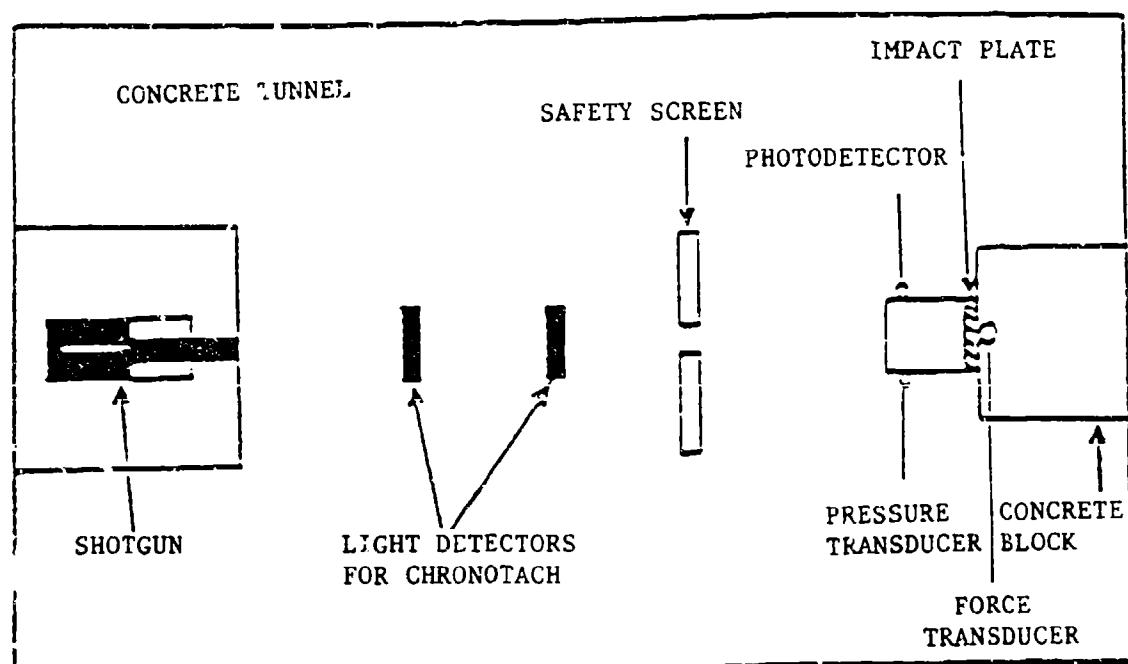


Figure 4.3. A 17 mm diameter by 20 mm long propellant cylinder is fired at an impact plate. Light intensity-time and pressure-time profiles are obtained for velocities ranging from 180 to 370 m/s (Ho et al., 1989).

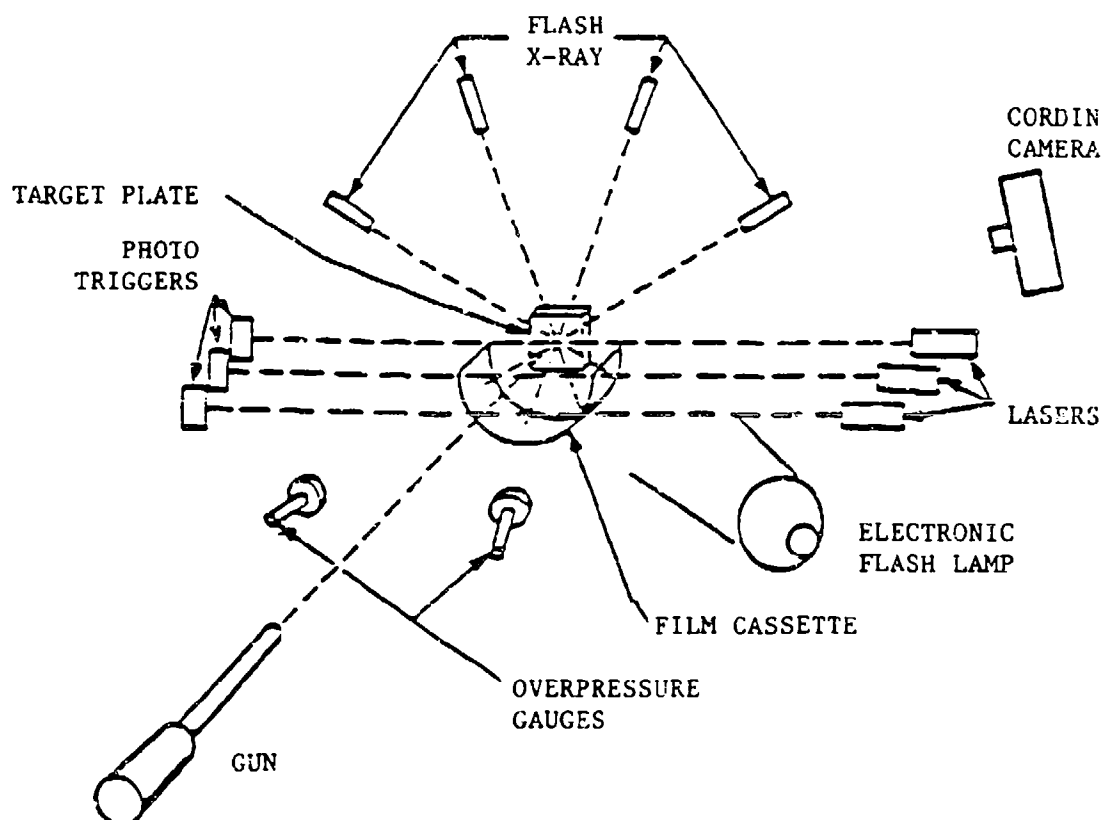


Figure 4.4. A 17 mm diameter by 20 mm long projectile is fired at an impact plate. A Cordin camera photographs the motion of the propellant, and blast pressure-time data are obtained. Velocity range is 670 to 1000 m/s (Jensen et al., 1981).

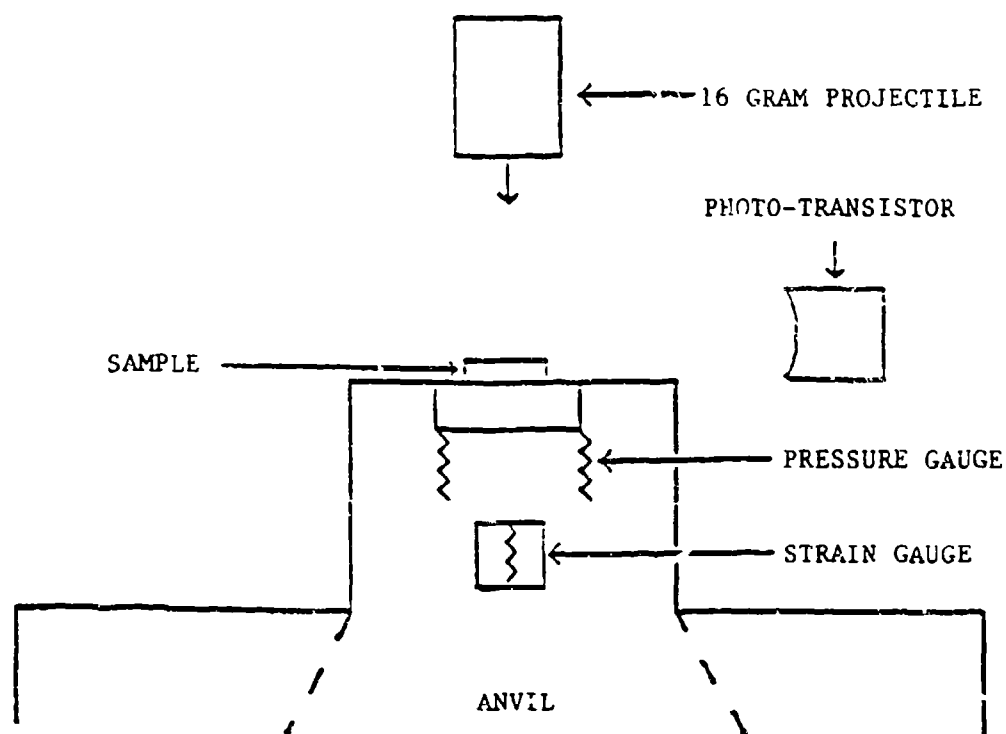


Figure 4.5. A PMMA projectile is fired at the propellant sample located on an anvil. Note the anvil is designed to absorb some of the impact by breaking away along the dotted lines. Velocity range is 50 to 225 m/s (Coffey et al., 1986).

cylinder of PMMA (Plexiglas) at a propellant sample resting on an anvil. The samples were thin wafers approximately 1 mm high and 5 mm in diameter, with sample masses ranging from 35 to 40 mg. In this test, first light was measured using a phototransistor with a rise time of 20 ns. Two strain gages, located on the sides of the anvil, and a fast response pressure gage located in the center of the anvil, measured the force and stress created by the impact. This stress was related back to the point of impact and used to determine the change in projectile velocity. Thus, critical energy could be calculated.

Because the velocities obtained in this testing were as high as 225 m/s, large loads are placed on the instrumentation. Therefore, a movable anvil system was designed to reduce the effects of the impact on the instrumentation. Upon impact, the force of the projectile pushed the anvil out of its base structure, thereby increasing the life of the pressure and strain gages.

Several improvements to the design in Fig. 4.5 were made in the present experiment. Due to the high velocities and small samples, reaction delay times after impact were as small as 2  $\mu$ s (Coffey et al., 1986), so all instrumentation required a time response on the order of ns in order to sufficiently represent the deformation process. However, the pressure and strain gages used by Coffey et al. (1986) had a time response only on the order of 1 to 2  $\mu$ s. It was also assumed that the elastic and plastic energy placed into the anvil and projectile, as well as the kinetic energy of the radially extruding sample, were negligible. Thus, following the discussion in Section 4.1, the critical energies given by Coffey et al. (1986) were computed using Eq. (4.2). Improvements to the critical energy calculation can be made by using the stress on the anvil to calculate the elastic anvil strain energy. The kinetic energy of the sample, which may be significant in the shotgun test, can also be computed, thus improving the estimate of work done on the sample.

Although funding was requested which would allow for testing of all the research propellants used in the drop-weight program, the available funds limited the overall scope of testing in the present program to three propellants. The performance of PVDF gages at higher velocities and the applicability of a new laser obscuration system designed specifically for the program are evaluated, and recommendations are made for a next generation design.



## SECTION 5.0

### VANDERBILT SHOTGUN IMPACT EXPERIMENT

The tests were performed at U.S. Army Missile Command in Huntsville, AL, in an outdoor test bay (Appendix A). A general description of the test is given first, and the individual components are discussed in detail in subsequent sections.

#### 5.1 Experimental Apparatus

Referring to Fig. 5.1, a 12-gauge Savage-Stevens single barrel shotgun is mounted vertically on a 0.0254 m (1") thick steel plate. Hard plastic (plexiglas) right circular cylinder projectiles are loaded in shotgun shells with varying amounts of gun powder. A small right circular cylinder of propellant is placed on a steel anvil in the line of the gun. A 110 V heavy-pull solenoid activates the trigger which fires the gun. To measure the projectile velocity, a laser obscuration system is used. The receiving optics are placed on a table to the left of the anvil. After impact, the sample and projectile are completely destroyed. Stress is measured with a PVDF gauge mounted midway down the anvil, and a photodiode determines the onset and severity of reaction of the various propellant samples tested. Numerous vibration dampening and safety features are also implemented.

From the data obtained, the relative severity of sample reaction as a function of propellant type and impact velocity is determined, and the critical energy is calculated. Also, the repeatability of the PVDF gauge output is examined, and the performance of the new laser obscuration system is evaluated.

##### 5.1.1 Anvil and Mounting System

The anvil design is a homogeneous right circular cylinder. Other anvil designs such as a two material anvil, a conical anvil, and a stepped anvil were evaluated using finite element analysis. All of these designs were rejected based on the results (Everson and Seay, 1992). When dimensioning the anvil, the major concerns included stresses at the impact surface, stresses at the gauges, anvil stability, and data interpretation.

Other than material, which was chosen so the anvil does not yield, the most significant design parameter was the cylinder diameter. The anvil diameter must be greater than the projectile diameter, and the stress at the PVDF gauge location must be less than the maximum load the instrumentation can handle.

The 0.0508 m (2") diameter anvil (Fig. 5.2) is constructed of 4140 steel heat treated to a Rockwell hardness of 55. The two 0.3048 m (12") sections are bolted at the flanges to allow for insertion/removal of the stress gauge. All flat ends were ground extremely smooth. A

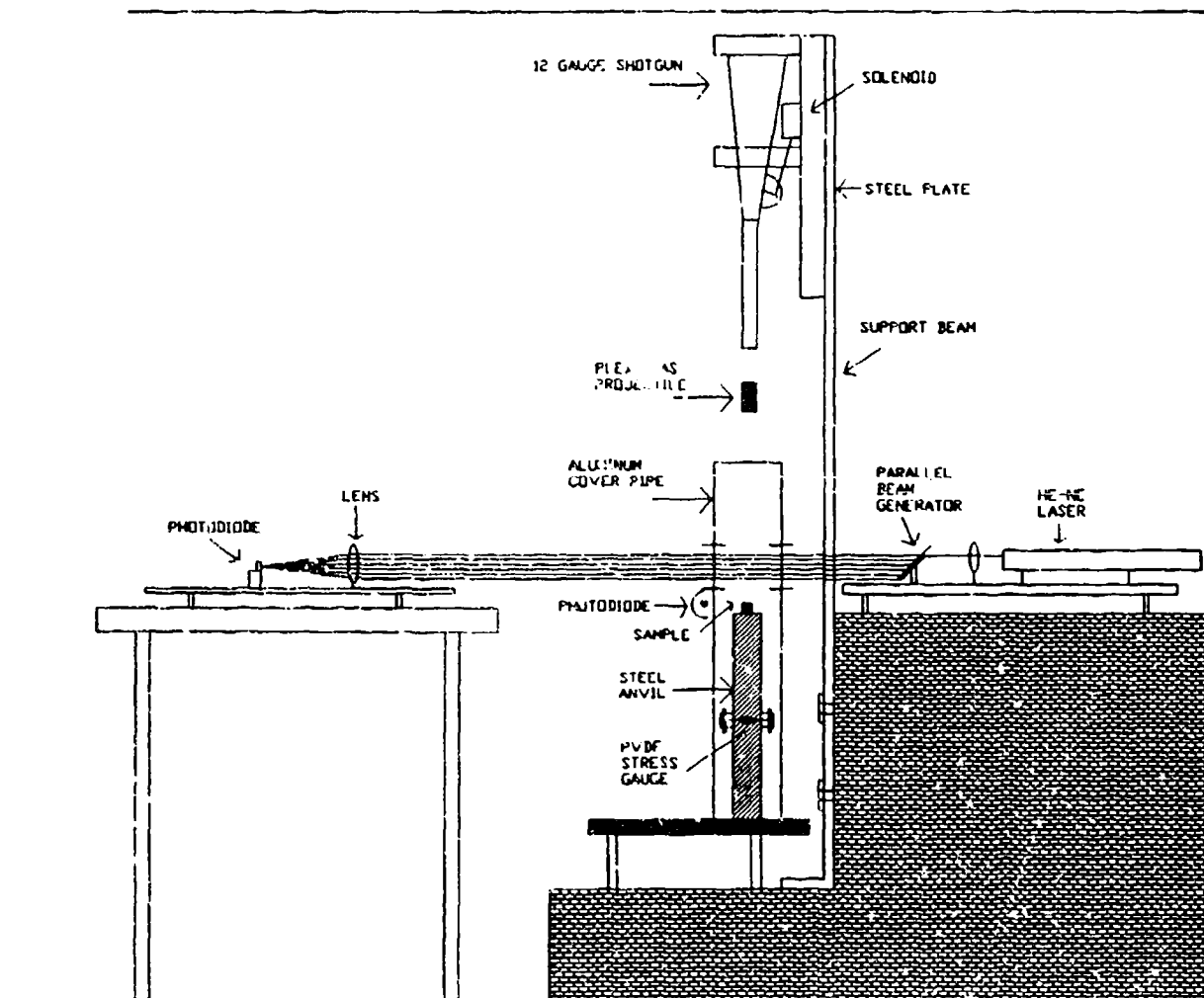


Figure 5.1. Experimental arrangement for the shotgun impact test.

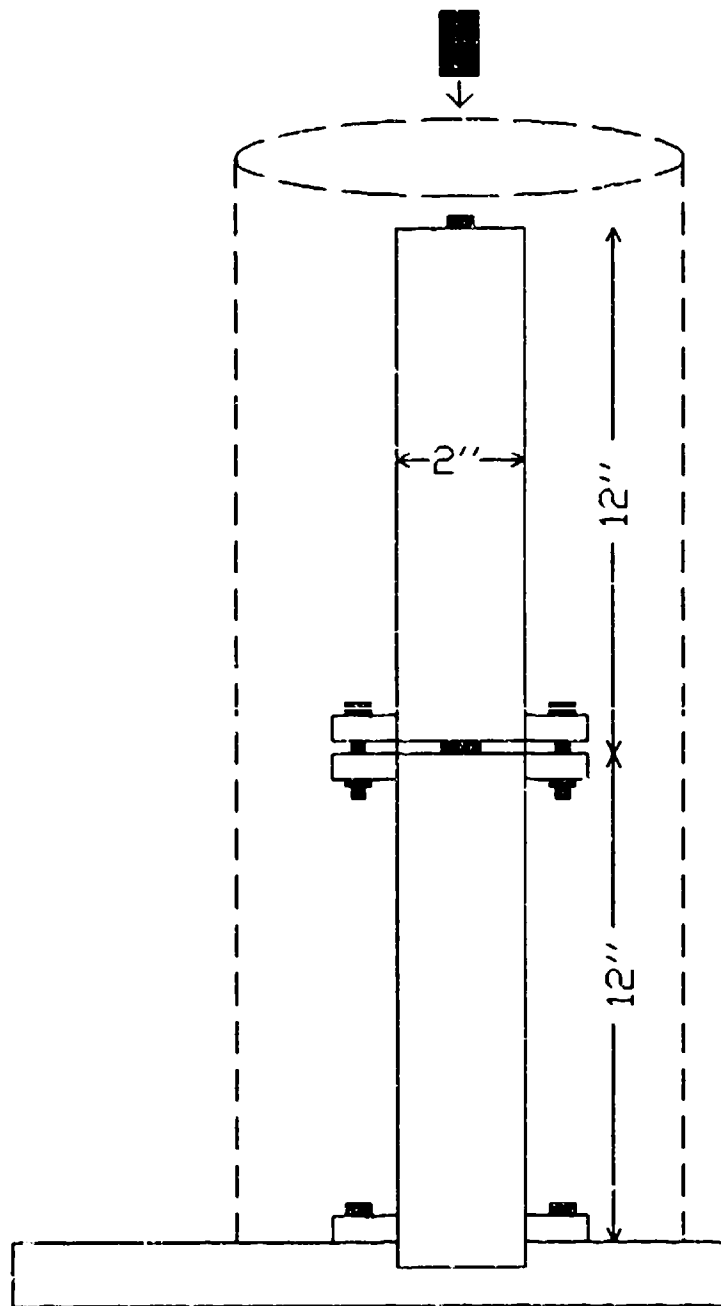


Figure 5.2. Anvil schematic for shotgun impact test.



conflicting design concern stemmed from elastic wave propagation. It is desired to accurately determine the impact stress from the stresses recorded by the PVDF gauge. This is accomplished if the pressure waves in the anvil are nearly one-dimensional. The anvil dimensions are chosen to accomplish this goal as shown later in the modeling discussion. The length of the bottom section was chosen to prevent vibrations from returning to the gauge location during the anticipated ignition delay times. This section is welded and bolted to a 0.0254 m (1") thick steel base plate for stability and stress wave dispersion.

#### **5.1.2 Projectile Characteristics**

The projectiles are machined from polymethyl methacrylate (PMMA) and have a length of 50.8 mm (2") and a diameter of 17.46 mm (11/16"). PMMA provides a low yield strength material when compared to steel thereby reducing the stresses placed on the anvil by a high velocity impact. Each projectile is loaded in a 12-gauge shotgun shell with differing amounts of gun powder (7X brand), and a modified wad is used to contain the high pressure combustion products once ignited, thus permitting higher projectile velocities. A smooth coating of flat black spray paint is applied to the radial surface of the projectile to block the laser beams in the obscuration system. An initial powder-velocity relation was obtained for a velocity range of 50-450 m/s. However, subsequent tests revealed the projectiles shatter in the gun barrel at velocities greater than approximately 150 m/s, thus setting an upper bound on the obtainable test velocities.

#### **5.1.3 Propellant Sample Characteristics**

The desired initiation time has the greatest influence on choice of sample size. Recall that the Coffey et al. (1986) test, which is similar to this test, used 1 mm thick wafers, and initiation times of  $\approx 2 \mu\text{s}$  resulted. The original plan called for cylindrical samples approximately 12 mm long and 10 mm in diameter which would result in reasonably longer ignition delay times and not require ultra-fast instrumentation. Simple linear scaling would imply that a delay of  $\approx 25 \mu\text{s}$  will be obtained with a 12 mm length sample. However, the scaling is most likely non-linear since the PMMA projectile is slowed as it deforms the 12 mm sample. Also, the sample diameter is increased to 10 mm, compared to the Coffey et al. 5 mm, suggesting a reaction delay on the order of 50  $\mu\text{s}$  for the Coffey et al. (1986) maximum reported impact velocity of  $\approx 225 \text{ m/s}$ .

Accordingly, all calibrations were performed using inert samples with approximately these dimensions. The inert was an HTPB binder containing carbon, salt, or ammonium sulfate to simulate proprietary Army formulations (MLRS, Patriot, etc.) so the exact constituents are not known.

The tests on live propellants were conducted with three different formulations: Arcadene-360 (made available by MICOM) and two research propellants used in the drop weight tests of Baker (1994). The relevant and known formulational variables are listed below in Table 5.1. Due to time and cost constraints other variations in test operation were not attempted, such as using a sabot (Jensen et al., 1981) to fire a propellant cylinder from the shotgun or attaching a propellant sample to a projectile with glue or adhesive and firing both the projectile and propellant together.

Table 5.1. Propellants Tested in Shotgun Impact Experiment

Propellant	Polymer	Weight %	Solids	Weight %
Arcadene-360 <sup>1</sup>	HTPB (R-45M)	≈10	AP Al	≈87
P3	HTPB (R-45M)	39.5	AP (200 μm)	60
P8	HTPB (R-45M)	14.5	AP (200 μm, 60%/ 20 μm, 25%)	85

<sup>1</sup>Remaining constituents consist of plasticizer, cure catalysts, and a burn rate catalyst (Fe<sub>2</sub>O<sub>3</sub>).

#### 5.1.4 Stress Measurement

As in the drop weight tests, a PVDF stress gauge is used to measure the axial stress. The gauge is mounted at the midlength of the anvil and consists of sputtered gold over platinum electrodes on a biaxially stretched piezoelectric polymer. Time response is on the order of nanoseconds. These PVDF sensors are often used in single shot experiments and can record stresses in the gigapascal range. For these tests, they are reusable at stresses up to approximately 70 MPa and should perform adequately for stresses below 1 MPa (Johnson, 1994). When used in the voltage mode the output of the gauge is calibrated to the stress on the gauge active area (the current mode gives stress rate and is not used here).

A time shift due to elastic wave propagation and a factor to compensate for the area difference of the sample and anvil (see Section 5.3.3) gives the stress at the contact surface. The gauge area is smaller than the anvil cross section. Therefore, a teflon spacer is used around the gauge so an accurate stress measure is obtained. Since the elastic moduli of the PVDF gauge and teflon are approximately equal, the spacer ensures equal strain in the gauge area, which in turn results in equal stress over this cross-section. Teflon spacers are also used to electrically insulate the gauge from the anvil. Complete details of the gauge are found in Baker

(1994) and will not be repeated here. The impedance problems also described in Baker (1994) did not occur in the present tests so the signal generated by the gauge is sent directly to an oscilloscope without further processing. The signal voltage is converted back to the charge on the gauge (q) using Eq. (5.1):

$$\frac{q(\mu\text{C})}{A(\text{cm}^2)} = \frac{\text{Volt(V)} \times C_{\text{cir}}(\text{pF})}{A(\text{cm}^2)} [10^6 \mu\text{V/V}] [10^{-12} \text{F/pF}] \quad (5.1)$$

where  $C_{\text{cir}}$  = circuit capacitance of gauge and cable in parallel = 100 pF  
 $A$  = active area of the gauge = .01 cm<sup>2</sup>

From this charge per unit area value, the stress  $\sigma$  is calculated from (Johnson, 1992):

$$\sigma(\text{GPa}) = 0.69 \times (q/A)^{1.11} \quad (5.2)$$

For the shotgun test the use of an accelerometer to calibrate the stress gauge results, as was done in the drop weight tests, is not possible.

### 5.1.5 Laser Obscuration System

Measurement of the post-impact projectile velocity during sample deformation (and hence projectile deceleration) facilitates the critical energy calculation. Instrumenting the projectile is not possible, and although velocity screens could be used to measure impact velocity, a new laser obscuration system was investigated in hope of providing pre- and post-impact velocities.

Laser obscuration is a temporal recording of laser light intensity as an object passes through a laser beam(s). If properly designed, this technique can yield quantitative measures of displacement, and hence velocity and acceleration. A single large diameter beam could be used, but its Gaussian intensity distribution would make data interpretation difficult. Therefore, discrete intensities are created by splitting the main beam into many parallel beams. A general schematic of this system is shown in Fig. 5.3.

A convenient technique for obtaining multiple laser beams is a plate beam splitter. This optical component allows a portion of the incident light to pass through the plate unaffected, while reflecting the remaining portion of the light. By using a plate beam splitter in conjunction with a flat first surface mirror, several parallel laser beams can be generated. The intensity of the parallel beams decreases after each split, but this decrease can be

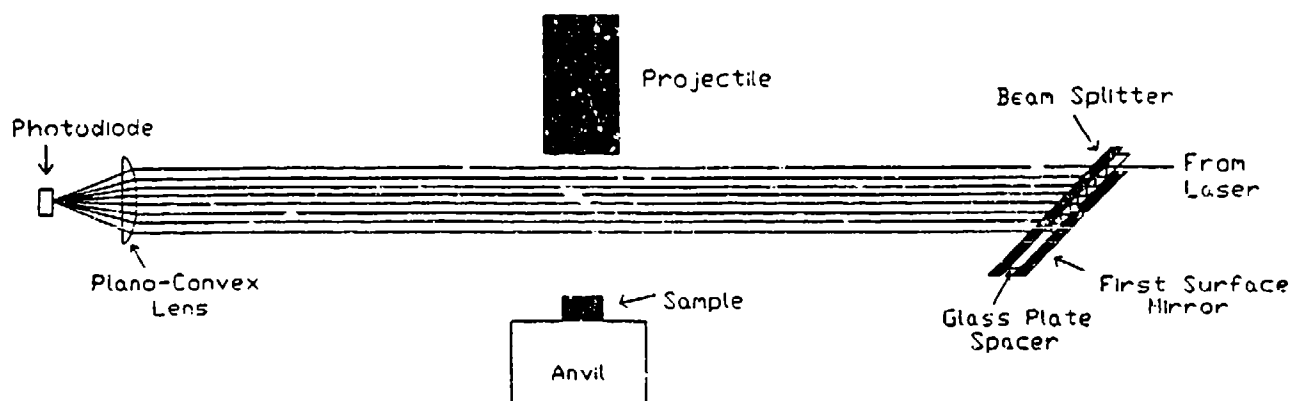


Figure 5.3. Schematic of laser obscuration system.

calculated. The beams are then focused using a plano-convex lens onto a photodiode detecting surface which results in intensity versus time output. The photodiode is a TEOR LABS high speed silicon detector (DET1-SI) with an internal bias 22.5 V battery which produces a 10 ns rise time. The active area of the diode (13.7 mm<sup>2</sup>) is adequate to capture the entire focused series of laser beams. During a test, the laser beams are obstructed by the projectile motion which decreases the intensity recorded by the photodiode. With careful calibration, this intensity is related to the displacement and hence velocity of the projectile. Other pertinent information regarding this system is listed in Table 5.2. A more thorough review of the present system's capabilities is provided in Section 5.3.1.

Table 5.2. Laser Obscuration System Information

---

Laser: Spectra Physics He-Ne, 10 mW max output, beam diameter $\approx$ 1.6 mm
First Surface Mirror: Edmund Scientific (P31497), 98% reflectivity, for use with He-Ne lasers
Plate Beam Splitter: Edmund Scientific (P31432), 75% reflectivity, 25% transmissivity
Plano-Convex Lens: Melles Griot (32345), 166 mm focal length

---

#### 5.1.6 Detection of Reaction

For the tests on live propellants, a second silicon photodetector (Hamamatsu, S1087-01) is mounted to the aluminum cover pipe (Fig. 5.1) slightly above the plane of the anvil impact surface. The instrument is directed at the middle of the sample. First detectable light emission indicates reaction and is used as the cutoff point for the critical energy calculation. This detector also provides a light intensity-time profile which assists in determining the severity of the reaction. The wide spectral response of this detector (400-1100 nm) ensures the detection of wavelengths that could be produced by the reaction. A protective covering of Teflon is placed over the photodiode to prevent propellant and/or projectile fragments from damaging the detector surface. The detector's 0.5  $\mu$ s rise time permits adequate resolution of the ignition events.

#### 5.1.7 Data Acquisition System

DATA6000 oscilloscopes with an input impedance of 1 M $\Omega$  at 35 pF were borrowed from MICOM and used to record the data. A schematic of the data acquisition system is shown in Fig. 5.4. The scope requires a plug-in card to operate. An available 4-channel plug-in had too slow a sampling rate (40  $\mu$ s) to resolve the velocity information. Therefore, a 2-channel

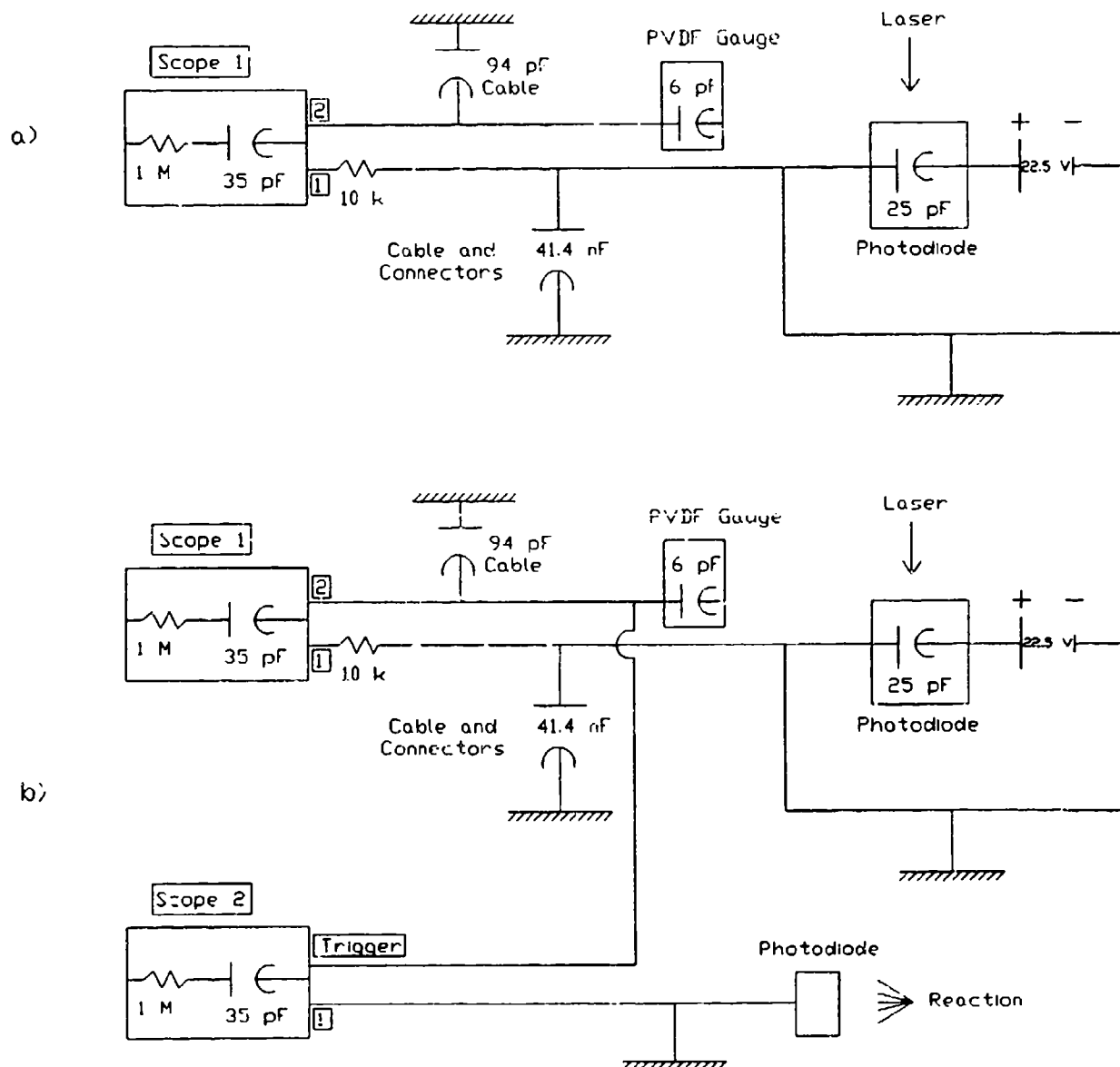


Figure 5.4. Data acquisition circuitry for a) tests on inert samples and b) tests on live propellants.

plug-in card with a maximum sampling rate of 27 ns is used, and in the tests on live propellant, the third data channel necessitates the use of a second oscilloscope (also with a fast response 2-channel plug-in).

The typical sequence of events for tests on inert samples (no first light photodiode) is as follows. A 50  $\mu$ s pre-recording of the laser signal precedes the scope triggering which occurs when the detected laser signal drops by a finite preset value (usually 20 mV) as the projectile blocks the beams. The scope then records the light intensity versus time as the projectile passes through the beams and begins to crush the sample. With adequate beam resolution, the signal may also be recorded as the projectile crushes the sample and hence decelerates. After a finite wave transit time through the sample and anvil ( $\approx 60 \mu$ s), the impact stress wave reaches the PVDF gauge location. The gauge then generates a voltage and is recorded on the second channel.

When live propellant samples are used, the sequence of events is slightly more complicated. The previously described events still occur. However, to trigger the second scope and keep the information for both scopes on relatable time axes, a signal from the first scope must be used as the trigger. This is accomplished by splitting the signal generated from the PVDF gauge and still recording the stress signal while using the other signal to trigger the second scope (Fig. 5.4). A 300  $\mu$ s delay is also used on scope 2 to pre-record the first light signal if it should occur before the stress signal triggers the scope. Thus, the initiation/ignition delay time (impact to first light) is found by determining the time when the first significant increase occurs in the first light trace and then subtracting the 300  $\mu$ s delay and adding the appropriate wave transit time delay.

All raw data are converted to ASCII numerical files with a BASIC program on a personal computer. These data are then input to spread sheets for manipulation and graph generation.

## **5.2 Finite Element Model of the Shotgun Test**

Finite element analysis is used as an additional analysis tool. The hydrodynamic, Lagrangian finite element code DYNA2D (Hallquist, 1982) is used for the analysis because of its ability to handle large sample deformations. The axisymmetric mesh used to model the shotgun impact test apparatus is shown in Fig. 5.5. The region around the propellant sample is shown enlarged for clarity. A  $5 \times 10$  mesh is used for the propellant unless otherwise noted. The propellant mesh is rezoned every 5  $\mu$ s. A linearly elastic, linearly plastic (LE-LP) propellant material model is used after Duffy (1993). Material constants used are listed in Table 5.3.

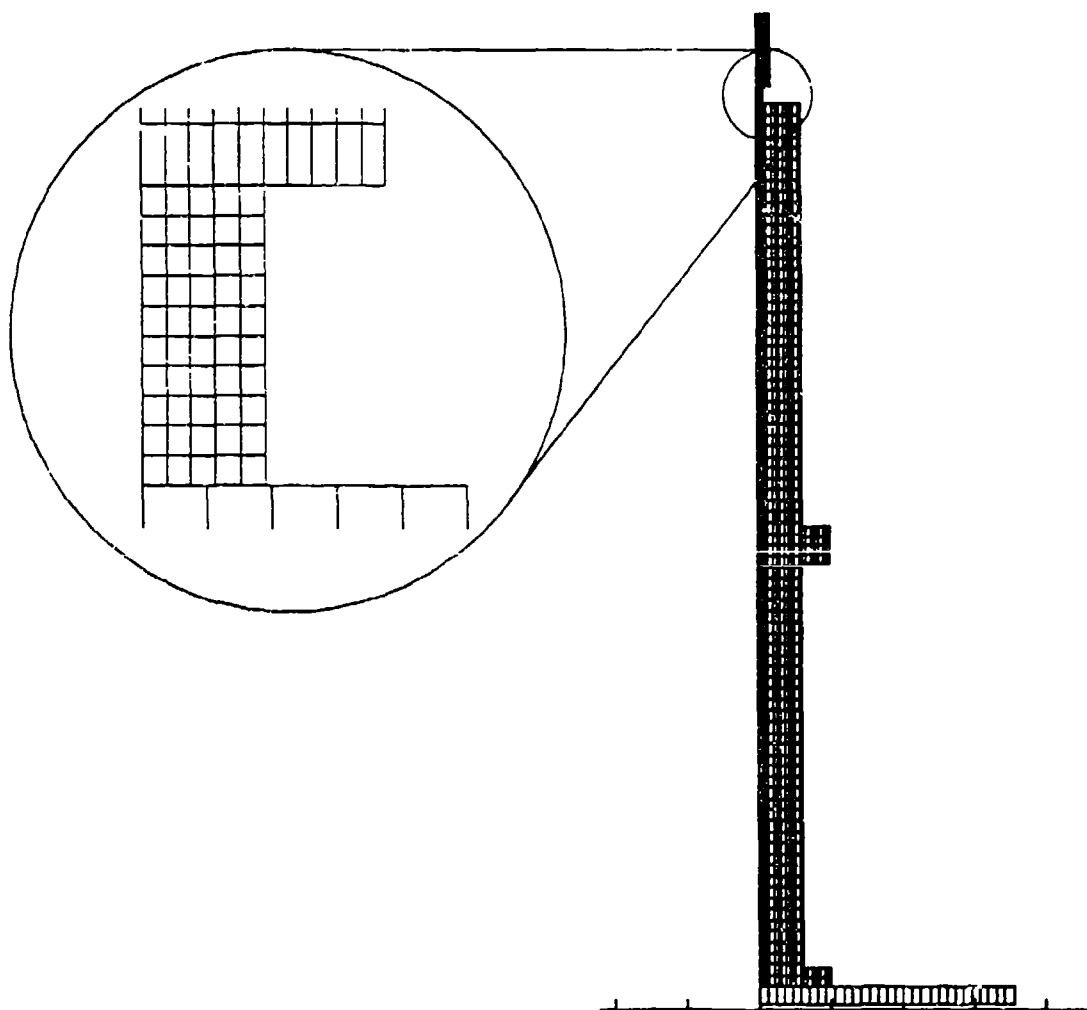


Figure 5.5. Axisymmetric finite element mesh of shotgun test including enlarged propellant sample region.



Table 5.3. Material constants used in DYNA2D model.

Constant	Steel	Propellant	PMMA
Young's Modulus (dyne/cm <sup>2</sup> )	$2.17 \times 10^{12}$	$6.895 \times 10^8$	$5.85 \times 10^{10}$
Plastic Modulus (dyne/cm <sup>2</sup> )	1	$6.895 \times 10^7$	1
Yield Stress (dyne/cm <sup>2</sup> )	$2.36 \times 10^{10}$	$6.895 \times 10^7$	$1 \times 10^9$
Density (g/cm <sup>3</sup> )	7.8	1.83	1.19
Poisson's Ratio	0.3	0.499	0.33

Propellant/anvil and propellant/impactor interfaces are modeled using the penalty friction model (Hallquist, 1978) with a friction coefficient of 0.2. The exact value for the friction coefficient is not known. It is estimated to be between 0.2 and 0.5. Experimental data for Composition B-3 (A), an explosive with TNT, RDX, and a small percentage of wax, indicate that the range of 0.2 and 0.5 is appropriate and that the coefficient decreases with increasing pressure (Dobratz and Crawford, 1985). Since the pressure at the interfaces in the shotgun tests is greater than the pressures used to obtain the friction coefficients, the lower value is used.

### 5.2.1 Stress Wave Propagation

The gauge is placed 30.48 cm (12") from the surface of the anvil in accordance with Hopkinson bar theory which states that stress waves in a cylinder become one-dimensional when they have traveled a distance equal to five cylinder diameters from the surface. Closer to the surface, the stress wave is three dimensional and reflects off the cylinder circumference. If the gauge were placed any closer to the impact surface, the rebounding waves would interfere with the measurement.

Contour plots of von Mises stress show the wave propagation through the anvil (Fig. 5.6). The contour plotted ( $2.5 \times 10^5$  dyne/cm<sup>2</sup>) was chosen high enough to filter out the numerical noise present in the stress curves while still showing the beginning of the stress wave. These results confirm the Hopkinson bar theory and indicate the gauge was located correctly. At 72  $\mu$ s, when this stress wave has reached the gauge, it is indeed a one-dimensional wave. At earlier times, the wave is not one-dimensional, and reflected radial waves are significant.

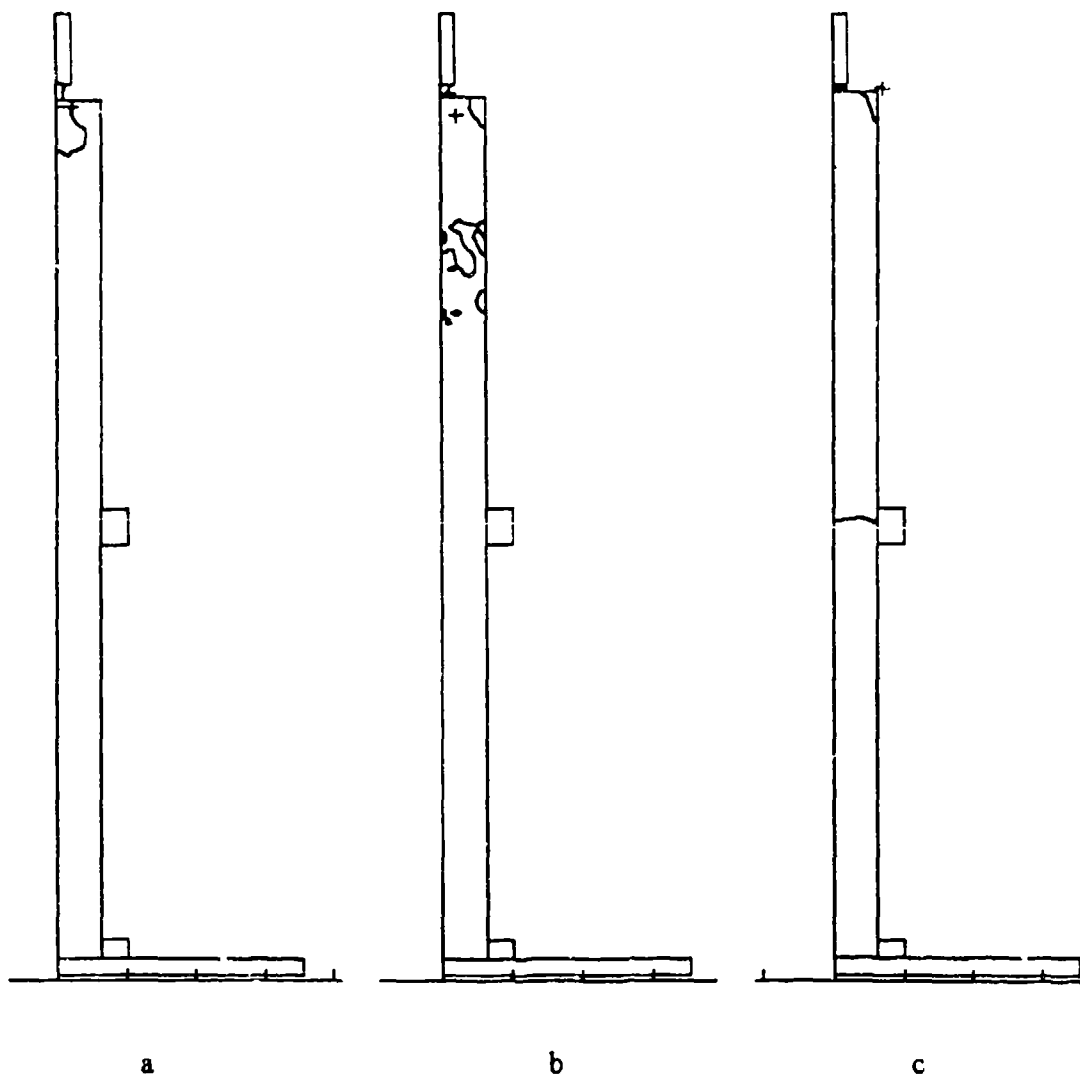


Figure 5.6. Contour plots of von Mises stress at a) 10  $\mu$ s, b) 38  $\mu$ s , and c) 72  $\mu$ s.

### 5.2.2 Stress Correlations

One goal of the finite element modeling was to obtain a correlation between the stress at the gauge location and the stress at the anvil surface. Several variables were changed in an attempt to determine how they affect the overall correlation. These included: (1) impact velocity, (2) slideline type, (3) initial velocity of the sample top surface, (4) two scaling factors (STIF and TSCL) related to the wave transit time through the materials (see Duffy, 1993), and (5) the use of element averaging methods. The numerical output was correlated using the equation

$$\frac{\sigma_{p v d f}}{\rho V_0^2} = m \frac{\sigma_{s u r f}}{\rho V_0^2} + \frac{b}{\rho V_0^2} \quad (5.3)$$

where  $V_0$  is the initial velocity of the PMMA,  $\rho$  is the density of the PMMA,  $m$  is the slope,  $b$  is the y-intercept, and  $\sigma$  is axial stress in the element closest to the centerline. The values were non-dimensionalized with initial projectile momentum per unit area so the y-intercept and standard deviation values could be compared for different impact velocities. All the correlations are summarized in Table 5.4.

Table 5.4. Summary of Stress Correlations.

Case	STIF	TSCL	$V_0$ (m/s)	Top Row Moving	Slope $m$	y-int $b$ , dyne/cm <sup>2</sup>	R	Standard Dev., dyne/cm <sup>2</sup>
1	0.1	0.66	200	no	0.0108	-0.0007	0.54	0.0009
2	0.1	0.66	200	yes	0.0007	-0.0013	0.11	0.0012
3	0.1	0.66	100	no	0.0287	-0.0069	0.83	0.0166
4	0.1	0.66	100	yes	0.0276	-0.0078	0.84	0.0173
5	0.1	0.66	10	no	0.0364	-0.0559	0.96	0.1589
6	0.1	0.66	10	yes	0.0320	-0.1299	0.86	0.3132
7	1.0	0.21	200	no	0.0301	-0.0634	0.44	0.0133
8	1.0	0.21	200	yes	0.0020	-0.0010	0.37	0.0020
9	1.0	0.21	100	no	0.0195	-0.0174	0.63	0.0292
10	1.0	0.21	100	yes	0.0309	-0.0142	0.72	0.0415
11	1.0	0.21	10	no	0.0294	-0.0254	0.87	0.3098
12	N/A	0.66	100	no	0.0231	-0.0224	0.54	0.0487
13	N/A	0.66	100	no	0.0229	-0.0182	0.57	0.0361
14	0.1	0.66	100	no	0.0354	-0.0060	0.88	0.0136
15	0.1	0.66	100	no	0.0287	-0.0006	0.93	0.0105
16	0.1	0.66	100	no	0.0287	-0.0075	0.92	0.0113

A time delay of 58  $\mu$ s was used in the correlation to account for the time required for the stress wave to propagate from the anvil surface to the gauge location using elastic longitudinal sound speed. The numerical output was not correlated at times later than 174  $\mu$ s, since after

this time, the stress wave reflected from the anvil bottom interferes with the stress at the gauge. Only the cases with a 10 m/s impact velocity calculated to a time greater than 174  $\mu$ s without excessive computational problems.

The highest correlation coefficient ( $R = 0.96$ ) is not high enough to be considered indicative of a strong correlation. This value was obtained (Case 5) for an impact velocity of 10 m/s, which is not representative of the shotgun impact tests which have impact velocities between 150 and 200 m/s.

Increasing STIF from 0.1 to 1.0 had a negative effect on the correlation. The correlation coefficient decreased from 0.83 (Case 3) to 0.63 (Case 9) when STIF was increased for an impact velocity of 100 m/s. Similarly, the standard deviation increased from 0.017 to 0.029. Comparisons of other cases where STIF was increased show the same effects. Setting the initial velocity of the nodes on the sample's top surface equal to projectile impact velocity did not have a clear effect on the correlation.

The correlation coefficient has an inverse relationship with the impact velocity. This relationship is partially explained by the smaller number of points used in the correlation at higher velocities. Twelve points were used in Case 1 while twenty-six were used in Case 5. Fewer points are available at higher velocities because the computational time is smaller.

The relationship between the two stress values should be the same regardless of the impact velocity. This is not shown in the correlations obtained. The slope increases as the velocity decreases. The dependence on velocity along with the lack of a strong correlation prevent the determination of the relationship between the gauge measurements and the stress at the anvil surface.

The finite element model exhibits significant undesired penetration of the projectile into the sample when the default values of STIF are used. Increasing STIF delays the onset of penetration, but adversely affects the correlation. An alternative method of eliminating penetration from the model is to use frictionless slidelines. The slideline type controls how the interface between two materials is modeled. Penetration occurs because of the friction model; therefore, frictionless slideline types will not allow penetration to occur.

Two alternative slideline types were examined: Type 1—sliding only (Case 12) and Type 3—frictionless sliding with voids (Case 13). Friction is not modeled by either type. The friction model is slideline Type 4. Slideline Type 1 requires that the two surfaces are always in contact while slideline Type 3 allows voids to form between the two surfaces. The impact velocity and time step are the same as Case 3. STIF has no meaning when frictionless slideline types are used. The results of these correlations are shown in Table 5.4.

Altering the slideline type has a significant effect on the correlations obtained. The correlation coefficient is reduced from 0.83 for Type 4 to 0.54 for Type 1 and 0.57 for Type 3.

The reason for this effect is the increase of radial waves in the axial stress curves for the frictionless cases (Fig. 5.7). Radial waves present in the sliding only case are not as evident in the friction case, indicating that friction dampens the radial waves before they affect the centerline element.

The absence of friction also affects the deformation of the sample. Without frictional forces, the sample extrudes much further. Since the deformation of experimental samples is affected by friction the preferred model is the friction slideline.

Several alternative methods for obtaining the stress correlation were tried. The output from Case 3 was used for each of the alternative correlations. The results of these attempts are listed in Table 5.4 (Cases 14 to 16). Previous correlations were performed using the element closest to the anvil centerline. The stress wave at the gauge location is a one-dimensional wave; therefore, the axial stress is the same in all elements at the gauge location. Averaging these values eliminates some of the numerical noise found in the stress curves for individual elements.

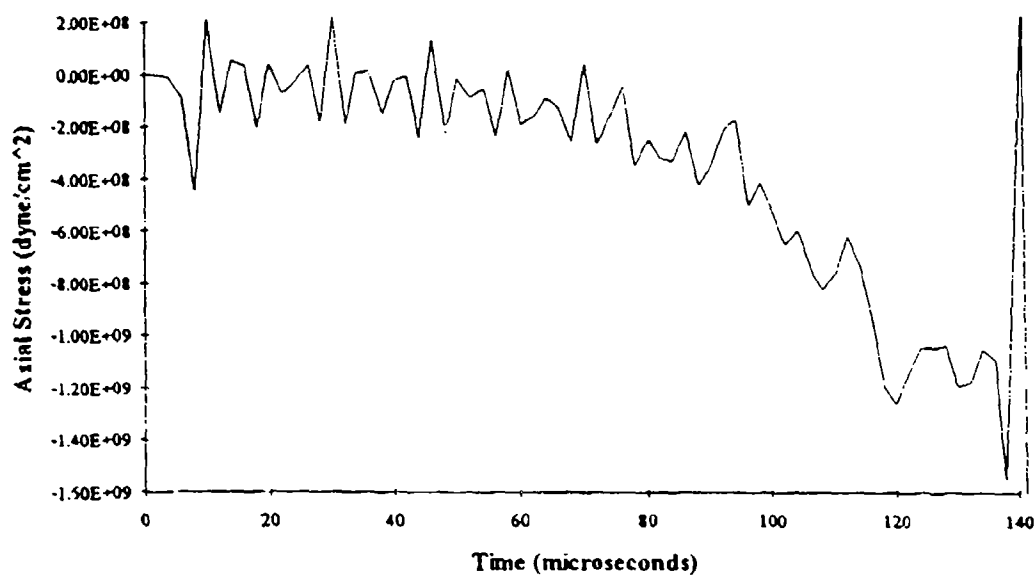
Correlating the average value at the gauge with the centerline element value at the surface (Case 14) results in a correlation coefficient of 0.88 and a standard deviation of 0.0136. Elements within five sample diameters of the centerline are averaged for the correlation. The elements near the edge are not used because their stress curves are affected by edge effects due to the presence of the flanges. Averaging the elements improved the correlation, but did not result in an acceptable correlation.

An alternative correlation was tried using the gauge stress and the stress in the bottom surface of the sample. The five elements in the bottom of the sample were averaged and correlated with both the centerline stress (Case 15) and averaged stress at the gauge location (Case 16). These correlations are the best obtained for a 100 m/s impact.

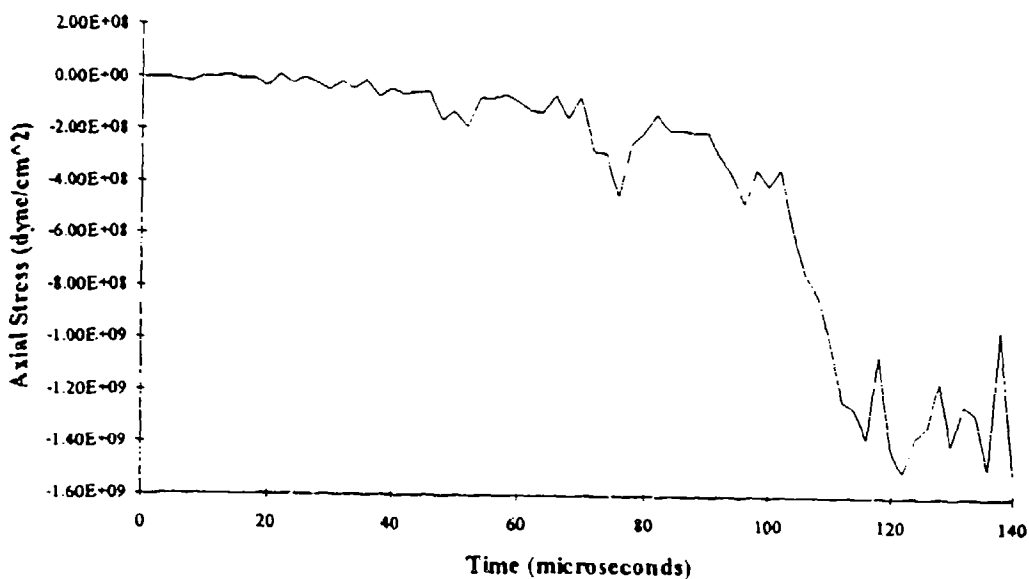
Although these alternative methods resulted in improved correlations, they do not provide strong enough correlations ( $R > 0.98$ ) which can be used to predict the stress in or near the sample using the gauge stress. The best conclusion the analysis supports is that the gauge stress is between 1 and 5% of the sample top or bottom surface stress.

### 5.2.3 Energy Distribution

The development of the critical energy model (Section 5.3.3) involves assumptions about the amount of energy stored in the machine. The model requires that only insignificant amounts of energy are transferred into the machine. The kinetic energy lost by the PMMA projectile is assumed to be transferred into strain energy in the sample instead of into the machine.



a



b

Figure 5.7. Axial stress at the anvil surface for slideline a) Type 1 and b) Type 4.

Kinetic energy in a material is obtained from the model results. Strain energy density ( $E_{\text{strain}}$ ) is the area under the stress-strain curve and is calculated by the following equation

$$E_{\text{strain}} = \int \sigma_{ij} d\epsilon_{ij} \quad (5.4)$$

where  $\sigma_{ij}$  and  $\epsilon_{ij}$  are the stress and strain tensors.

Nine elements in both the sample and PMMA are used for strain energy calculations. The location of these elements is shown in Fig. 5.8. The strain energy in an element is then determined using the axisymmetric volume represented by the element, and these values are averaged to obtain the strain energy per element. The strain energy for the entire sample is found by multiplying the strain energy per element by the number of sample elements. For the PMMA the strain energy is found by multiplying the strain energy per element by the number of elements in the bottom quarter of the PMMA. This was based on visual inspection of the projectile mesh which showed the deformation was concentrated in the bottom portion of the projectile.

Impact velocities of 50, 100, and 150 m/s were used to determine if the assumptions made in the critical energy model are valid for the shotgun tests. The results of the model for the 100 m/s impact are shown in Fig. 5.9. The values are normalized by the initial kinetic energy of the PMMA projectile (80 J).

The kinetic energy of the anvil remains less than 1% of the total energy and can be neglected. At times less than 100  $\mu\text{s}$ , the PMMA strain energy is negligible. After 100  $\mu\text{s}$ , this value becomes significant, reaching 10% of the system's total energy after 130  $\mu\text{s}$ .

The kinetic energy of the sample remains less than 10% of the total energy. However, the kinetic energy values are not accurate since each time the sample was rezoned, some kinetic energy was lost. The losses remain less than 1% of the total energy through 80  $\mu\text{s}$  but reach 9% at 140  $\mu\text{s}$  when severe sample deformation and penetration occur. Total rezone loss is approximately equal to the maximum kinetic energy in the sample.

Sample strain energy is approximately equal to the sample kinetic energy at times less than 80  $\mu\text{s}$ . If the energy lost to rezoning is added to the sample kinetic energy, the strain energy remains equal to the kinetic energy until 120  $\mu\text{s}$ .

The projectile decelerates, and hence its kinetic energy decreases slowly until 100  $\mu\text{s}$  when a more rapid decrease occurs. At 90  $\mu\text{s}$  (Fig. 5.10) the amount of penetration begins to increase significantly indicating severe pressures at this interface. After this time, the sample is more resistant to deformation and greater stresses are transmitted through the sample into the anvil. This shows up as a significant increase in the anvil strain energy and also corresponds to

1006		1008		1010
981		983		985
961		963		965

a

1051					1056				1060
1031					1036				1040
1011					1016				1020

b

Figure 5.8. Location of elements used in strain energy calculations for a) sample and b) PMMA projectile.



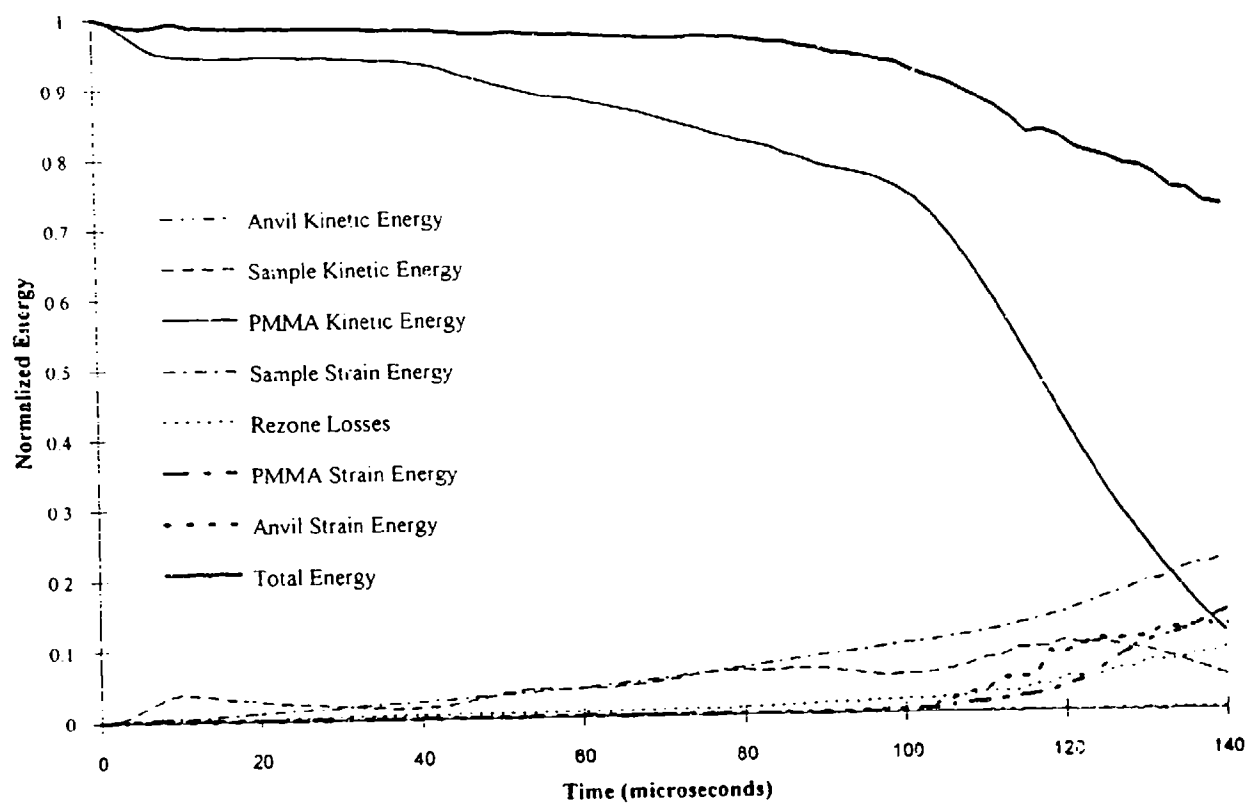


Figure 5.9. Calculated energy values for 100 m/s impact.

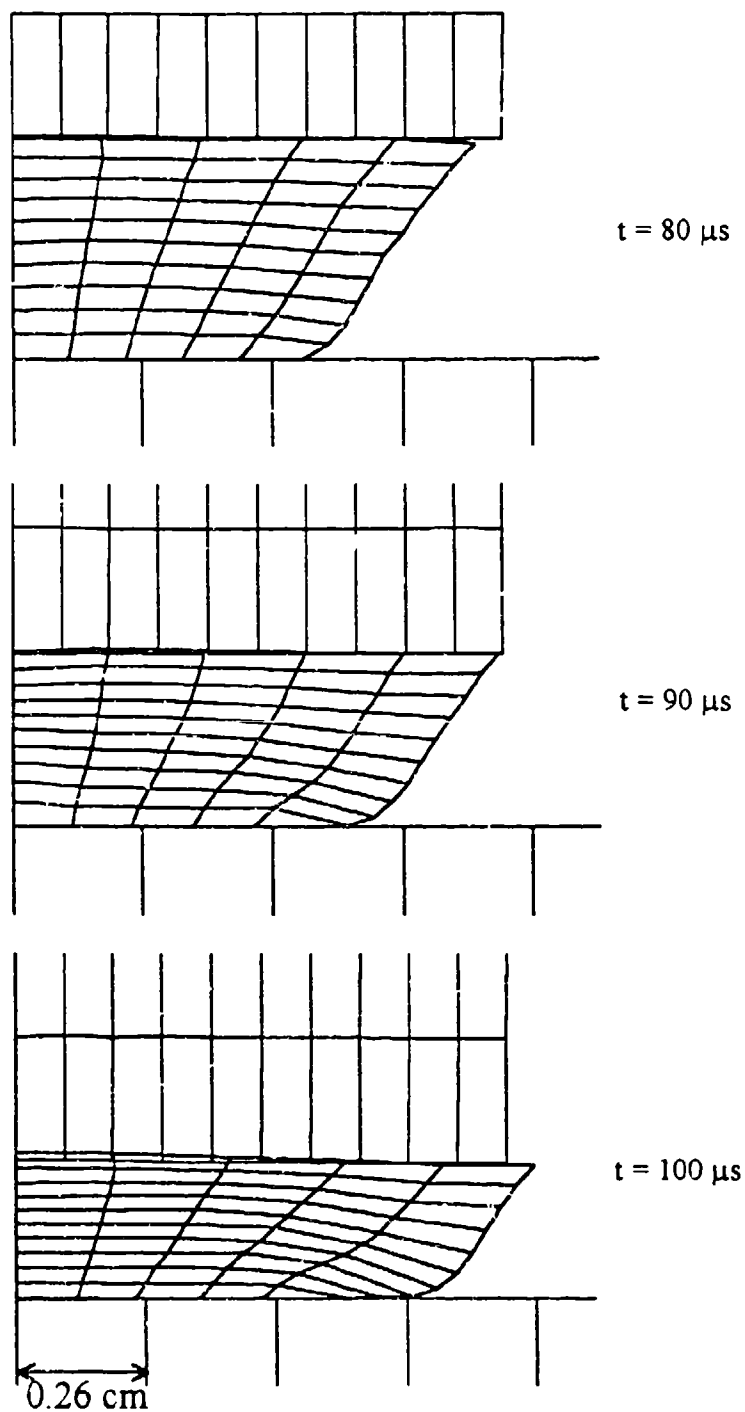


Figure 5.10. Deformation of sample mesh at three different times showing penetration between projectile and sample surfaces at  $90 \mu s$  ( $V_0 = 100 \text{ m/s}$ ).

an increase in projectile strain energy (heavy dotted lines in Fig. 5.9).

The total amount of energy in the system should remain constant at the initial kinetic energy of the projectile. The sum of the individual energy components remains greater than 90% of the initial energy through 100  $\mu$ s. After that time, the total amount of energy begins to drop off more quickly. Some of the discrepancy between the calculated total energy and the initial energy can be accounted for by the method of calculating the strain energy. For both the sample and PMMA, only nine of fifty elements were used for the calculations and only nine of 480 for the anvil. After 100  $\mu$ s, the increasing size of the discrepancy is related to the amount of penetration.

At an impact velocity of 150 m/s, similar trends are observed. The anvil kinetic energy is negligible, but the sample kinetic energy is greater than the sample strain energy at times less than 85  $\mu$ s as shown in Fig. 5.11. Kinetic energy losses due to rezoning were not examined, but if they are comparable to those found for a 100 m/s impact, the sample kinetic energy may be comparable to the sample strain energy at all times. The strong decrease in total energy observed at 100  $\mu$ s for the 100 m/s impact occurs at 70  $\mu$ s and is accompanied by an increase in penetration and presumably the increase in projectile and anvil strain energies.

For a 50 m/s impact, the sample strain energy is more significant (Fig. 5.12). The sample kinetic energy remains below 5% of the total energy, and the anvil kinetic energy remains below 1%. The sample strain energy accounts for over half of the loss in PMMA kinetic energy, but a large portion of the energy is not accounted for. Total energy drops to 55% of the initial total energy. PMMA strain energy was not calculated, but the projectile mesh does not show the deformations necessary for that amount of strain energy. The sample mesh for the 50 m/s impact does not become severely distorted, and therefore rezoning losses are not significant. The sudden decrease in total energy found for the higher impact velocities does not occur due to the minimal penetration at this lower velocity.

These results support the drop weight analytical modeling which indicated sample kinetic energy may not be negligible in the shotgun test (Baker, 1994). Since the critical energy model assumes that all of the PMMA kinetic energy is transferred into sample strain energy before initiation sample kinetic energy and elastic strain energy storage may make interpreting shotgun impact results difficult.

#### 5.2.4 Stress Localization

Experimental results indicate that in a drop-weight test, initiation occurs in hot spots near the radial edge of the sample, possibly due to the high shear stresses (Coffey et al., 1989). The localization of energy causes the sample to initiate before the auto-ignition temperature is attained throughout the bulk sample.

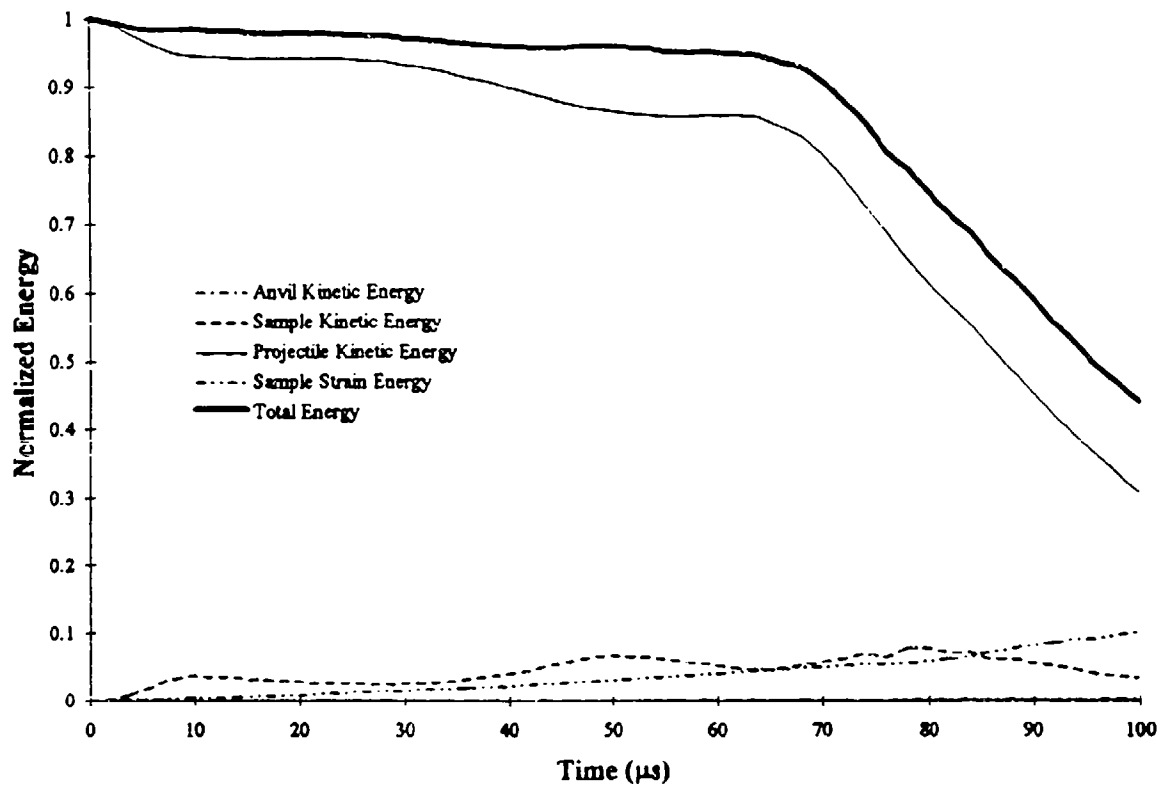


Figure 5.11. Calculated energy values for 150 m/s impact.

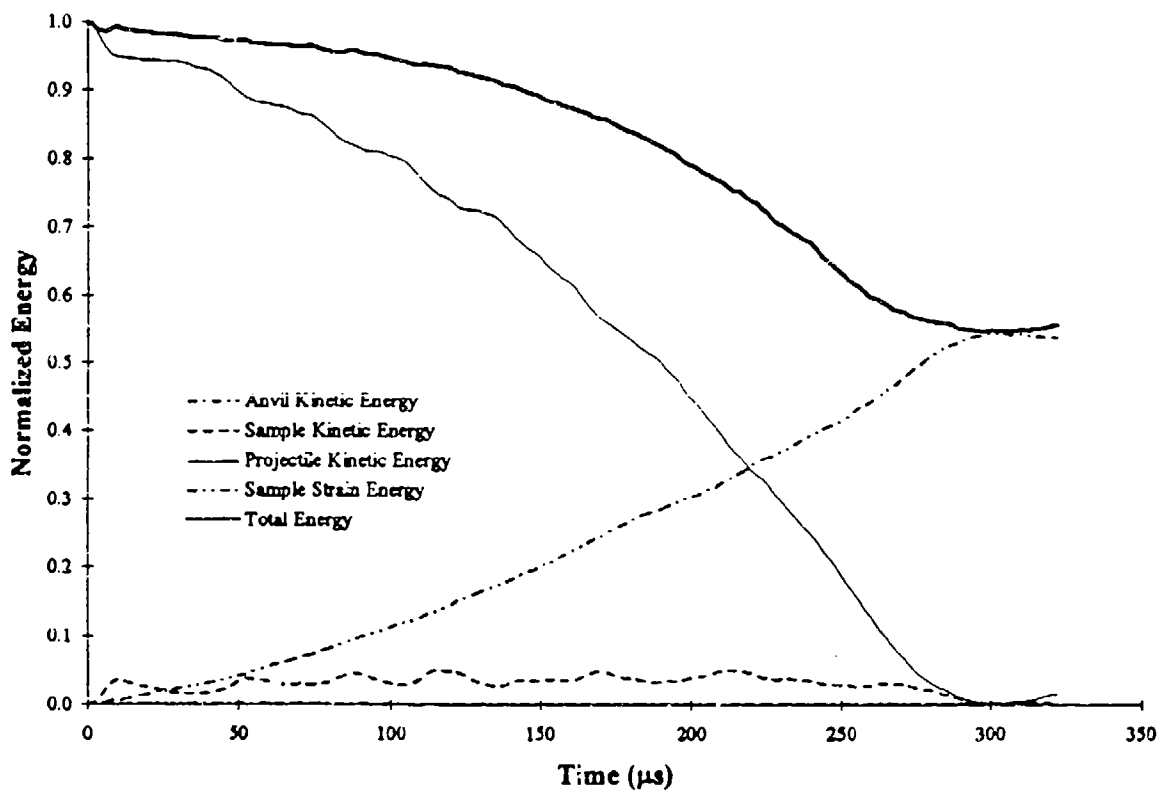


Figure 5.12. Calculated energy values for 50 m/s impact.

Calculations show that the strain energy is also not evenly distributed throughout the shotgun test sample. Strain energy density values for the elements indicated in Fig. 5.8 are given in Table 5.5 for an impact of 100 m/s. Prior to 80  $\mu$ s the energy does not show a definite trend radially. The bottom radial edge element (965) has the highest energy density of the three elements on the bottom of the sample, but the top radial edge element (1010) has the lowest value of the top elements. Energy density increases from the bottom to the top of the sample, and more energy is localized in the top surface of the sample than in the bottom surface.

Table 5.5. Strain Energy Density Values (dyne/cm<sup>2</sup>).

Element	r/r <sub>0</sub>	z/z <sub>0</sub>	V <sub>0</sub> = 100 m/s		V <sub>0</sub> = 150 m/s	
			80 $\mu$ s	120 $\mu$ s	60 $\mu$ s	100 $\mu$ s
			E <sub>strain</sub> × 10 <sup>7</sup>		E <sub>strain</sub> × 10 <sup>7</sup>	
961	0	0	3.3	5.7	3.8	6.0
963	0.5	0	3.2	6.5	4.1	6.8
965	1	0	4.9	7.6	5.9	12
981	0	0.5	6.1	8.9	8.6	9.9
983	0.5	0.5	6.3	1.2	7.9	12
985	1	0.5	5.8	15	7.1	31
1006	0	1.0	10	14	15	27
1008	0.5	1.0	12	33	15	48
1010	1	1.0	9.0	15	13	26

At 120  $\mu$ s, a definite radial trend is present with greater energy density at the edge than at the centerline (except for the top surface). At the top surface, the highest energy density is in the middle element. The highest value is not at the edge because that element is no longer in contact with the projectile. It has extruded beyond the projectile edge, as shown in Fig. 5.10. The same trends are evident for a 150 m/s impact.

These calculations indicate that the greatest concentration of energy is present on the top surface of the sample at the outermost radial point which is in contact with the projectile. However, the energy density does not reach a level sufficient to cause initiation. The mean critical energy density required to cause a hot spot reaction in the drop-weight tests was 111 J/g for Arcadene-360 propellant (Baker, 1994). This corresponds to an energy density of  $2.1 \times 10^9$  dyne/cm<sup>2</sup>. If any location in the sample reaches that energy density it should initiate if critical energy density is independent of impact velocity for this propellant. The highest values obtained for the 100 and 150 m/s impacts are  $3.3 \times 10^8$  and  $4.8 \times 10^8$  dyne/cm<sup>2</sup>, respectively, neither of which is sufficient to cause initiation. The validity of the energy density numbers is limited by several factors including the material properties and the presence of penetration in

the model. However, the qualitative trends obtained can be considered valid and suggest samples of the size used in the shotgun model (10 mm diameter, 12 mm long) and initially proposed for the test may not initiate at these velocities.

One finite element computation was performed using a 10 mm diameter 6 mm long propellant sample and an impact velocity of 100 m/s. The normalized energy distribution curves are shown in Fig. 5.13. Time constraints did not permit determining the anvil and projectile strain energies, but the qualitative trends of the remaining curves are the same as for the 12.7 mm sample except the decrease in total computed energy occurs at approximately 50  $\mu$ s. The sample elastic strain energy storage for the shorter specimen is somewhat higher.

### **5.3 Experimental Results**

Approximately the first nine months of the sixteen month shotgun impact program were spent designing and constructing the hardware and optical system. During that time extensive calibrations were made of the obscuration system, and these results are presented in Section 5.3.1. The remaining time was devoted to the projectile impacts on inert and live propellants to test the PVDF stress gauge performance and measure the reaction intensities (Section 5.3.2). In Section 5.3.3, the critical energy calculations are presented.

#### **5.3.1 Capabilities of the Laser Obscuration System**

The original concept involved a pattern of 50 one millimeter beams spaced one millimeter apart. This was to be accomplished using a He-Ne laser with a beam diameter of one millimeter and a beam splitter with 99% reflectivity. However, the laser was borrowed rather than purchased and has a slightly larger beam diameter of approximately 1.6 mm. In addition, the highest reflectivity of beam splitters commercially available at reasonable cost is 75%. At most eight beams could thus be generated, with their parallelism in question since after eight reflections, the beam intensity is degraded to an undetectably small value. Due to several other problems encountered, as discussed below, the present system is not capable of accurately measuring the post-impact deceleration of the projectile.

##### **5.3.1.1 Spacing Constraints**

Several constraints are placed upon the optical system which limit the measurement of post-impact velocity. A sketch of the "parallel" beam-generating optical components is shown in Fig. 5.14. To obtain the ideal series of parallel beams spaced one mm apart using an incidence angle of 45° requires a glass spacer with a uniform thickness of 0.707 mm between the beam splitter and first surface mirror. However, as explained later, a plate this thin is very

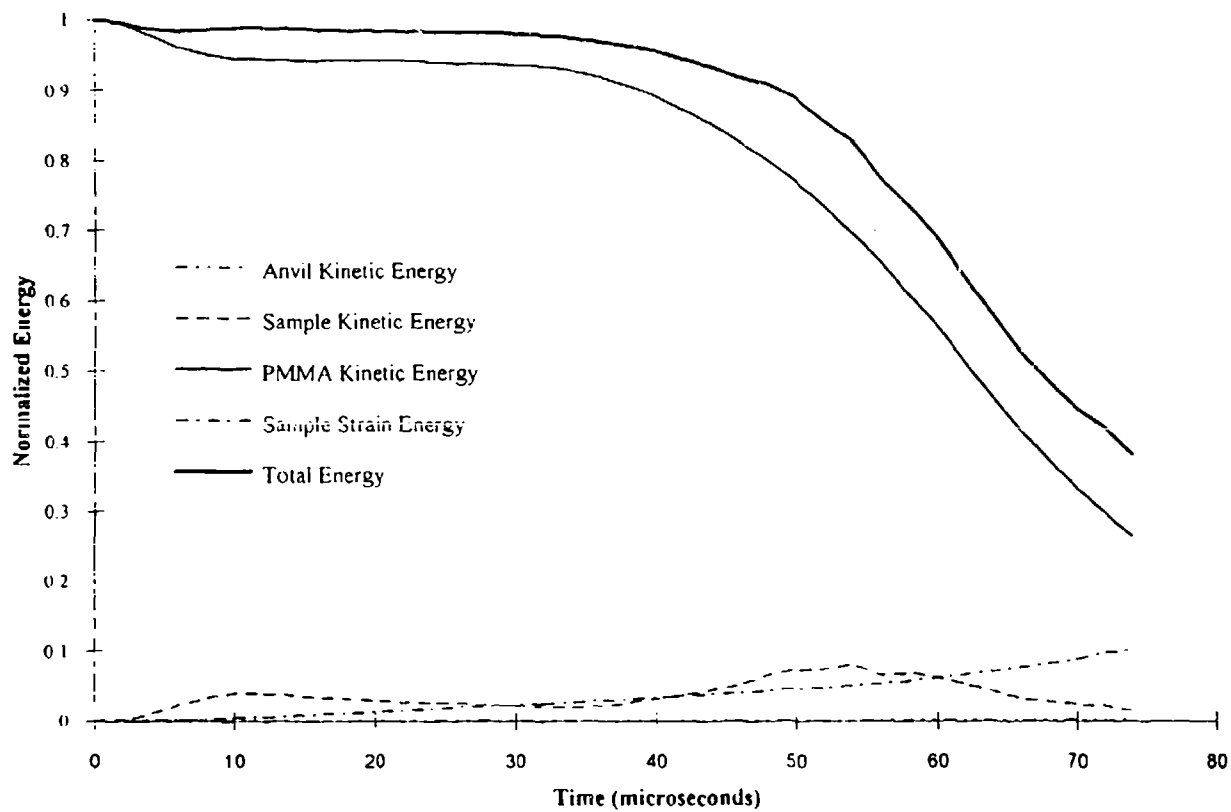


Figure 5.13. Calculated energy values for 100 m/s impact on a smaller 6 mm long sample.



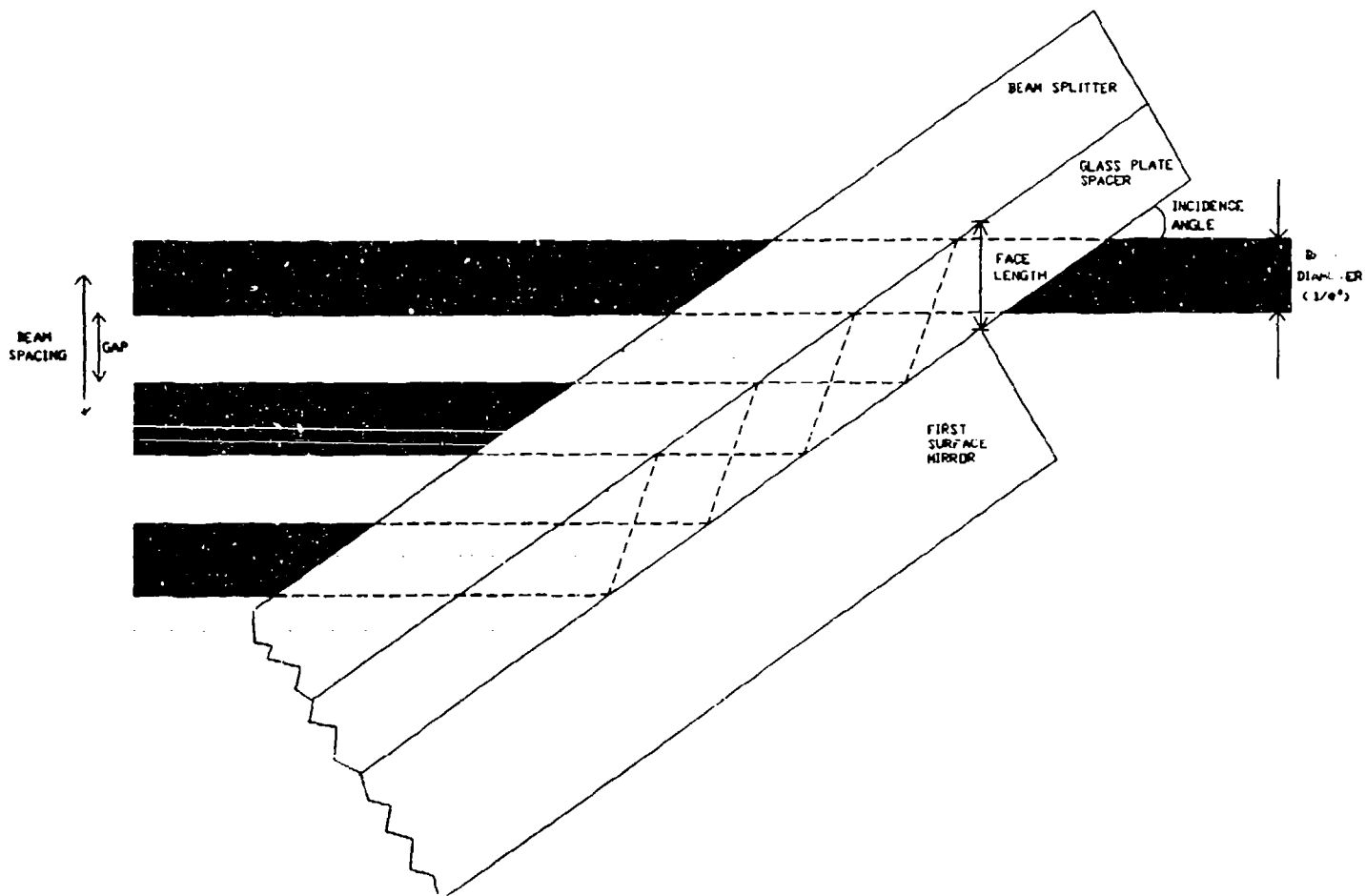


Figure 5.14. Optical components used to generate parallel beams.

difficult to manufacture with the length and width requirements of this experiment and still have parallel surfaces. To construct a piece of glass the approximate size needed with  $1/10$  wavelength flatness and parallelism in the seconds range, the glass would have to be a minimum of 9.5 mm ( $3/8$ ") thick (Spindler-Hoyer, 1993) which is prohibitively large for this experiment. Therefore, other commercially available plates with thicknesses of 1, 1.59, and 3.18 mm were acquired.

For example, considering a glass plate spacer of thickness 1.59 mm and an incidence angle of  $35^\circ$  leads to a face length, defined in Fig. 5.14, of 1.94 mm (see Appendix B). Since the diameter ( $1/e^2$ ) of the laser beam is approximately 1.6 mm, gaps of less than 0.2 mm exist above and below the beam. A gap this small makes beam alignment difficult. Henceforth, spacing will refer to centerline beam spacing (Fig. 5.14), and gap will refer to the region between beams where little or no laser light is present. If the entrance beam is misaligned, it may be partially blocked by the corner of the first surface mirror making interpretation of the resulting signal difficult. Furthermore, at angles greater than  $45^\circ$ , the top portion of the beam may be reflected downward in such a manner as to irradiate the leading edge of the first surface mirror (i.e., missing the reflecting surface) again making analysis difficult.

Calculations (Appendix B) also show for the above setup that the resulting centerline beam spacing is 2.6 mm. As discussed later, this is too large if one wishes to determine post impact velocity over a distance of at most 12 mm (the propellant sample length). The face length and centerline beam spacing are related as shown in Fig. 5.15 for the three spacers. For increasing incidence angle, the face length increases while the beam spacing decreases which are both beneficial results. However, the optical surfaces are designed for use at a  $45^\circ$  angle (maximum reflectivity, etc.) so any value greater than  $50^\circ$  or smaller than  $40^\circ$  should be avoided.

Keeping in mind the laser beam diameter of 1.6 mm, from Fig. 5.15 it is apparent that the 1 mm spacer cannot be used except at angles greater than  $60^\circ$  since the face length must be at least 2 mm in order to "fit" the beam in the space. Both the 1.59 mm and the 3.18 mm spacers meet the criteria at  $45^\circ$ .

#### 5.3.1.2 Beam Divergence

Another potential problem which could make analyzing the data difficult is divergence. Theoretically, the beams can diverge to the point where they cross one another, leaving no distinct gap. Due to the propagation properties of Gaussian beams, each beam will have a waist radius ( $w_0$ ) as shown in Fig. 5.16. The far field divergence angle ( $\theta'$ ) is given by (Durst and Stevenson, 1977):

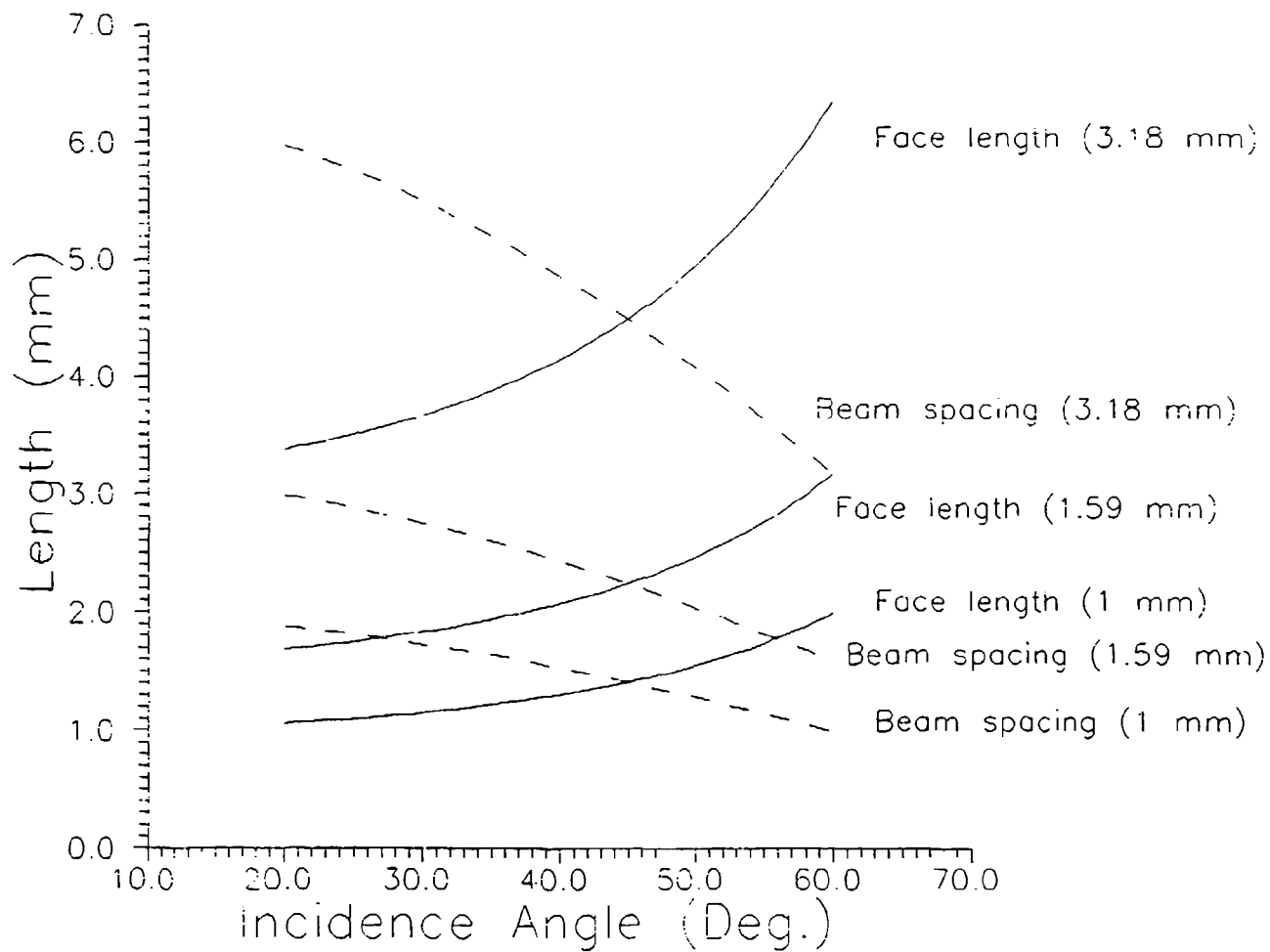


Figure 5.15. Face length and centerline beam spacing as a function of incidence angle for three different spacers.

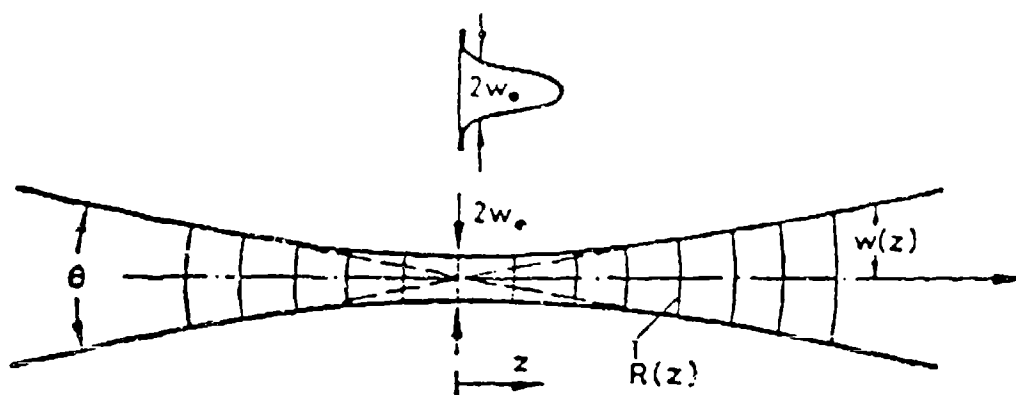


Figure 5.16. Parameters describing Gaussian beam characteristics (from Durst and Stevenson, 1977).

$$\theta' = 2\lambda/\pi w_0 \quad (5.5)$$

where  $\lambda$  is the wavelength of the light. At a  $z$  location downstream, the beam radius  $w(z)$  is given by (Durst and Stevenson, 1977):

$$w^2(z) = w_0^2 [1 + (\lambda z/(\pi w_0^2))^2] \quad (5.6)$$

For the He-Ne laser used in this study, the waist is most likely found at the aperture of the laser (Pitz, 1993). Equation (5.6) (solved for  $w(z)$  and multiplied by 2 to give diameter) is plotted for several beam waist diameters in Fig. 5.17. For the 1.6 mm waist, the divergence at 500 mm, which is the approximate location where the projectile will break the beams, is small enough (two-hundredths of a mm) to be neglected. Similarly, the 1.0 mm waist diameter beam leads to only an eight-hundredths of a mm divergence at 500 mm. However, because of the  $w_0$  term in the denominator of Eq. (5.6), the divergence for the 0.5 mm waist beam is almost doubled at 500 mm which, depending on the spacing required, limits its usefulness.

#### 5.3.1.3 Non-Parallel Surfaces

The analysis of the oscilloscope voltage-time curves assumes the beams are parallel for the determination of the spacings. This, in turn, implies the optical components which produce the beams are also flat and parallel. The first surface mirror and beam splitter are both flat (1/10 wavelength), and their surfaces are parallel to 20 seconds. However, because the glass plate spacers are much thinner (1-3 mm compared to 9 mm) than these other two pieces, they cannot be made as flat or their surfaces made parallel.

That being the case, the glass plates are approximately parallel to 3 minutes (0.05°). Calculations were performed to see the effect on this optical arrangement. Referring to Fig. 5.18, if the spacer surfaces are parallel to 0.05°, the second beam is reflected slightly upward so that eventually the beams will converge. Assuming a 2.25 mm centerline spacing for the 1.59 mm glass spacer with an incidence angle of 45° (Eq. (B.1)), this convergence location is approximately 2500 mm from the optics. More relevant to the test, at 500 mm the beams converge to 1.8 mm (or 20% of the initial value) which is close to the beam diameter. This suggests the non-parallelism is a factor which cannot be ignored.

#### 5.3.1.4 Beam Transmission Measurements

The reflectivity and transmissivity of the beam splitter when placed at an angle of 45° with respect to the incoming beam are reported in the catalog as 75% and 25%, respectively.

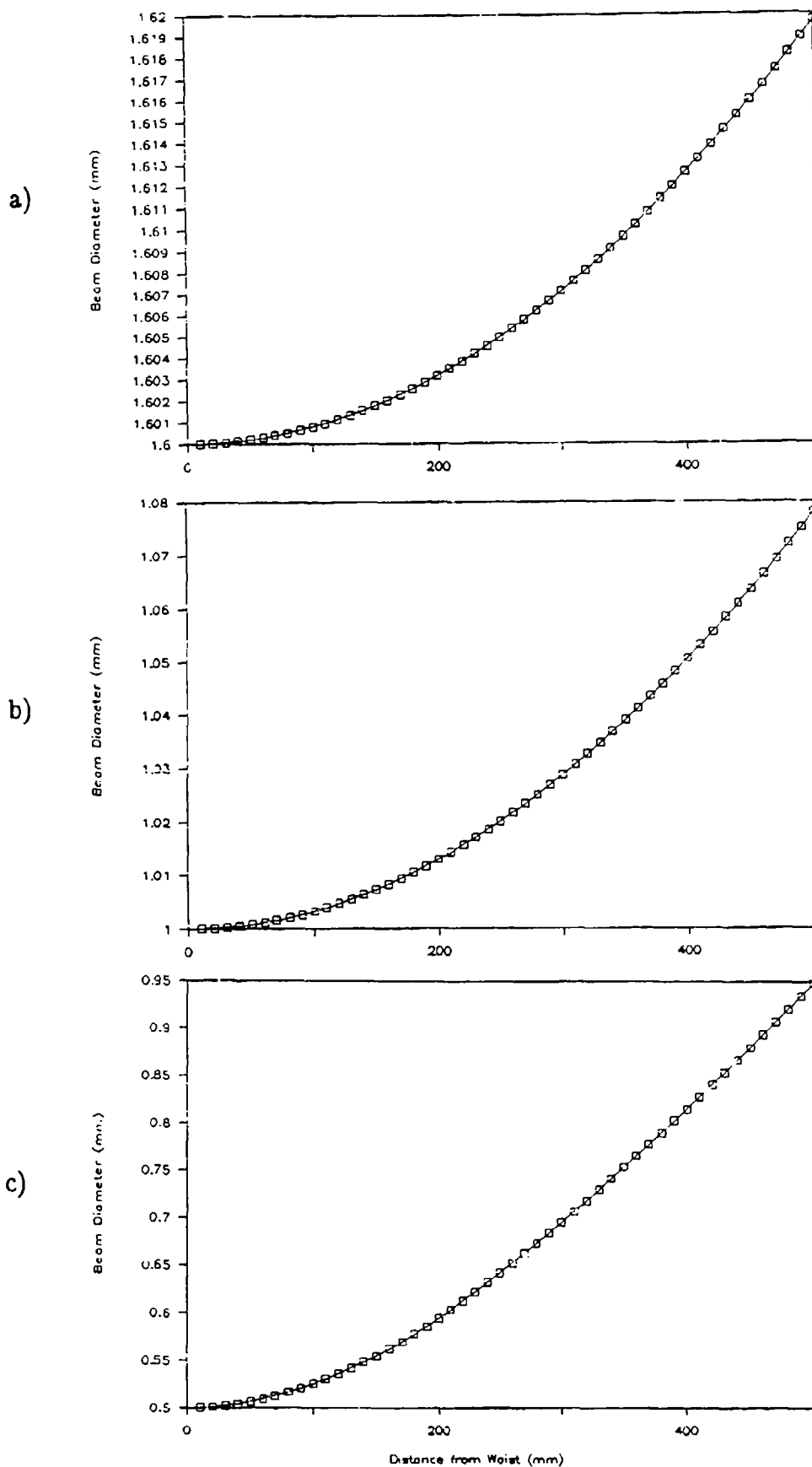


Figure 5.17. Beam diameter as a function of distance from waist location for waist diameters of a) 1.6 mm, b) 1.0 mm, and c) 0.5 mm. 500 mm corresponds to the approximate distance of the anvil surface from the laser aperture.

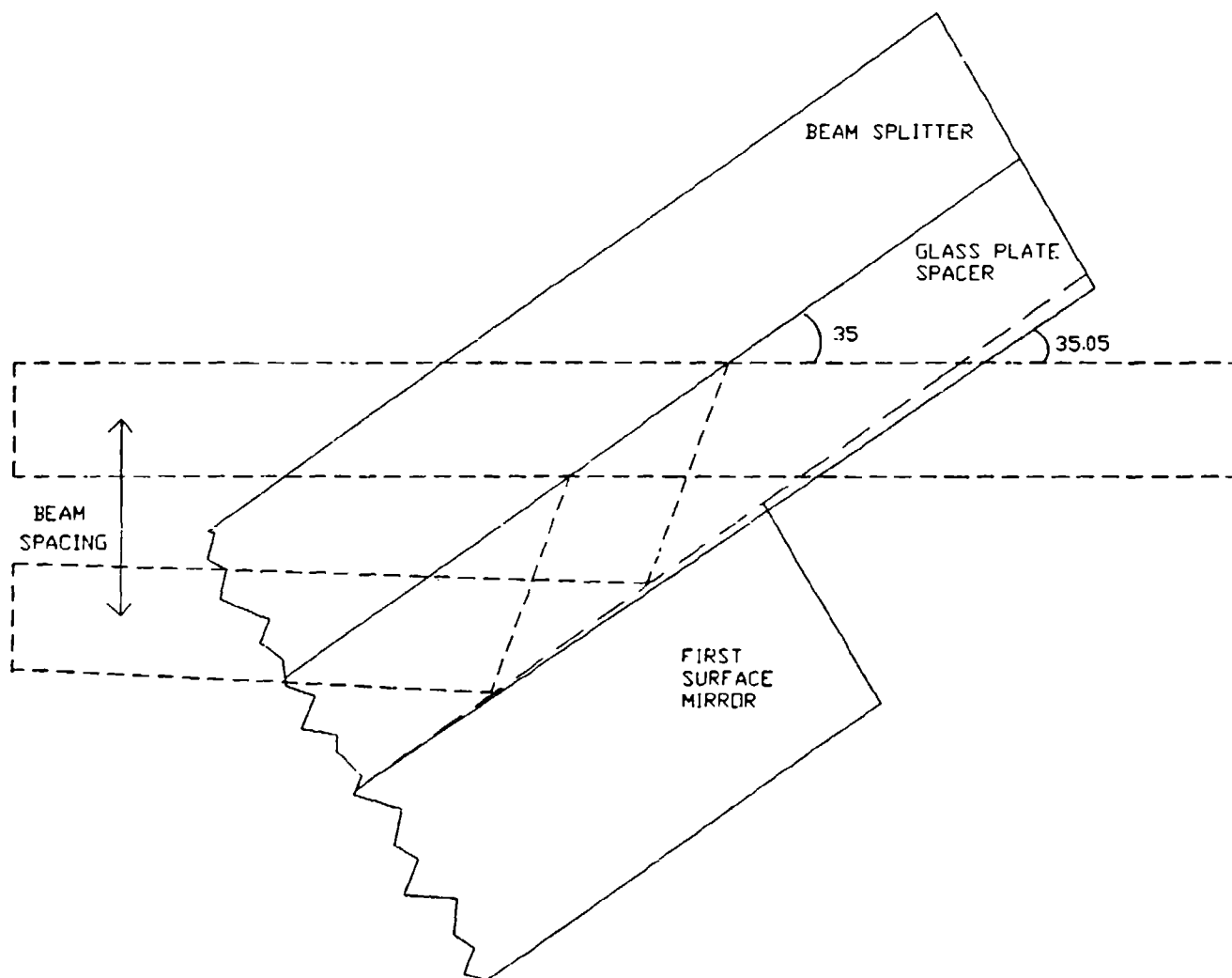


Figure 5.18. Resulting beam spacing if the spacer surfaces are not parallel.

To test the accuracy of these numbers as well as to determine the functional relationship with incidence angle, several tests were performed. Referring to the symbols in Fig. 5.19, first the signal was measured for just the laser beam irradiating the photodiode, and second, with the beam passing through lenses L1 and L2. L1 is a small lens used to focus the beam as small as possible, and L2 is the large plano-convex lens. Both these measurements were greater than 5 V which saturates the oscilloscope. Therefore, a filter (F) was placed at 90° to the beam at the laser aperture. This resulted in a weakening of the beam which produced a signal of 3.5 V ( $= I_0$ ).

The lenses (L1 and L2) were found to absorb 3.5% of the incident light, collectively. The results of the remaining tests are shown in Table 5.6. The I(1) data column refers to tests using the lenses, filter, and the beam splitter. In the I(2) tests, the 1 mm thick spacer was added. When the I(1) results are normalized by the full voltage (3.5 V), the values are consistent with a 25% transmissivity beam splitter considering the absorption by the additional optical components. Also, the spacer absorbs on average 15% of the light (column 3). Similar results were obtained when using the 1.59 and 3.18 mm thick glass spacers.

Table 5.6. Beam transmission measurements.

I(1): F+L1+BS1+L2 (with no BS1,  $I_0 = 3.5$  V)  
I(2): F+L1+spacer+BS1+L2

$\theta, ^\circ$	I(1), V	I(2), V	I(2)/I(1)
32	0.51	0.40	0.78
40	0.60	0.50	0.83
45	0.69	0.59	0.86
50	0.73	0.64	0.88
69	0.85	0.77	0.91
90	0.97	0.86	0.89

### 5.3.1.5 Chopper Wheel Calibrations

To determine the centerline beam spacing as well as the gaps between the beams (gap width increases as the beam diameter decreases), a chopper wheel (Fig. 5.20) was used. The wheel was mounted on a dc motor, and a variac power supply was used to change the rotational speed. By knowing the slit length (24 mm), and determining the times corresponding to when edge 1 and edge 2 break the first beam, a measure of the chopper wheel velocity is obtained. For all measurements the chopper wheel was placed approximately 500 mm from the beam splitter, corresponding to the location of the shotgun/specimen axis in the experiments.



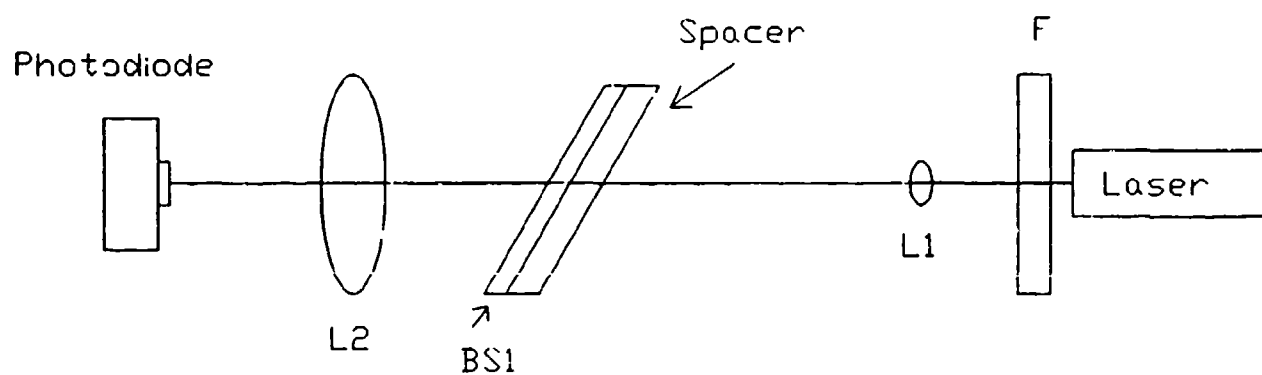


Figure 5.19. Symbols corresponding to beam transmission measurements.

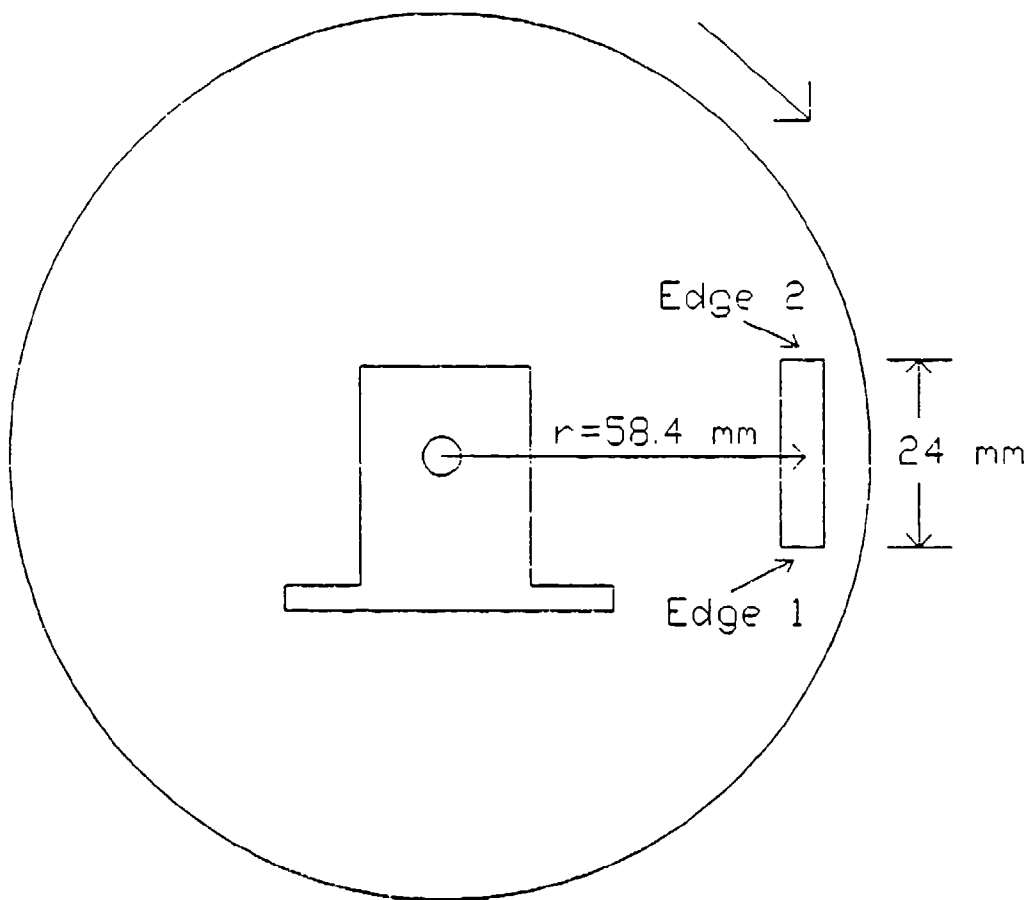


Figure 5.20. Schematic of chopper wheel used in laser obscuration calibration.

### 1 mm Thick Glass Spacer Results

A series of eight beams was generated with the obscuration system at  $45^\circ$ . Traces of photodiode output voltage versus time (Fig. 5.21) indicate plateaus and discontinuities which correspond to the times when the beams are obscured or pass freely through to the photodiode. The velocity increases in each test ( $V_a < V_b < V_c$ ), and the "plateaus" become less distinct. Using the technique described above, a rough estimate for  $V_c$  is 24 m/s, and the plateaus are indiscernible. This result is due to the proximity of the beams to one another using the thin 1 mm spacer. At the experimental impact test velocities of up to 200 m/s, clearly the plateaus will not be seen, and no determination of velocity will be possible. Furthermore, even at  $V_a \approx 1.76$  m/s the plateaus are not sharp enough to determine where in time they begin and end (necessary for measuring the gap widths). The beam spacing is too close for this glass spacer thickness; coupled with the 1.6 mm beam diameter, this spacer cannot be used in this system.

### 1.59 mm Thick Glass Spacer Results

It was observed that from 0 to 150 mm (6") away from the beam splitter and at any incidence angle, a pattern of 6 to 7 distinct beams is generated. However, at locations greater than 150 mm, the beams begin to lose their focus, and by 400 mm become a large blur. At approximately 500 mm, the pattern flips, with the top beam moving to the bottom and vice versa. This is indicative of the non-parallel surfaces of the spacer as discussed previously.

In order to obtain an unblurred pattern, the chopper wheel was moved to within 150 mm of the beam splitter. Results similar to those for the 1 mm spacer were obtained, again indicating no determination of the gap widths or center line beam spacing can be made even at this unrealistically close location and ruling out the use of this spacer also.

### 3.18 mm Thick Glass Spacer Results

Due to the increased centerline beam spacing, the results for the thicker spacer appear reasonable. Fifteen distinct beams were observed, though only nine fit in the chopper wheel opening. With these results, further analysis is possible. A more rigorous technique is used to determine the velocity as follows. Referring to Fig. 5.22, horizontal lines are drawn through the plateaus, and tangents are drawn to the downward sloping lines. At the intersections, projections are made to the x and y axes. The time between intersections ( $t_{\text{transit}}$ ) is fairly repeatable and averages to  $1.2 \pm 0.1$  ms (Table 5.7). For an incidence angle of  $40^\circ$  with the 3.18 mm thick spacer, the centerline beam spacing is 4.15 mm. A more accurate estimation of the velocity is  $(4.15 \text{ mm}/1.2 \text{ ms}) = 3.45$  m/s, a value higher than the estimate of 2.2 m/s calculated using the slit length.

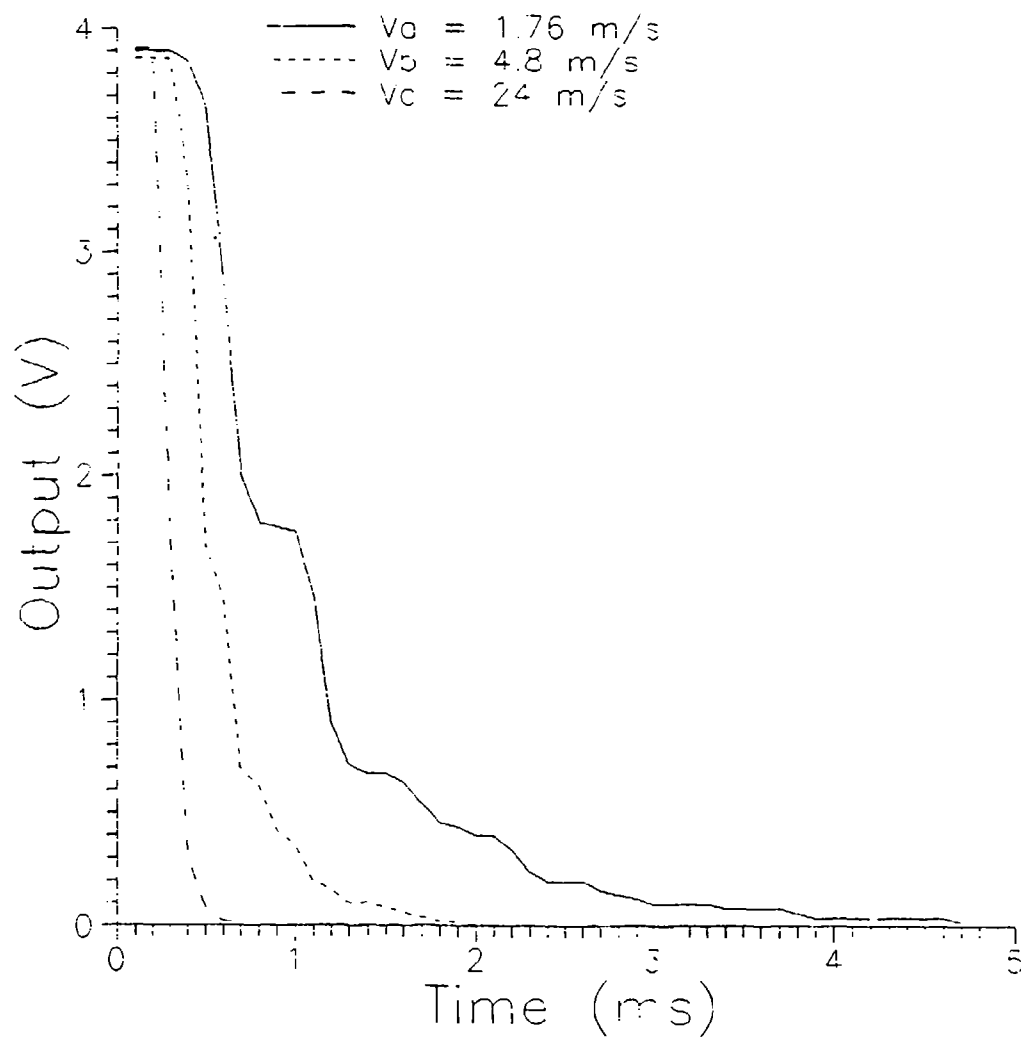


Figure 5.21. Calibration traces for three different chopper wheel rotation speeds.

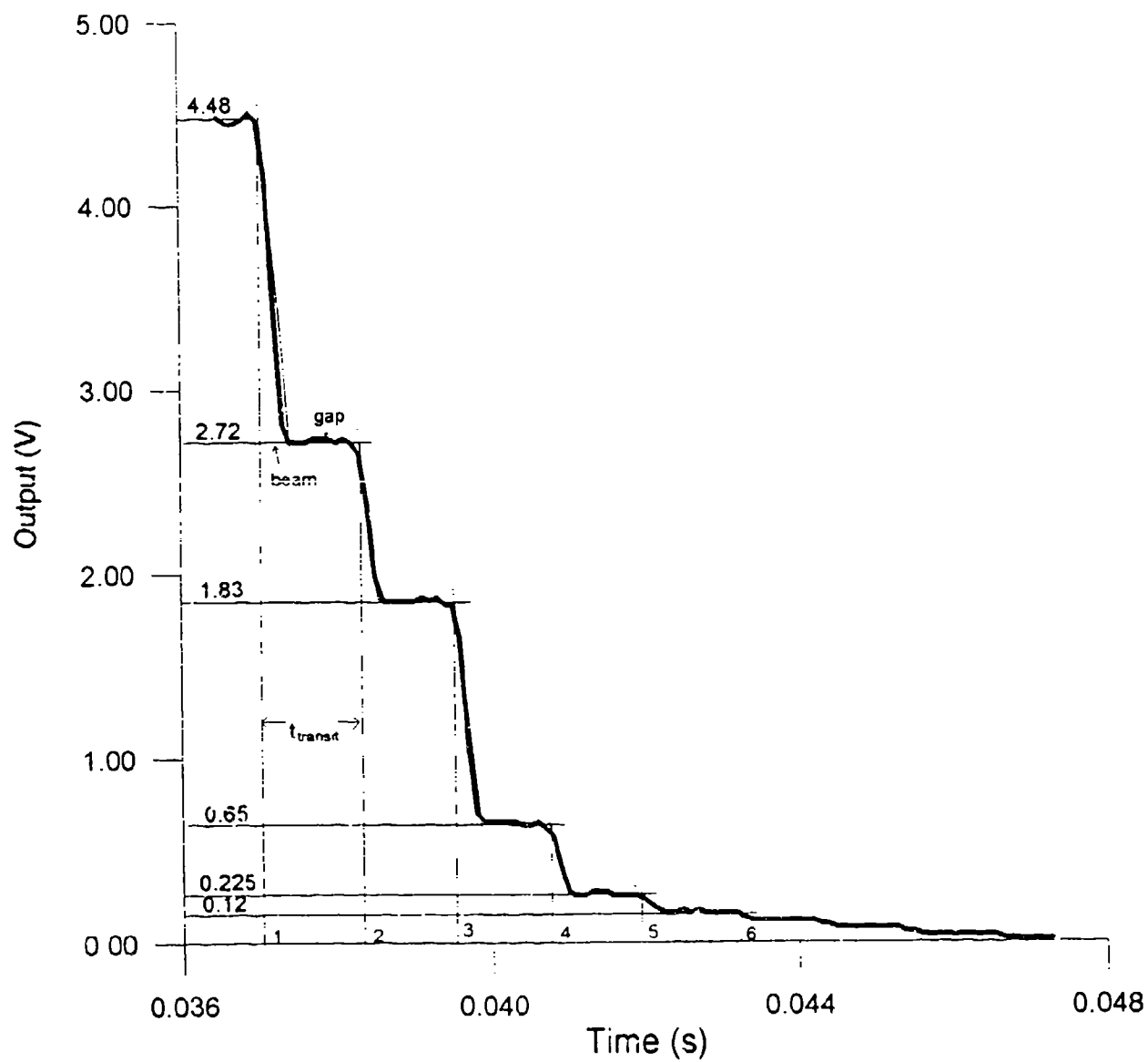


Figure 5.22. Typical obscuration trace indicating data reduction method.

The gap widths (defined in Fig. 5.22) are listed in Table 5.7. The increase from beam 1 to 2 is as expected since the beam diameter decreases with the decrease in intensity. However, the next gap decreases which suggests beam 3 exhibits larger intensity. To explore this further, the intensities of the individual beams were determined. The full signal value of 4.48 V is a measure of the intensity of the nine beams after passing through the optical arrangement, unobstructed by the chopper wheel. The first plateau at 2.72 V represents the signal which remains after the first beam is blocked. Therefore, this beam has a signal value of  $(4.48 - 2.72)$  1.76 V. The remaining values are shown in Table 5.7.

A similar analysis was performed on the raw data results of Fig. 5.23. In this case a slightly higher velocity was produced by increasing the chopper wheel rotational speed. As shown (Table 5.8), the increase in velocity from 3.45 to 8.3 m/s was measured using this technique. For both cases, as expected, beam intensity decreases from 1 to 2, but then increases from 2 to 3, again suggesting a form of constructive interference. This interference is explored with the aid of Fig. 5.14.

Table 5.7. Data corresponding to Fig. 5.22. Velocity = 3.45 m/s.

#	$t_{\text{transit}}$ (ms)	Gap (mm)	Beam (mm)	Intensity (V)
1	1.3	3.36	1.2	1.76
2	1.3	3.55	0.75	0.89
3	1.2	3.36	0.677	1.18
4	1.2	3.17	0.677	0.43
5	1.3	3.14	N/A	0.11
6	0.9	2.69	N/A	N/A
7	1.1	N/A	N/A	N/A
8	1.3	N/A	N/A	N/A

Table 5.8. Data corresponding to Fig. 5.23. Velocity = 8.3 m/s.

#	$t_{\text{transit}}$ (ms)	Gap (mm)	Beam (mm)	Intensity (V)
1	.59	2.97	1.5	1.72
2	.52	3.10	1.1	0.89
3	.48	3.04	0.83	1.17
4	.50	3.04	0.83	0.41
5	.50	3.10	0.968	0.11
6	.50	3.29	0.968	0.05
7	.42	N/A	N/A	N/A
8	N/A	N/A	N/A	N/A

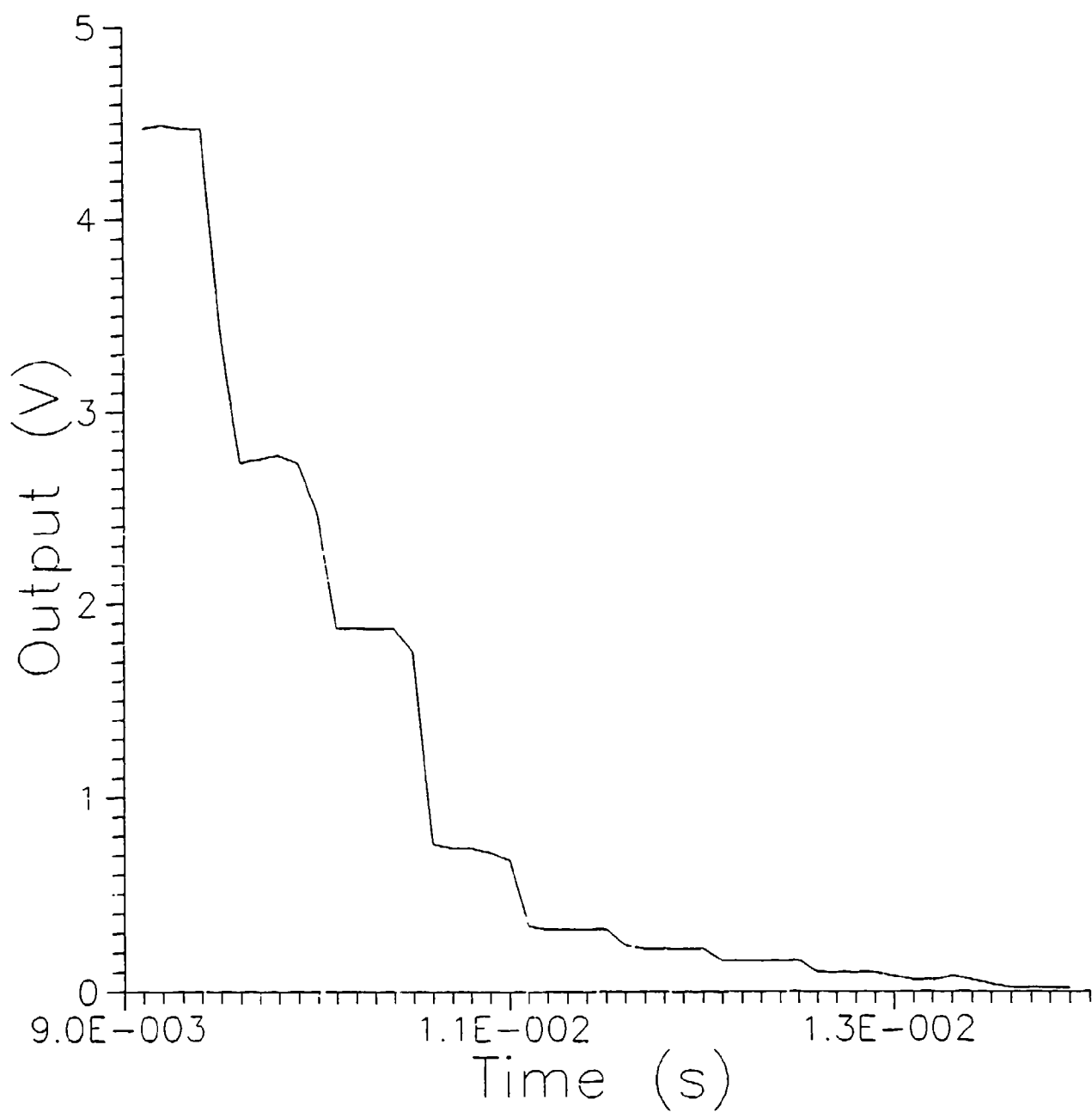


Figure 5.23. Raw data from chopper wheel calibration test at medium rotation speed.

The reflectivities of the interior surfaces of the beam splitter are not known, only the total value of  $\approx 0.83$  at  $40^\circ$ . It is conceivable that a portion of beam 1 (dotted line in Fig. 5.14) is reflected off the inner surface of the beam splitter and constructively interferes with beam 3 as shown. Furthermore, the decrease in intensity from beam 1 to 2 of 51% (Table 5.8) results from the two internal reflections in the spacer (dashed lines). Previously, it was indicated that the spacer absorbs 17% of the incident light (Table 5.6,  $40^\circ$ ) when the light travels through it a distance of approximately  $(3.18 \text{ mm} / \tan 40^\circ) = 3.8 \text{ mm}$ . Therefore, a 100 V initial signal is first reduced to 83 V as it travels through the spacer. Of the 17 V which enters the beam splitter, assuming the reflectivity of the inner surface is 4% (for standard glass surface), 16.3 V is transmitted through as the strength of beam 1. After the initial reflection off the beam splitter, the reflected 69 V signal is reduced to 47 V as it reflects twice internally in the spacer. Then it reaches the beam splitter and is further reduced to 8 V. After the 4% reduction, the predicted signal corresponding to beam 2 is 7.7 V. The predicted ratio of beam 1 to 2 ( $7.7/16.3$ ) of 47% is close to the experimentally observed value of 51%. The difference is most likely due to the absorption of the first surface mirror. The remaining theoretical internal beam structure calculation indicates the beam 3 intensity can be increased due to constructive interference from beam 1 reflecting off the inner surface of the beam splitter. However, the increase (2%) is not significant enough to cause the intensity of beam 3 to exceed the value of beam 2 as found in Tables 5.7 and 5.8. This suggests there may be minute flaws in the glass spacer or beam splitter which absorb and/or reflect a portion of beam 2, thus lowering its intensity.

As a result, more tests were performed in which different locations on the optical surfaces were explored which produced a closer to theoretical intensity versus time signal. After several of these attempts, the "sweet spot" on the optical surface was located. The chopper wheel was then set on maximum rotation speed resulting in the trace shown in Fig. 5.24. The velocity and spacings were determined as before and are listed in Table 5.9.

Table 5.9. Data corresponding to Fig. 5.24. Velocity = 66.2 m/s.

#	$t_{\text{transit}}$ ( $\mu\text{s}$ )	Gap (mm)	Beam (mm)	Intensity (V)
1	67	3.35	1.1	2.64
2	61	3.10	0.97	1.16
3	61	3.14	0.97	0.55
4	61	3.20	0.88	0.24
5	63	3.30	0.84	0.10



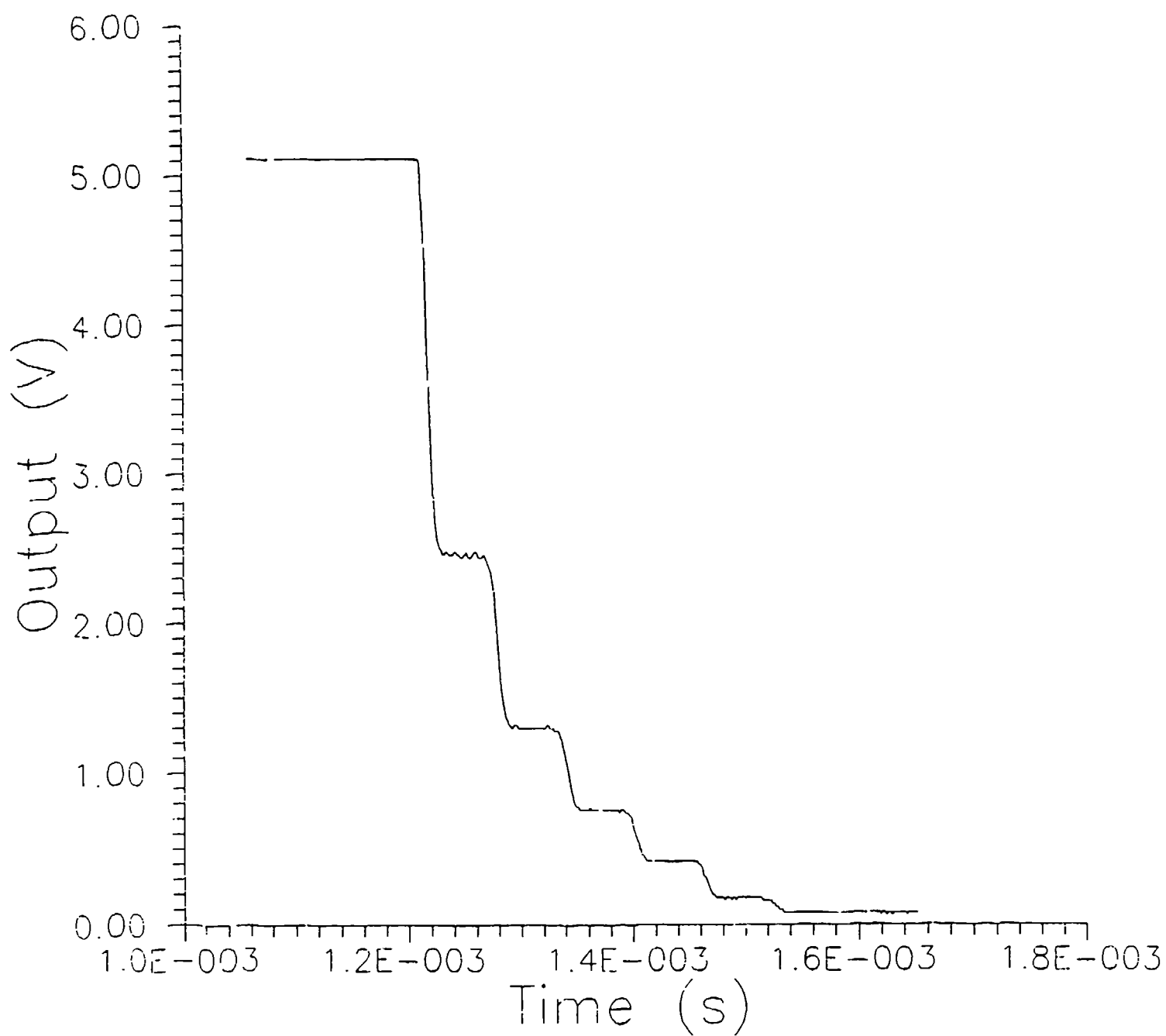


Figure 5.24. Raw data from chopper wheel calibration test at maximum rotation speed.

Note the beam diameter decreases as does the intensity. The average decrease in intensity from beam to beam is nearly constant at 44% of the previous value which is close to the theoretical value of 47% calculated above. Finally, these results indicate the circuit has adequate response time to delineate the individual plateaus corresponding to the beam locations at this maximum chopper wheel velocity of 66.2 m/s. Consequently, response time problems are not anticipated over the 150 to 200 m/s projectile impact velocity range of the actual experiments.

### 5.3.2 PVDF Stress and Reaction Intensity Results

Initial testing efforts involved firing the projectiles over a broad range of impact velocities at various size inert samples. It was discovered that some projectiles shattered at powder loadings designed to produce velocities of approximately 200 m/s and greater. Both the photodiode and stress signals exhibited excessive amounts of randomly scattered peaks resulting from the small plexiglas projectile fragments. Thus all the remaining results are for 1 or 2 grain measured powder loadings (1 grain  $\approx$  0.065 gram) which lead to approximately 150 and 200 m/s impact velocities.

For interpreting the stress gauge results it is useful to contrast this test with a split Hopkinson pressure bar often used to obtain high rate material properties (see e.g., Follansbee and Frantz, 1983) and recently to measure hazard sensitivity of energetic materials (Ho and Fong, 1989). A striker bar (Fig. 5.25) impacts an incident pressure bar and generates a compressive wave. When this wave reaches the specimen, part is transmitted ( $\epsilon_T$ ) and part is reflected ( $\epsilon_R$ ) due to the impedance mismatch at the interface.

The mechanical properties and size of the specimen determine the shapes of these transmitted and reflected waves. By recording the strain-time histories at the gauge locations and accounting for the longitudinal wave transit time, the stress and strain at the specimen ends can be determined. Thus, this test makes use of both reflected and transmitted stress wave information. For proper interpretation, the waves must be one-dimensional.

In contrast, the drop weight experiments made use of just the wave generated from the impact by locating the gauge in the impacting drop weight (Baker, 1994). A gauge in the anvil was initially used, but because the drop-weight gauge results correlated well with accelerometer output at low velocities, the anvil gauge was not used extensively. Modeling efforts by Baker (1994) showed that only for very high impact velocities did the average pressures differ on the anvil and drop weight surfaces.

Since instrumenting the projectile is impossible, the PVDF stress gauge was located in the anvil in the shotgun test thus using the "transmitted" wave. As mentioned earlier, Hopkinson bar theory was in fact used in determining the anvil length and gauge location to ensure the one-dimensionality of the wave. The finite element results (Section 5.2.1) showed

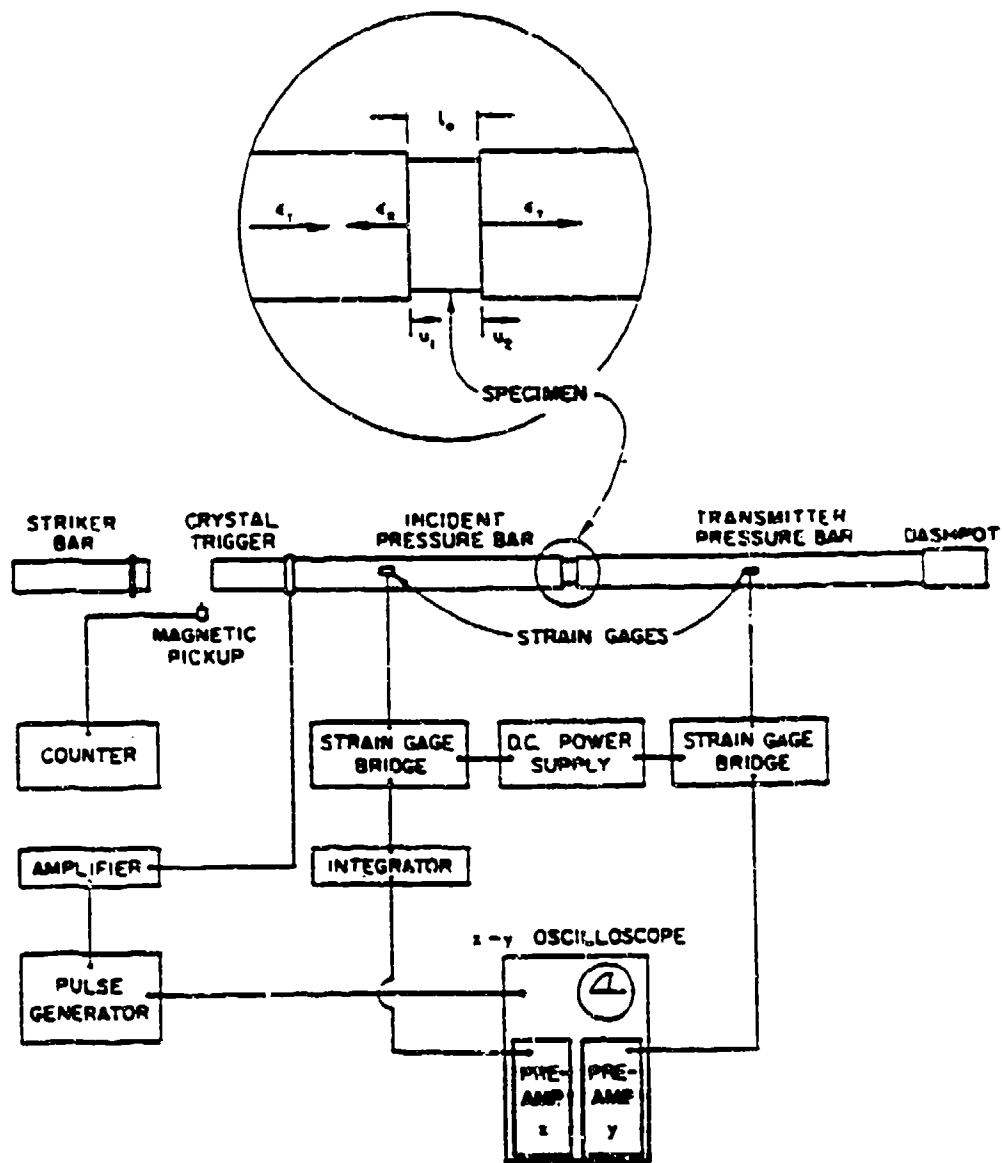


Figure 5.25. Schematic of a split Hopkinson pressure bar (from Follansbee and Frantz, 1983).

this to be true. These differences among the tests bring to light the fundamental problem of using a gauge which records only transmitted stress waves to calculate the energy deposited in the specimen. This method requires almost completely planar impacts, or the one-dimensionality of the wave when it reaches the gauge location is in serious question.

Because the sample absorbs a significant portion of the impact energy, the stress gauge signal is then a measure of the transmitted energy. The projectile does absorb a portion as strain energy, but the modeling showed this amount may be negligible during the first 100  $\mu$ s after impact. These arguments suggest PVDF stress gauge histories with smaller peak values and integrated areas may correspond to more severe reactions (higher intensities on first light traces) since more energy is absorbed by the sample, and vice versa. Initial tests performed on inert samples both to check the laser obscuration system and determine the repeatability of the stress gauge output are discussed before results obtained with live propellants.

#### **5.3.2.1 Inert Samples at $V_0 \approx 150$ m/s**

The laser obscuration signal for a successful test (a217, where the first number (2) refers to the month the experiment was performed, and the second (17) is the day) is shown in Fig 5.26. The descending plateaus indicate a 150 m/s impact velocity followed by a region of near zero intensity (projectile completely obscures beam). The beams are aligned so that when impact occurs, and the projectile is just touching the sample, the highest beam is less than 1 mm from the top surface of the projectile (Fig. 5.27). In Fig. 5.26, this impact time is 574  $\mu$ s, indicated by the sharp rise 1  $\mu$ s later. The post-impact velocity as the sample is crushed is determined from the discernible ascending plateaus. The initial sample length was 12.7 mm (cut from a 0.5" JANNAF class C dogbone specimen). For a beam spacing of 4.5 mm ( $3.18/\cos 45^\circ$ ), two or three beam spacings are the maximum distance the projectile can travel before the sample is completely crushed and the projectile impacts the anvil surface. Calculations indicate the projectile decelerates from 150 m/s to 145, 140, and 128 m/s over the 3 plateaus, respectively. Thereafter the projectile reaches the anvil, and no further values are indicated.

These results indicate the limitations of the current obscuration system. The larger than desired beam diameter (1.6 mm), coupled with the thicker than desired glass plate spacer (3.18 mm), results in a system that is incapable of properly resolving the deceleration of the projectile. Its usefulness for the remaining tests was thus limited to determining impact velocity and indicating quality of impact (planar or oblique) as explained below.

An obscuration trace for an impact with the same powder loading (1 grain) on an identically sized inert sample is shown in Fig. 5.28. Here the descending plateaus are incomplete, indicating the projectile did not pass cleanly through the beams as shown in Fig. 5.29. This suggests an oblique impact on the sample, and in some cases a complete miss, has

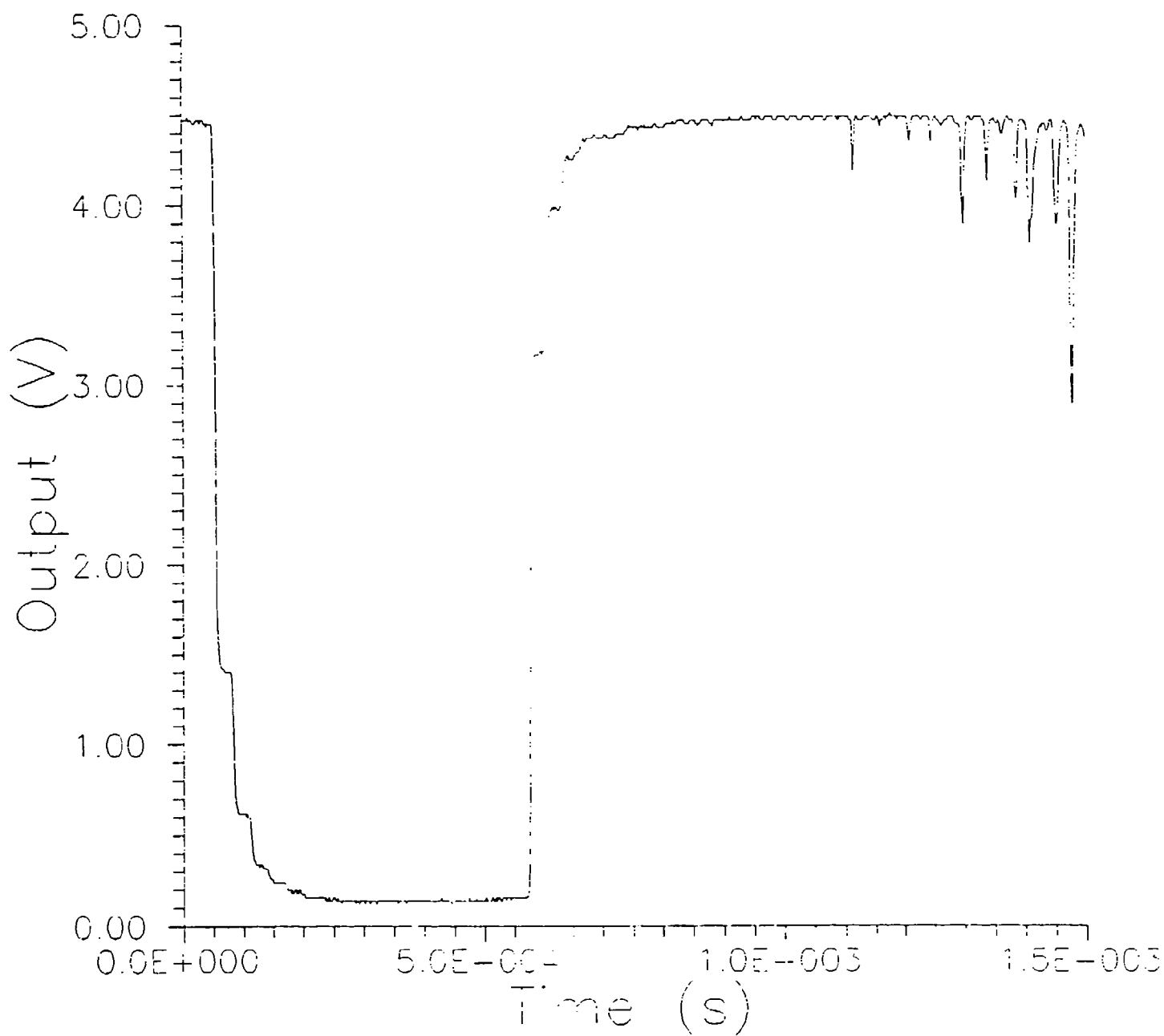


Figure 5.26. Laser obscuration trace for shotgun impact at 153 m/s (case a217) indicating a planar impact.

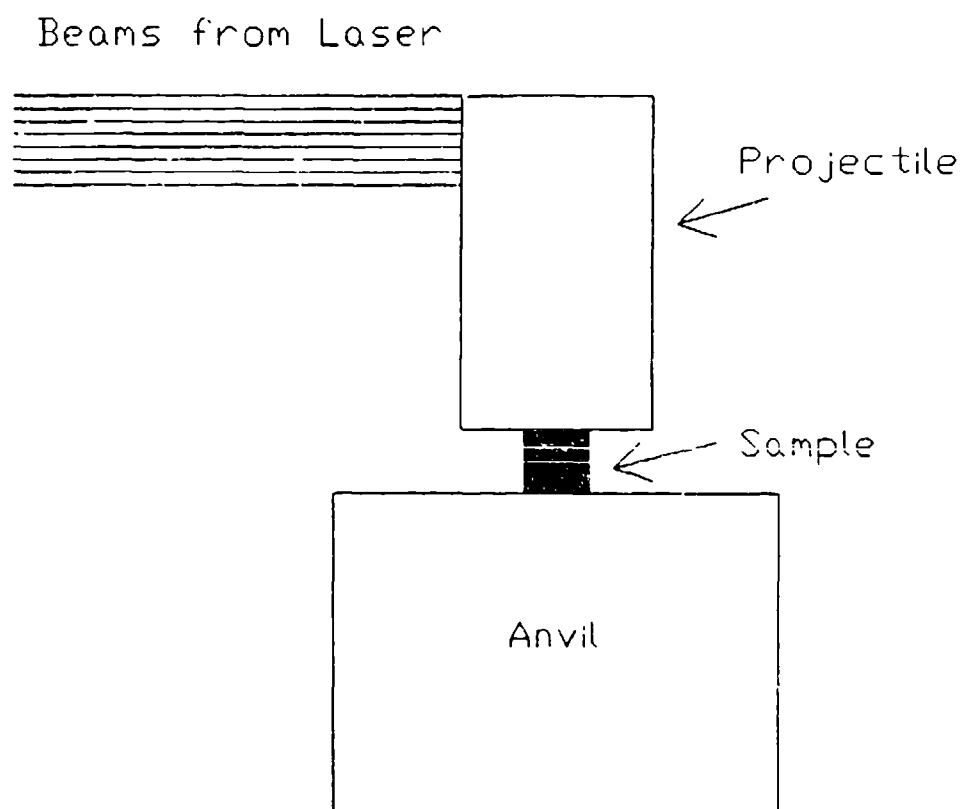


Figure 5.27. Alignment of laser beams with reference to the top of the projectile.

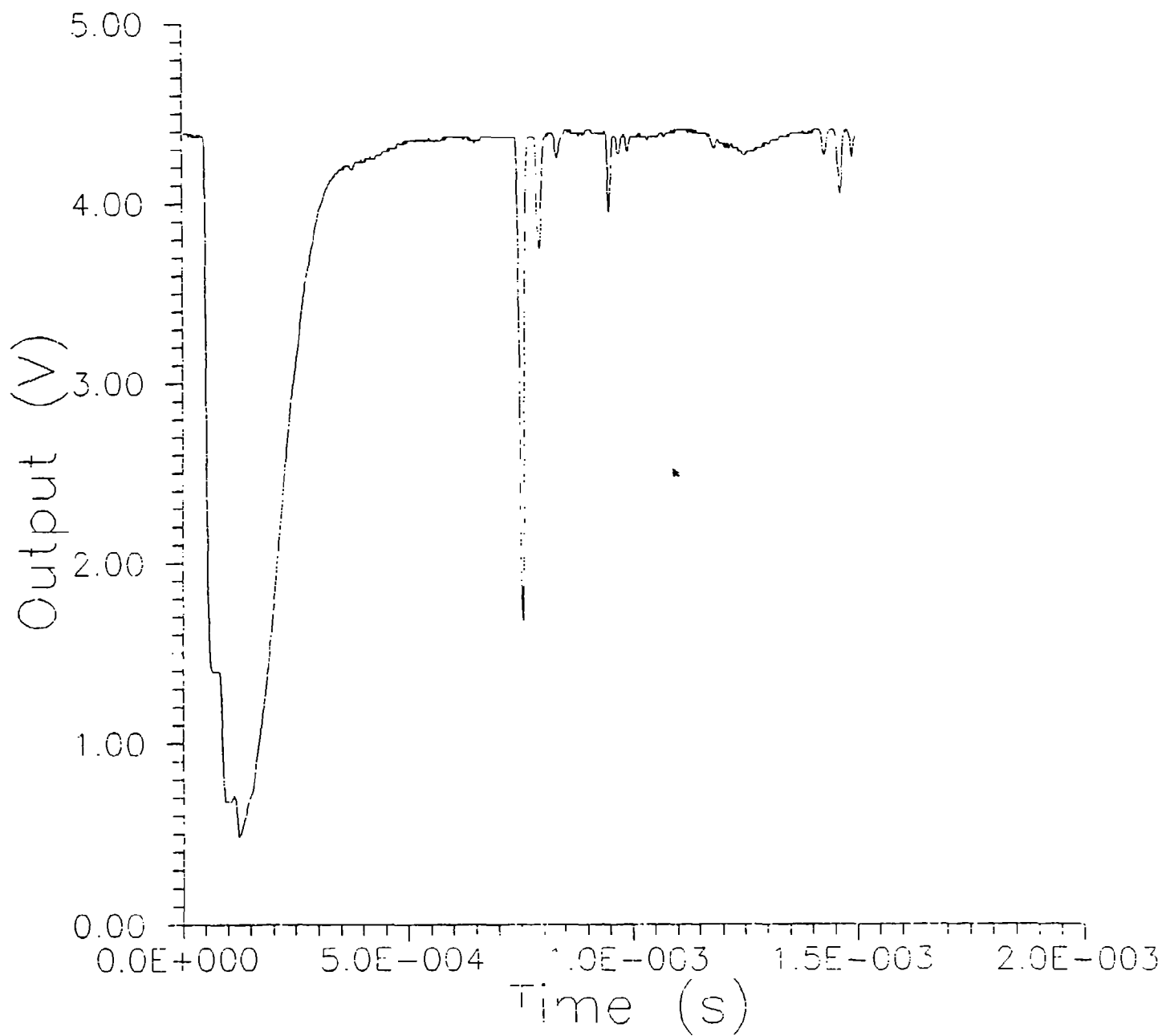


Figure 5.28. Laser obscuration trace for shotgun impact (case d217) indicating an oblique impact.

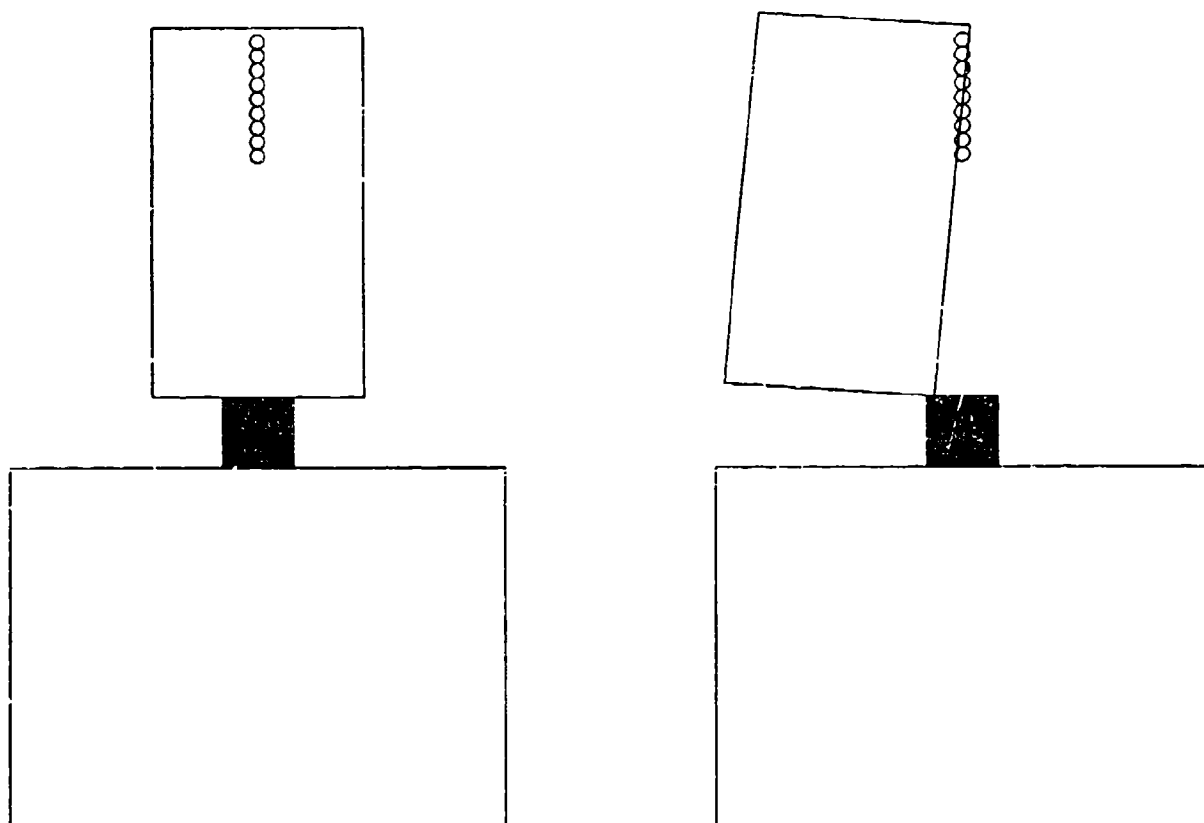


Figure 5.29. Schematics of desired and tilted impacts. The latter results in an incomplete obscuration signal as in Fig. 5.28.



occurred. There are three possible explanations for this phenomenon.

First, the gun may be improperly aligned vertically before it is fired. The alignment is checked with a bubble level before each shot. However, the accuracy of this measurement is at best  $\pm 0.5^\circ$  to the vertical. Extrapolated over the 2 ft (609 mm) distance between the end of the gun barrel and the sample, potentially the projectile could travel 5.3 mm ( $609 \sin 0.5^\circ$ ) off line leading to the partial miss of the lower beams.

Second, when the gun is fired, the recoil may temporarily misalign the barrel and propel the projectile at an off-line trajectory. Though the gun is securely clamped and all possible vibration/absorption dampening measures have been taken, this scenario may in fact be occurring. Without an extensive redesign which time and money did not permit, this potential problem was one that had to be tolerated. However, these type of results occurred in less than 10% of all the tests, suggesting the system was properly aligned the majority of the time.

The third reason may stem from the aerodynamic instability of the projectiles. The flat face may cause the cylindrical projectile to swerve. However, no high speed camera was available to record the projectile flight so this explanation is only postulated.

The probably oblique impacts manifest themselves in the stress histories obtained with the PVDF gauge. Stress outputs for the two previously described cases plus an additional identical case (b317) are shown in Fig. C-1. This third case also was an oblique impact. As expected the stress waves are dissimilar in magnitude and duration for these three different impacts. As a matter of reference, an impact on the bare anvil produced peak stresses of 2.1 MPa and a total wave duration of 25  $\mu$ s. The peak value is well below the suggested maximum allowable gauge stress of 70 MPa for repeated impacts. These results support the finite element results described previously which showed the radial waves in the anvil significantly complicate the correlation between stress at the anvil and that recorded by the gauge. The oblique impacts lead to even more radial wave structure casting doubt on any correlations expected from the PVDF gauge. However, as mentioned, these oblique impacts occurred only about 10% of the time so other cases were evaluated. Lists of tests performed are given in Tables 5.10 and 5.11. The velocity indicated in the second column is determined from the obscuration signals, and the values in parentheses are approximate values for cases where planar or oblique impacts occurred or no valid data were obtained (column 6).

#### 5.3.2.2 Inert Samples at $V_0 \approx 200$ m/s

For two of the three tests on the inert samples at impact velocities of approximately 200 m/s, the laser obscuration traces indicated planar impacts. As a result similar stress histories (Fig. C-2) were obtained. In the third case (e217), no light signal was obtained, and the stress results are slightly different. The initial rise of these three curves is nearly identical for the

Table 5.10. Summary of Inert and Arcadene-360 Cases.

Case	Vel. (m/s)	Sample	Diam. (mm)	Length (mm)	Type of Impact	Rxn. Intensity (V ms)	Max Rxn. (V)
a217	153	inert	10	12.7	planar	N/A	N/A
d217	(150)	inert	10	12.7	oblique	N/A	N/A
b317	158	inert	10	12.7	planar	N/A	N/A
e217	(200)	inert	10	12.7	N/A	N/A	N/A
f217	208	inert	10	12.7	planar	N/A	N/A
c317	194	inert	10	12.7	planar	N/A	N/A
a331	(150)	Arcadene	10	12.7	oblique	0	0
b331	(150)	Arcadene	10	12.7	N/A	0	0
c47	151	Arcadene	10	6	planar	0	0
e47	(150)	Arcadene	10	6	N/A	76	0.52
f421	146	Arcadene	10	6	planar	325	0.51
d331	(200)	Arcadene	10	6	N/A	44	0.48
b47	(200)	Arcadene	10	6	N/A	78	0.5
d47	207	Arcadene	10	6	planar	72	0.58
f47	191	Arcadene	10	6	planar	65	0.52
e421	203	Arcadene	10	6	planar	21	0.4

Table 5.11. Summary of Research Propellant Cases.

Case	Vel. (m/s)	Sample	Diam. (mm)	Length (mm)	Type of Impact	Rxn. Intensity (V ms)	Max Rxn. (V)
e414	148	P3	10	6	planar	2.9	0.17
c421	(150)	P3	10	6	oblique	3.4	0.22
i421	(150)	P3	10	6	N/A	0	0
j421	156	P3	10	6	planar	0	0
a414	204	P3	10	6	planar	20	0.44
d421	201	P3	10	6	planar	3.2	0.22
l421	191	P3	10	6	planar	10	0.31
d414	157	P8	10	6	planar	22	0.27
a421	156	P8	10	6	planar	3.8	0.13
g421	(150)	P8	10	6	N/A	4.1	0.09
b421	193	P8	10	6	planar	15	0.23
h421	203	P8	10	6	planar	252	0.44

first 60  $\mu$ s. Were these live propellants with initiation times less than 60  $\mu$ s, the stress histories would predict similar amounts of energy imparted to the samples. Qualitatively, the peak stresses for these 200 m/s impacts are repeatable and higher than the previous 150 m/s results, suggesting the gauge can sense this difference in velocity. Next, impacts on live propellants were performed.

#### 5.3.2.3 Arcadene-360 Propellant at $V_0 \approx 150$ m/s

For the remaining cases the second oscilloscope was used to record the first light of reaction signal. In the first two cases (Table 5.10) with 12.7 mm long samples, the scopes did not trigger and no signals were recorded. However, both samples were found in two pieces, sheared almost down the center, indicating oblique and/or off center impacts. The collected pieces showed no signs of reaction, indicating pure shear alone cannot initiate these samples. Significant reactions were produced in two additional cases using 6 mm long samples (e47, f421) as shown in Fig. C-3. Fragments collected after these tests showed clear signs of burning at random locations on several pieces. The final two columns of Tables 5.10 and 5.11 list the reaction intensity obtained by integrating the light emission voltage-time traces and the maximum voltage generated.

The corresponding stress histories for these cases are shown in Fig. C-4, and the results are somewhat random. The most severe reaction occurred for f421, but this case had the largest peak stress among the others. Cases a331 and c47 have similar stress histories, yet the sample length has been reduced by a factor of more than two for the latter. Case a331 had a poor obscuration signal (oblique impact) while c47 was likely a planar impact. Since similarly poor results were obtained with the inert samples at 150 m/s, and they improved at 200 m/s, the higher velocity was also attempted for the Arcadene - 360 propellant.

#### 5.3.2.4 Arcadene-360 Propellant at $V_0 \approx 200$ m/s

For these cases medium level initiations occurred in all instances (Fig. C-5) but with varying degrees of severity (Table 5.10). The results of case b47 suggest a strong initial reaction followed by a steady decline to a second reaction at approximately 1.5 ms. Four of the cases have similar maximum reaction levels (Table 5.10) while e421 is slightly lower. Attempts to explain these results with the stress histories (Fig. C-6) are not successful. Though all have similar rise regions the periods of high transmitted stress are different by as much as 50  $\mu$ s, and the peak stresses vary by 50%. Cases d331 and d47 have virtually indistinguishable stress histories, yet d47 has a much stronger reaction history. At least qualitatively, cases b47 and f47 exhibit lower stresses and also two of the more intense reactions compared to the other three cases. As discussed in Section 5.3.2, this may theoretically be the case. At this point,

two of the research propellants from the drop weight experiments were tested to determine their sensitivities to shotgun impact. Due to time and monetary constraints only a limited number of tests was performed.

#### 5.3.2.5 P3 Baseline Research Propellant at $V_0 \approx 150$ m/s

The first research propellant tested was the baseline P3 which has a low solids loading (see Table 5.1). As expected it was much less reactive than the fielded Arcadene propellant. Two cases resulted in very mild initiations (Table 5.11) while the other two showed no reaction. One of each of these results is shown in Fig. C-7. Cases e414 and j421 were similar to cases c421 and i421, respectively, but they are omitted for the sake of clarity of the graph. The stress signals are again misleading in several cases (Fig. C-8). Similar stress curves were obtained for c421 and j421 which were oblique and planar impacts, respectively (Table 5.11). However, the oblique impact (c421) resulted in the mild initiation while the planar impact (j421) did not. Also, the steep initial stress rise of case e414 was in contrast to the other cases which had a more gradual exponential rise. Higher velocity impacts were also attempted on this baseline research propellant.

#### 5.3.2.6 P3 Baseline Research Propellant at $V_0 \approx 200$ m/s

Only three successful runs were obtained for this velocity (Table 5.11), but stronger reactions were recorded (Fig. C-9) than for the 150 m/s cases. Again the stress histories (Fig. C-10) are not very repeatable. All the cases were planar impacts yet showed no similarity in stress magnitude or duration. Furthermore, case d421 had a comparatively weak stress signal yet only initiated slightly (Fig. C-9). When compared to the 150 m/s impacts, similar peak stresses occurred, which is not to be expected. The final propellant tested (P8; Table 5.1) was presumably more reactive due to its higher solids loading (85%) more in line with a fielded munition.

#### 5.3.2.7 P8 Research Propellant at $V_0 \approx 150$ m/s

Of the three cases tested, the reaction varied (Fig. C-11) from a medium level initiation (d414) to a mild reaction (a421, g421). For this propellant, the stress histories (Fig. C-12) predict the opposite of what is expected for the reaction intensities. The strongest and steepest stress (d414) shows the most severe reaction while the weakest stress signals correspond to mild reactions. When compared to the baseline propellant at 150 m/s (Fig. C-4), significantly lower stresses were obtained. This in part is due to the mechanical strength differences between the propellants. The 85% solids propellant (like the Arcadene-360) is much stiffer with a consistency similar to a rubber eraser. The baseline propellant (P3) is softer and gummier (i.e.,

lower modulus) and hence deforms more easily. So for a given strain P3 will have a lower stress and hence lower deformation energy than the P8 propellant. Consequently, more stress is transmitted (Fig. C-8) than compared to the P8 or Arcadene-360 propellants. Finally, two successful runs were obtained with the P8 propellant at the higher impact velocity.

#### 5.3.2.8 P8 Research Propellant at $V_0 \approx 200$ m/s

As expected, the higher impact velocity led to more severe reactions (Fig. C-13) compared to the 150 m/s cases. For the full-fledged ignition (h421, Table 5.11) most of the sample was completely burned with only a few small charred pieces gathered during the post-test inspection. Stress levels (Fig. C-14) are significantly higher than the corresponding P8 cases at 150 m/s, and as before are lower than the P3 cases at 200 m/s (Fig. C-10). The apparent similarity between the initial planar impact stress histories (b421, h421) but yet vastly differing reaction intensities suggests the overall shape of the stress curve may not be a good correlator of the results. Nevertheless, attempts are first made using the stress history output. More important may be the total area under the curve or the area up to the initiation time. These values are determined in the critical energy calculations as discussed in Section 5.3.3.

#### 5.3.2.9 Stress Gauge Correlations

Several attempts were made to correlate the results from the stress gauge with various parameters. One obvious correlating factor is the peak stress, but no repeatable trends with impact velocity were obtained. Also the duration of the wave from zero stress to maximum and back to zero did not correlate the reaction intensity results (Table 5.10). Finally, the loading rate (i.e., the slope of the stress curve from time zero to the time at the peak level) was evaluated as a correlating factor and was also unsuccessful. For example, cases b421 and h421 had nearly equal loading rates, yet the former only slightly reacted while the latter showed a strong ignition response. The loading rates ranged from  $1 \times 10^{-2}$  to  $5.5 \times 10^{-2}$  MPa/ $\mu$ s and did not correlate the go/no go behavior or reaction severity except in a limited number of cases. The poor quality of the stress histories casts doubt on any possible correlations, especially with critical energy calculations desired from the start of this shotgun program. However, for completeness the critical energy calculations are presented below.

#### 5.3.3 Critical Energy Calculations

Currently, nearly all critical energy data have been determined with drop-weight impact machines (Baker et al., 1990, 1991; Coffey et al., 1986). Velocities and HTPB/AP propellant initiation delay times are on the order of 10 m/s and 100  $\mu$ s, respectively. For longer

delay times the assumption of negligible elastic energy storage in the machine is in doubt, as suggested by the finite element results of Section 5.2.3. Data of Baker et al. (1990) and Coffey et al. (1986) were obtained with HTPB/AP/Al propellants and an explosive containing mostly HMX with an inert polymer binder. The lower ignition velocities for the HMX explosive are a function of the formulation and/or increased drop-weight mass in the Coffey et al. tests. As discussed in Baker et al. (1990) the data for the propellants show different trends of critical energy with impact velocity. The shotgun test was used to determine the trends over higher impact velocities. Limited critical energy data were presented for the Coffey et al. (1986) shotgun test.

The analysis methods developed for the drop-weight test are applied to the shotgun test. Calculation of critical energy for the shotgun experiments can theoretically be done with or without the velocity history of the projectile. Both methods require the energy balance equation discussed earlier:

$$W_S = \left| \Delta E_{P,K} + \Delta E_{P,E} + \Delta E_{A,K} + \Delta E_{A,E} + \Delta E_{S,K} \right| \quad (5.7)$$

For either method the elastic and kinetic anvil energies are determined from the PVDF stress gauge data. When the stress from the impact reaches the PVDF gauge it can be assumed uniform over the surface of the anvil, as suggested by the results in Fig. 5.6c. The elastic and kinetic energies of the anvil at the time of first reaction are

$$\Delta E_{A,K} = \Delta F_{A,E} = \frac{1}{2} \int_{t_{\text{DELAY}}}^{t_{\text{DELAY}} + t_{\text{REACTION}}} A_A \frac{\sigma(t)^2}{\rho_A C_A} dt \quad (5.8)$$

where  $t_{\text{DELAY}}$  is the wave travel time from impact to the gauge ( $\approx 60 \mu\text{s}$ ),  $A_A$  is the anvil cross-sectional area ( $3.167 \times 10^{-3} \text{ m}^2$ ),  $\rho_A$  the anvil density ( $7.8 \text{ g/cm}^3$ ),  $C_A$  the elastic wave speed ( $5274 \text{ m/s}$ ),  $\sigma$  the measured transmitted stress, and dispersion is neglected. The stress also gives the strain, displacement, and, hence, velocity of the top surface of the anvil as a function of time. The elastic and plastic deformation of the PMMA are neglected in both methods.

In the first method, where the velocity history of the projectile is known, the PMMA kinetic energy history is easily computed, and the sample kinetic energy is computed from the anvil and PMMA velocities (sample kinetic energy may be significant in the shotgun test). Thus, the critical energy can be computed from Eq. (5.7). However, as indicated earlier the present obscuration system is not capable of resolving the critical post-impact velocity history so an alternative method is used.

In the second method, the analysis of Baker and Mellor (1992) can be adapted to find the velocity. The projectile is assumed a rigid mass and the pressure exerted on it by the sample determines the velocity. For the Baker and Mellor analysis the drop-weight pressure  $P_w$  is related to the anvil pressure  $P_A$  by

$$P_w = P_A / (1 + \frac{1}{2} M_S / M_A) \quad (5.9)$$

where the anvil was assumed to have infinite mass.  $P_w \approx P_A$  for the sample and anvil size chosen here. This pressure ( $\sigma(t)$ ) determines the velocity of the projectile which gives its kinetic energy and the kinetic energy of the sample. A derivation of the resulting equations is given in Appendix D. The integrations are performed numerically in a spreadsheet using Simpson's Rule.

One immediate observation that can be made is that friction will have a smaller effect on the shotgun test than in the drop-weight test because the sample thickness is so much greater in the former. However, caution should be used when applying the Baker and Mellor analysis. The rigid mass assumption begins to break down if the reaction time is less than required for achieving vibrational equilibrium in the projectile ( $\approx 50 \mu s$ ).

A typical result from the critical energy calculations is shown in Fig. 5.30. At the reaction time the majority of energy transferred is from the change in projectile kinetic energy. Sample kinetic energy is only 3% of the total work done on the sample. For all cases the change in anvil elastic and kinetic energies was negligible compared to the other energy storage modes. These calculations were performed out to the time corresponding to the end of the stress history of the initial loading and unloading wave, which had an average duration of 100  $\mu s$  from impact to the first zero crossing. If longer times were evaluated, higher values would be predicted since the total stress history oscillates, as shown in Fig. 5.31 for case f47. The other signals are also included, and the time axes have been shifted to account for pre-set oscilloscope delays and elastic wave transit times so all curves are in real time to the best approximation. The rise on the laser signal corresponds to impact, and the stress rise begins. At some later time, the first light initiation begins. Time from impact to first light is the reaction delay time. For this case the delay time of 36  $\mu s$  occurred during the rise period of the stress wave. The remaining cases are listed in Table 5.12. In column four, the reaction times are listed and  $W_s$  and  $W_s/m_s$  ( $m_s$  = propellant sample mass) correspond to this reaction time. In the last three columns the values correspond to the first loading and unloading stress waves as discussed in Section 5.3.2. With the exception of Case c421, the Arcadene-360 propellant reaction times all occur before the peak stress value.

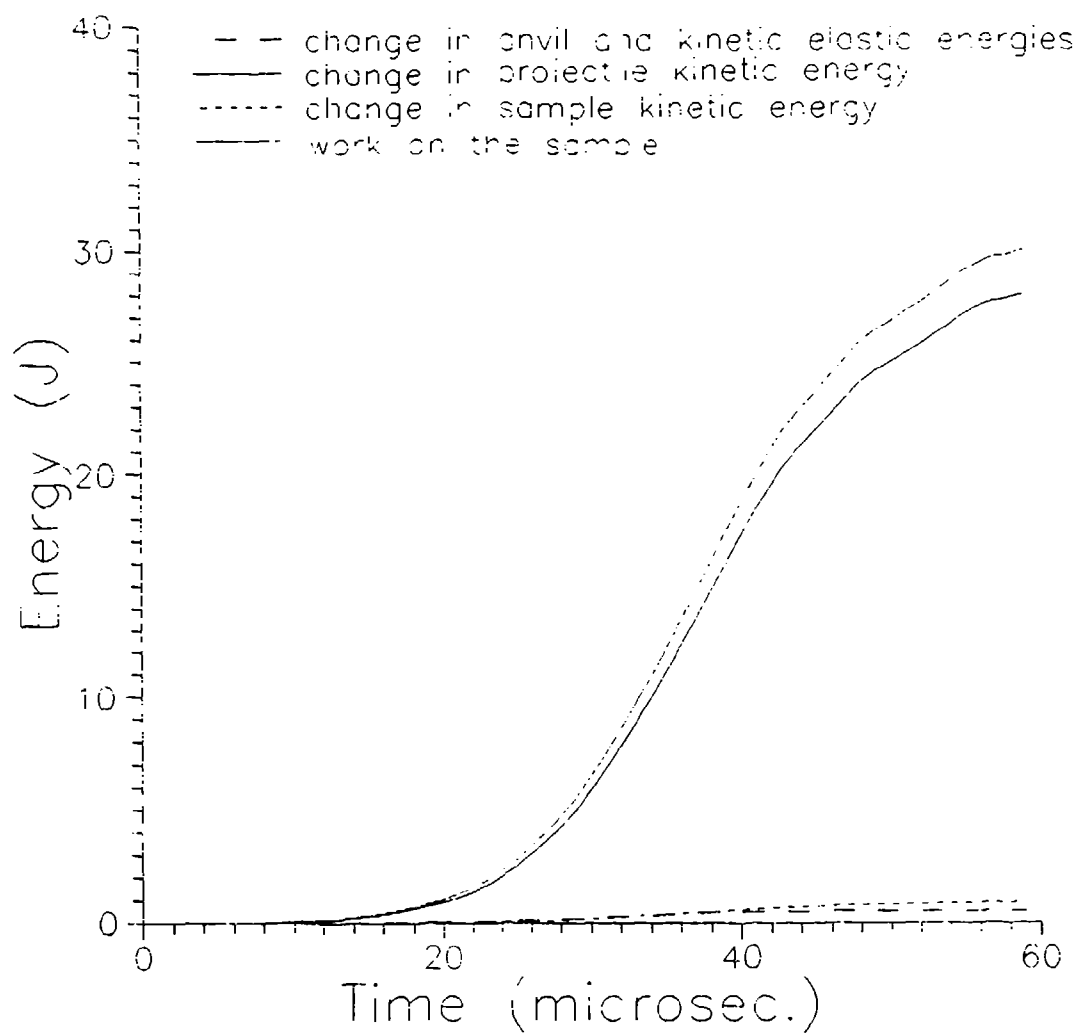


Figure 5.30. Typical calculated energy distribution (case f47).



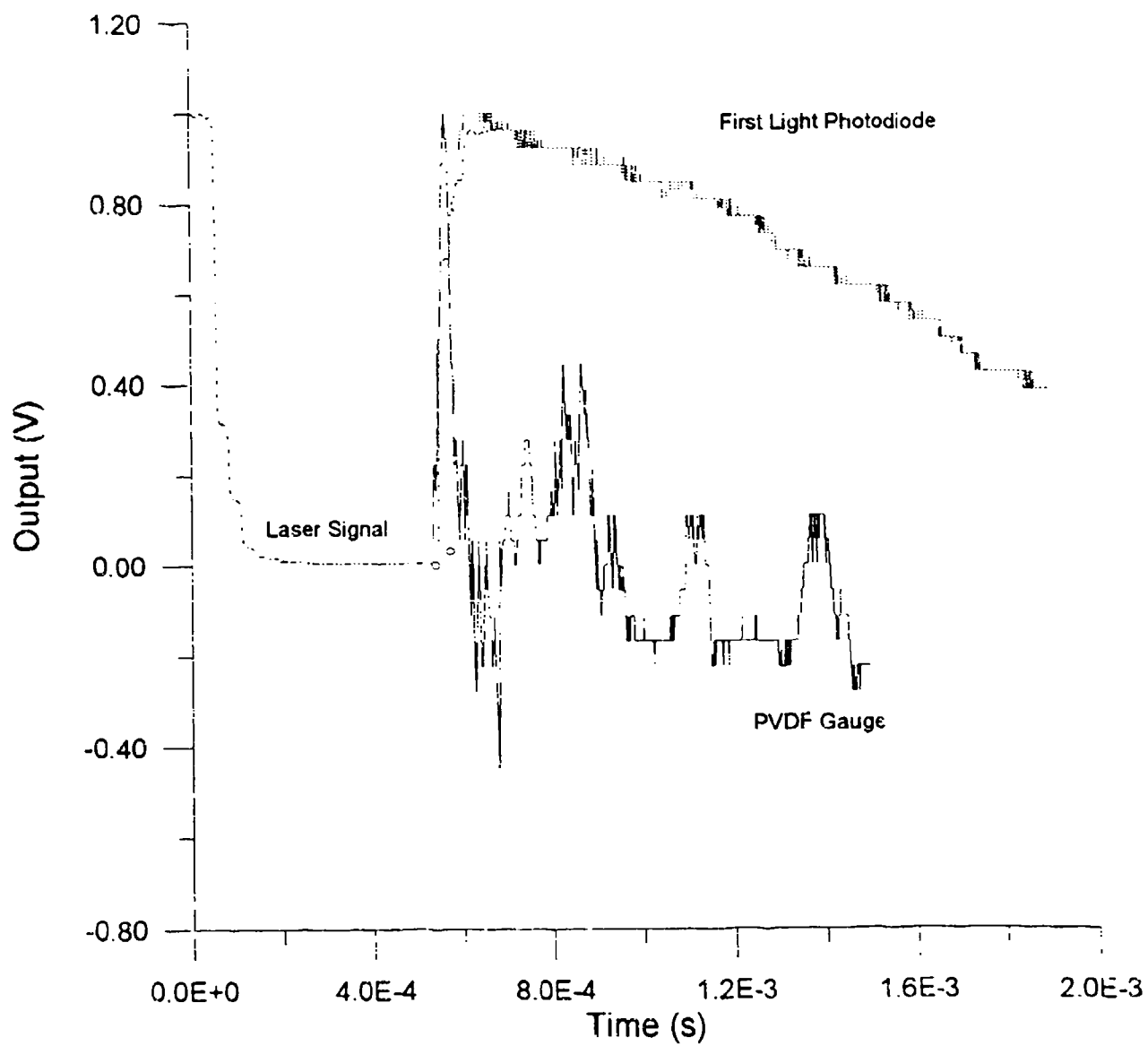


Figure 5.31. Composite of all three signals shifted in time.

Table 5.12. Summary of Energy Calculations.

Case	Vel. (m/s)	R <sub>AM</sub> Intensity (V ms)	t <sub>ren</sub> (μs)	W <sub>s</sub> (J)	W <sub>s</sub> /m <sub>s</sub> (J/g)	t <sub>wave</sub> (μs)	W <sub>wave</sub> (J)	W <sub>wave</sub> /m <sub>s</sub> (J/g)
Arcadene-360								
a331	(150)	0	N/A	N/A	N/A	52	90	105
b331	(150)	0	N/A	N/A	N/A	112	43	50
c47	151	0	no	N/A	N/A	93	96	112
e47	(150)	76	55	2.7	3.1	122	92	107
f421	140	325	43	11	13	74	59	68
d331	(200)	44	57	52	60	91	87	101
b47	(200)	78	36	7.2	8.3	102	29	93
d47	207	72	44	0.7	0.8	125	90	104
f47	191	35	36	13	15	59	30	95
e421	203	21	132	132+	153+	121	132	153
P3								
e414	148	2.9	145	129+	149+	65	129	149
c421	(150)	3.4	138	101+	117+	97	101	117
i421	(150)	0	N/A	N/A	N/A	99	124	144
j421	156	0	N/A	N/A	N/A	99	129	149
a414	204	20	160	188+	218+	98	188	218
d421	201	3.2	153	61+	71+	59	61	71
l421	191	10	262	123+	148+	116	128	148
P8								
d414	157	22	225	71+	82+	116	71	82
a421	156	3.8	219	40+	46+	132	40	46
g421	(150)	4.1	235	47+	55+	148	47	54
b421	193	15	64	53	61	92	115	130
h421	203	252	76	75	85	90	85	98

The reaction times for the P3 propellant are all significantly past their corresponding peak stress times. For the higher velocities the P8 reaction times are near or slightly past the times for peak stress. Coffey et al. (1986) suggest if reaction occurs after the peak value, significant elastic anvil and impactor energy storage make the critical energy assumptions invalid.

Expected trends with critical energy are as follows. In the drop weight impact tests on the smaller samples (1.2 mm thick, 5.3 mm diameter), a general trend of decreased critical energy with increased weight percent AP was observed (Baker, 1994). For the three propellants tested in the shotgun experiment the following results were found at a baseline impact velocity of 10.5 m/s. The Arcadene-360 had a critical energy of  $111 \pm 27$  J/g which

increased with decreasing sample diameter and was independent of sample thickness and impact velocity. The P3 propellant had a critical energy of  $293 \pm 106$  J/g which also increased with decreasing diameter, was independent of sample thickness, but showed a slight increase with decreasing impact velocity. Finally, P8 had a critical energy of  $171 \pm 53$  J/g that increased with decreasing impact velocity.

For the shotgun tests in which the samples are much longer (6 mm) and wider (10 mm), the larger diameter would decrease the critical energy if in fact friction plays a large role as in the drop weight tests. The computed friction area to volume ratio for the drop-weight specimen is five times the value for the shotgun. The sample length effect remains unclear based on the drop-weight results. However, 12.7 mm Arcadene samples did not initiate at 150 m/s while a shorter 6 mm sample at the same velocity had the strongest reaction of any case tested.

Neglecting changes in sample geometry and accounting only for the large increase in impact velocity, the critical energies should be the same, less than and less than the corresponding drop weight values for Arcadene, P3 and P8, respectively. However, only in one set of data did these expectations hold true.

For Arcadene-360, the average of the critical energy density values in Table 5.12 (column six) is 16.7 J/g. The P3 values in Table 5.12 are not directly comparable since initiations occurred well past the peak stress location. For the P8 propellant no valid data were available at 150 m/s, but for 200 m/s the average value of the two cases (73 J/g) is less than the corresponding drop weight value and agrees with the predicted trend.

In the related shotgun experiment of Coffey et al. (1986), the average critical energy density for an unspecified binder/AP propellant was 61 J/g for the combined shotgun and drop weight tests ( $V_0$  range from 1.4 to 169.6 m/s) but higher (111 J/g) for the shotgun results only ( $V_0$  from 69.1 to 169.6 m/s).

An alternative method of correlating the results is based on the discussion in Section 5.3.2 where it was suggested the lower transmitted anvil stresses should correspond to stronger reactions and vice versa. Accordingly, a plot of the integrated transmitted stress density ( $W_{\text{wave}}/m_s$ , Table 5.12) versus integrated light intensity (Rxn. Intensity, Table 5.12) for all the propellants is shown in Fig. 5.32. A poor correlation coefficient ( $R = 0.24$ ) results. However, the expected trend occurs. In light of the previous discussions, the cases which had reaction times greater than their corresponding times of peak stress were removed from the correlation. This correlation (Fig. 5.33) shows improvement the correlation is still not statistically significant. Attempts were also made using results for each impact velocity, but the correlations were worse.

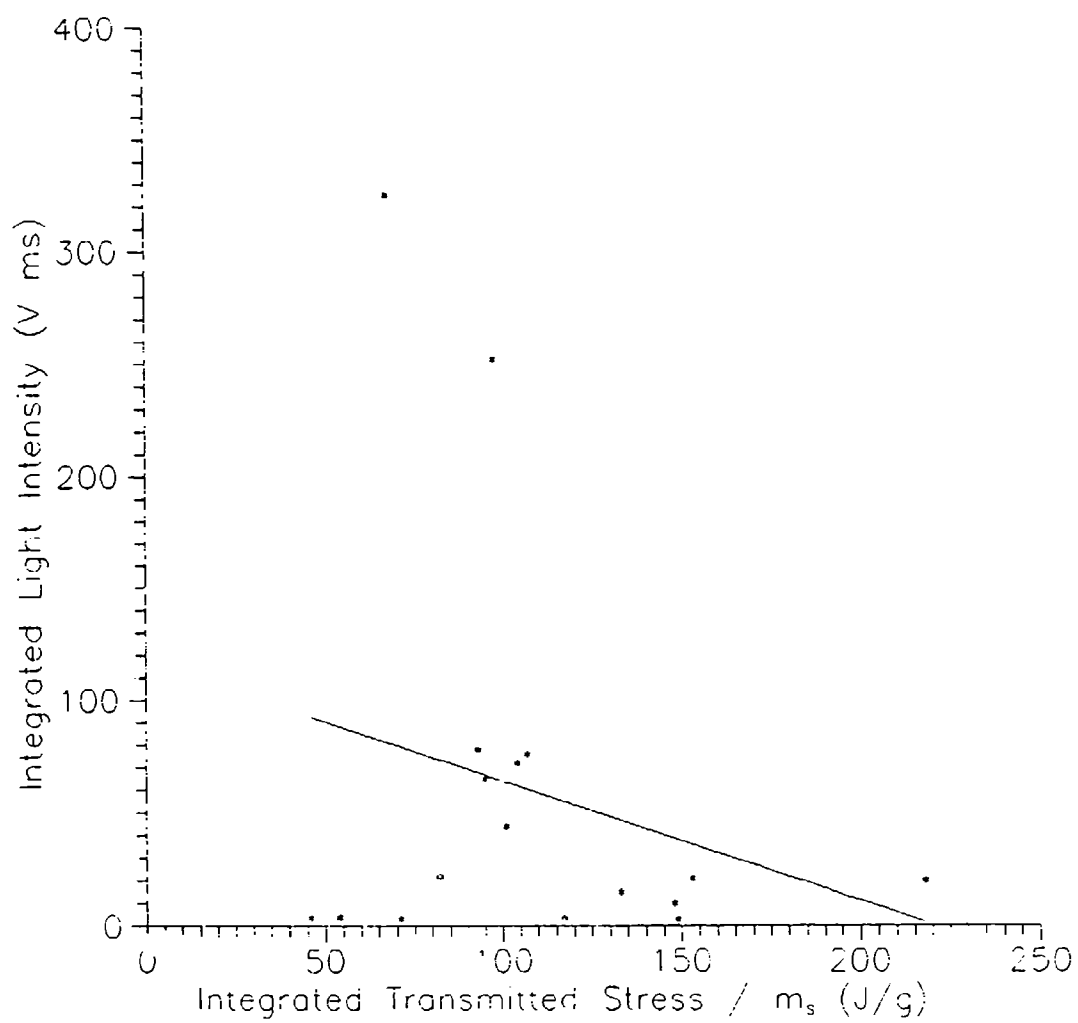


Figure 5.32. Correlation of stress density and light intensity for all propellant data.

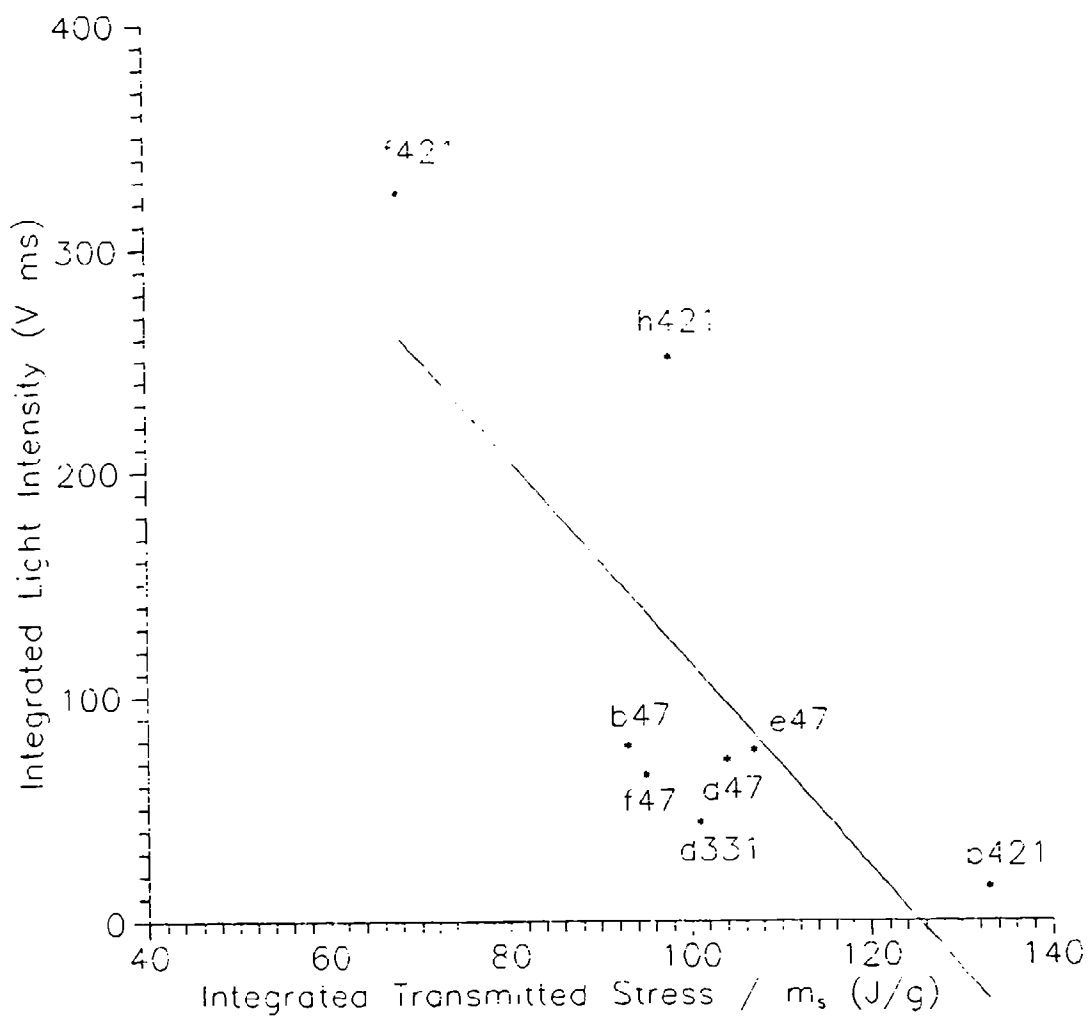


Figure 5.33. Correlation of stress density and light intensity for cases where reaction occurs before peak stress level is reached.

#### 5.3.4 Summary of Important Results

This experimental program was a one-year extension to the recently completed drop-weight impact program. One focus of the work was to determine the feasibility of a new technique, laser obscuration, for measuring the velocity history of a projectile as it impacts and crushes a small propellant sample. With a borrowed laser that has a larger beam diameter than desired and using commercial grade optical components, the following conclusions are drawn.

Due to the large beam diameter and slightly non-parallel optical surfaces, the minimum centerline beam spacing which can be generated is approximately 4.5 mm. This is sufficient for measuring the projectile impact velocity but does not provide adequate resolution for determining the crucial post-impact velocity, which was its intended purpose. Recall that the length of the cylindrical specimens selected initially was 12.7 mm, but since the first two Arcadene-360 tests with samples of this size at 150 m/s showed no reaction, this length was decreased to 6 mm (see Table 5.10).

The light detection system used to determine the severity of and time to reaction worked well and generated useful information for a series of shotgun impact tests at  $\approx 150$  and 200 m/s on three different HTPB/AP solid rocket propellants.

PVDF stress gauges were shown to be reliable devices for determining critical energies in the drop-weight tests (Baker, 1994). However, their performance in the shotgun tests is not as clear. Qualitatively, they can detect changes in both impact velocity and propellant type. But the experimental arrangement necessitated that the waves recorded by the gauge are one-dimensional in order for proper signal evaluation. The stress gauge output was interpreted accordingly.

Because the velocity history was not available from the obscuration system, it was estimated from the stress gauge output as shown in Appendix D. Many assumptions were made here which cast doubt on the quantitative critical energy density values obtained. The calculated values qualitatively support the lower velocity drop-weight results for the three propellants tested. For two of the three propellants, critical energy density ostensibly decreased at the higher shotgun impact velocities compared to the drop-weight results. But due to the limited number of data obtained, this should not be construed as a result with a high degree of certainty.

Finite element modeling with DYNA2D proved a useful tool for analyzing various aspects of the shotgun test. Most importantly it showed that the transmitted wave is one-dimensional when it reaches the gauge location if a planar impact generates the wave. However, several problems result from using DYNA2D to model the shotgun impact test.

Before additional modeling is done, the problems associated with this code should be addressed. Of particular importance is the slideline model used for the sample/anvil and sample/projectile interfaces. Friction is the controlling variable for the drop-weight test (Baker, 1994), and although it may not be as important in the shotgun test due to the larger sample size, without a method for correctly incorporating friction into the model, quantitative results cannot be expected.

### 5.3.5 Recommendations

In order for a next generation shotgun test to yield better results, the alignment of the entire system must be improved. A one-piece unit in which the gun barrel and anvil impact surface are always rigidly locked in the same position would remove some of the uncertainty regarding the planarity of the impact.

Other projectile materials should be examined since the plexiglas often shatters at velocities greater than about 250 m/s. Possible thermoplastic material replacements include nylon or acetals for their improved ductility and dimensional stability (Smith, 1986).

Incorporating strain gauges on the anvil would allow a Hopkinson bar type analysis and serve as a calibration for the PVDF gauge provided the waves are one-dimensional. Strain gauges are available at reasonable cost ( $\approx$  \$100) which can handle this task (Mallard, 1993).

A 10 mW laser from Edmund Scientific (Model NG1.834, \$1350) with a beam diameter of 0.68 mm and divergence of 1.2 mrad ( $0.07^\circ$ ) is just one example of a laser which apparently falls within the required constraints of the obscuration system design. A tradeoff exists between the thickness of the spacer and the amount of information which can be obtained from using it. What must be kept in mind is the desired measurement of the post-impact velocity of the propellant sample/projectile interface. It is possible to obtain a high-grade, custom-designed optical unit with a beam splitter, 1 mm spacer, and first surface mirror all of sufficient flatness for approximately \$1000 (Spindler-Hoyer, 1994). A unit such as this would facilitate the critical beam alignment. Using a 0.68 mm beam diameter and an incidence angle of  $45^\circ$  results in a 1.92 millimeter centerline beam spacing (Eq. (B.6)). At the location  $z = 500$  mm where the projectile breaks the beams, the beam radius is 0.45 mm (Eq. (5.6)). The gap between two successive beams is  $(1.92 - 2 \times 0.45 =) 1.02$  mm which does not present a resolution problem. However, in light of the experimental results in which 6 mm thick samples must be used, only three measurements could be obtained during the post-impact velocity regime. This suggests even with further expenditures on a more advanced laser obscuration system, reasonable post-impact velocity results could not be obtained.

In light of these results and the importance of obtaining the post-impact velocity, the shotgun test is not recommended for further development. Rather, future efforts to determine high-strain-rate impact response of energetic materials should involve the use of more established test equipment such as the split Hopkinson pressure bars of Ho and Fong (1989) and Lieb (1989). These tests can provide high rate mechanical properties as well as impact sensitivity.

Traditionally, the samples used in Hopkinson bar testing have been nearly the same diameter as the bars, and lubrication is applied to the interfaces. These methods help to ensure one-dimensional wave propagation in the bars. Since presumably smaller energetic material sample sizes are desired (cost, safety, ease of initiation, etc.), this suggests a use for the PVDF gauges. If several gauges were placed both on- and off-axis, a measure of the planarity of the reflected and transmitted waves could be obtained thereby validating or negating the applicability of the Hopkinson bar equations.





**SECTION 6.0**  
**LIST OF PUBLICATIONS AND TECHNICAL REPORTS**

Baker, P.J. (1994), "Drop-weight impact initiation of ammonium perchlorate composite solid rocket propellants," Ph.D. Thesis, Vanderbilt University, Dept. of Mechanical Engineering.

Baker, P.J. and Mellor, A.M. (1992), "Relating sample deformation to observations in the drop weight impact test," AIAA Paper 92-3631; accepted for J. Propuls. Power (1993).

Baker, P.J. and Mellor, A.M. (1992), "Modeling propellant sample deformation in the drop weight impact test," Spring Technical Meeting, Central States Section/The Combustion Institute.

Baker, P.J. and Mellor, A.M. (1993), "Interpreting drop-weight impact results in terms of deformation dependent initiation criteria," pp. 107-112, Structure and Properties of Energetic Materials, Materials Research Society, Pittsburgh.

Baker, P.J. and Mellor, A.M. (1993), "Energetic materials impact initiation mechanisms," prepared for Giassman-70 Symposium (invited).

Baker, P.J. and Mellor, A.M. (1994), "Critical impact initiation energy measurements for AP composite propellants," accepted for AIAA Joint Propulsion Meeting.

Baker, P.J. and Mellor, A.M. (1994), "Critical initiation energy tests on AP composite propellants," accepted for JANNAF Propulsion Systems Hazards Subcommittee Meeting; accepted for IM Technologies Symposium.

Baker, P.J. and Mellor, A.M. (1994), "An analytic model of AP composite propellant behavior in the instrumented drop weight impact test," accepted for JANNAF Propulsion Systems Hazards Subcommittee Meeting.

Baker, P.J., Mellor, A.M. and Coffey, C.S. (1990), "Critical impact initiation energies for three HTPB propellants," AIAA Paper No. 90-2196; J. Propuls. Power 8, 578-586 (1992).

Baker, P.J., Mellor, A.M. and Coffey, C.S. (1991), "The critical impact initiation energy test," Spring Technical Meeting, Central States Section/The Combustion Institute

Baker, P.J., Mellor, A.M. and Isom, K.B. (1991), "Mechanisms for ignition of composite energetic materials," U.S. Army Research Office Workshop on Propellant Ignition Micromechanics, Nashville, TN, June, pp. 1-15.

Barr, E.J. (1992), "Finite element analysis of low velocity impact tests for solid rocket propellants," MS Thesis, Vanderbilt University, Dept. of Mechanical Engineering.

Duffy, K.P. (1993), "Dynamic finite element simulations of the response of solid rocket propellant subjected to impact," MS Thesis, Vanderbilt University, Dept. of Mechanical Engineering.

Duffy, K.P. and Mellor, A.M. (1992), "Numerical modeling of the solid propellant drop weight impact test," Spring Technical Meeting, Central States Section/The Combustion Institute.

Duffy, K.P. and Mellor, A.M. (1992), "Mechanical properties test methods as related to hazards sensitivity of energetic materials," pp. 215-230, JANNAF Structures and Mechanical Behavior Subcommittee Meeting Proceedings, CPIA Publ. 591; AIAA J. Propulsion Power 9, 337-344 (1993).

Duffy, K.P. and Mellor, A.M. (1993), "Finite element modeling of the solid propellant drop weight impact test," Joint Technical Meeting, Central States and Eastern Sections/The Combustion Institute.

Duffy, K.P. and Mellor, A.M. (1993), "Numerical modeling of composite propellant response to drop weight impact," pp. 107-117, JANNAF Structures and Mechanical Behavior Subcommittee Meeting Proceedings, CPIA Publ. 604; J. Energetic Materials 11, 261-292.

Duffy, K.P. and Mellor, A.M. (1993), "A numerical study of drop weight impact testing of solid rocket propellants," accepted for Tenth Symposium (International) on Detonation.

Duffy, K.P., Baker, P.J., Barr, E. and Mellor, A.M. (1991), "Dynamic analysis of drop weight impact rocket propellant ignition," AIAA Paper 91-2193.

Duffy, K.P., Baker, P.J. and Mellor, A.M. (1992), "The high strain rate deformation of composite solid propellant disks," pp. II.11.9-II.11.18, Developments in Theoretical and Applied Mechanics, Vol. XVI, Univ. Tennessee Space Inst., Tullahoma.

Mann, D.M. and Mellor, A.M. (1991), "Progress towards a unified view of energetic material hazards," Fall Technical Meeting, Eastern Section/The Combustion Institute (invited).

Mellor, A.M., Wiegand, D.A. and Isom, K.B. (1993), "Hot spot histories in energetic materials," pp. 293-298, Structure and Properties of Energetic Materials, Materials Research Society, Pittsburgh; submitted to Combust. Flame, (1993).

## SECTION 7.0

### LIST OF PARTICIPATING SCIENTIFIC PERSONNEL AND DEGREES AWARDED

Mellor, A.M., Principal Investigator

Coffey, C.S., Naval Surface Warfare Center, Co-Principal Investigator

Francis, E.C., United Technologies Chemical Systems, Co-Principal Investigator (First two years only)

#### Graduate Students

Baker, P.J., Ph.D. (8/94)

Duffy, K.P., B.E. (5/91); M.S. (5/93); Ph.D. in progress

Barr, E.J., M.S. (12/92)

#### Undergraduate Students (all awarded B.E. degrees, most with honors)

Barnes, J.C. (5/94)

Campbell, T.A. (5/91)

Everson, D.G. (5/93)

Jeffries, C.L. (5/91)

Miller, J.E. (5/94)

Seay, J.E. (5/93)



SECTION 8.0  
LIST OF REPORTABLE INVENTIONS

Not applicable.



## SECTION 9.0

### REFERENCES

- Baker, P.J. (1994), "Drop-weight impact initiation of ammonium perchlorate composite solid rocket propellants," Ph.D. Thesis, Vanderbilt University, Dept. of Mechanical Engineering.
- Baker, P.J. and Mellor, A.M. (1992), "Relating sample deformation to observations in the drop weight impact test," AIAA Paper 92-3631; accepted for J. Propuls. Power.
- Baker, P.J., Mellor, A.M. and Coffey, C.S. (1990), "Critical impact initiation energies for three HTPB propellants," AIAA Paper No. 90-2196; J. Propuls. Power 8, 578-586.
- Baker, P.J., Mellor, A.M. and Coffey, C.S. (1991), "The critical impact initiation energy test," Central States Section/Combustion Institute, Nashville, TN, 233-239.
- Coffey, C.S. and DeVost, V.F. (1986), "Drop weight impact machines - a review of recent progress," JANNAF Propulsion Systems Hazards Subcommittee Meeting, CPIA Publication 446, Vol. I, pp. 527-531.
- Coffey, C.S., DeVost, V.F. and Yergey, B.A. (1986), "Critical initiation energy in at least some propellants and explosives subjected to impact," JANNAF Propulsion Systems Hazards Subcommittee Meeting, CPIA Publication 446, Vol. I, pp. 579-585.
- Coffey, C.S., Devost, V.V., and Woody, D.L. (1989), "Towards developing the capability to predict the hazard response of energetic materials subjected to impact," Ninth Symposium (International) on Detonation, OCNR 113291-7, Vol. II, pp. 1243-1252.
- Dobratz, B.M. and Crawford, P.C. (1985), "LLNL Explosives Handbook," Univ. of Cal., Lawrence Livermore National Laboratory, Report UCRL-52997, Change 2.
- Duffy, K.P. (1993), "Dynamic finite element simulations of the response of solid rocket propellant subjected to impact," MS Thesis, Vanderbilt University, Dept. of Mechanical Engineering.
- Durst, I. and Stevenson, W.H. (1977), "The influence of Gaussian beam properties on laser Doppler signals," Sonderforschungsbereich 80, Universität Karlsruhe.
- Everson, D.G. and Seay, J.E. (1992), "Proposed shotgun impact test design," Spring Technical Report, Honors Program, Vanderbilt University, Dept. of Mechanical Engineering.
- Follanste, P.S. and Frantz, C. (1983), "Wave propagation in the split Hopkinson pressure bar," J. Engineering Materials and Technology 105, 61-66.
- Gould, R.A. (1980), "Progress report of JANNAF panel on shotgun/relative quickness testing," JANNAF Propulsion Systems Hazards Subcommittee Meeting, CPIA Publication 330, Vol. I, pp. 289-301.
- Hallquist, J.O. (1978), "A numerical treatment of sliding interfaces and impact," Computational Techniques for Interface Problems, Park, K. and Gurtling, P., Eds., A.M.D., Vol 30, ASME United Engineering Center, NY.
- Hallquist, J.O. (1982), "User's manual for DYNA2D," Univ. of Cal., Lawrence Livermore National Laboratory, Report UCID-18756, Rev. 1.



Ho, S.Y. and Fong, C.W. (1989), "Relationship between impact ignition sensitivity and kinetics of the thermal decomposition of solid propellants," Combust. Flame 75, 139-151.

Ho, S.Y., Fong, C.W. and Hamshire, B.L. (1989), "Assessment of the response of rocket propellants to high velocity projectile impact using small-scale laboratory tests," Combust. Flame 77, 395-404.

Johnson, D. (1992, 1994), KTECH Corp., Personal Communication.

Jensen, R.C., Blommer, E.J. and Brown, B. (1981), "An instrumented shotgun facility to study impact initiated explosive reactions," Seventh Symposium (International) on Detonation, NSWC MP 82-334, pp. 299-307.

Lieb, R.J. (1989), "The mechanical response of M30, JA2 and XM39 gun propellants to high-rate deformation," Technical Report BRL-TR-3023.

Mallard, P. (1993), Measurements Group, Inc., Personal Communication.

Maykut, A. (1991), "Insensitive munitions requirements and their impact on rocket motor Design," Invited Paper, Central States Section/Combustion Institute, Nashville, TN.

Mellor, A.M., Boggs, T.L., Covino, J., Dickenson, C.W., Dreitzler, D., Thorn, L.B., Frey, R.B., Gibson, P.W., Roe, W.E., Kirshenbaum, M. and Mann, D.M. (1988), "Hazard initiation in solid rocket and gun propellants and explosives," Progress in Energy & Combustion Science, Vol. 14, No. 3, pp. 213-220.

Pitz, R.W. (1993), Vanderbilt University, Personal Communication.

Roth, J. (1975), "Impact, initiation of explosion by," in Encyclopedia of Explosives and Related Items, PATR 2700, Vol. 7, pp. I 35 - I 55.

Smith, W.F. (1986), Principles of Materials Science & Engineering, McGraw-Hill Book Company, pp. 367-370.

Spindler-Hoyer Co. (1993, 1994), Personal Communication.

## APPENDIX A

### TEST BAY DIMENSIONS

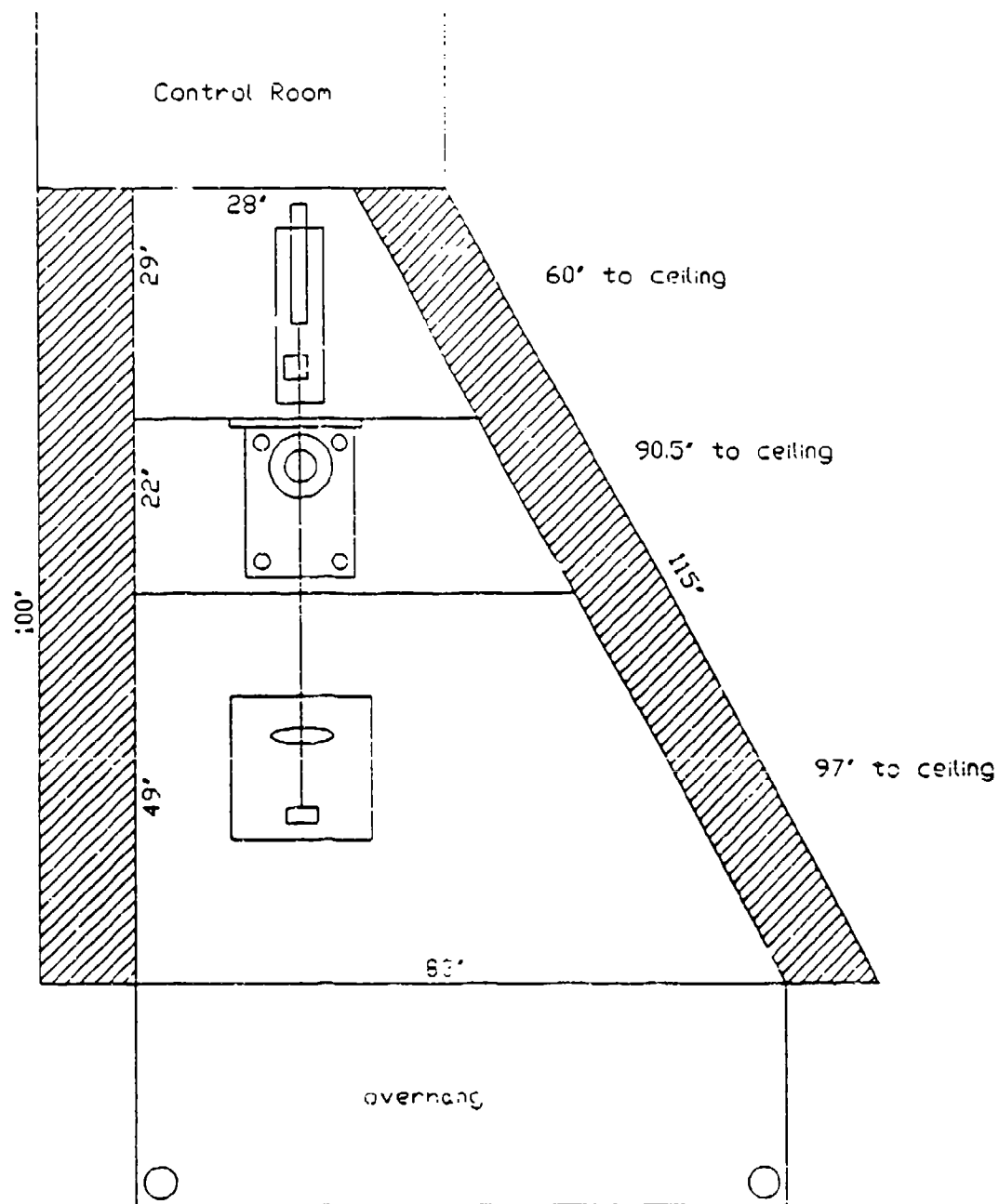


Figure A-1. Diagram of test bay for shotgun impact. All dimensions in inches.

**APPENDIX B**  
**DETERMINATION OF FACE LENGTH AND CENTERLINE BEAM SPACING**

Referring to Fig. B-1 for a 1.59 mm thick spacer ( $t$ ) at incidence angle ( $\theta$ ) of  $35^\circ$ :

The face length ( $L$ ) is:

$$L = t / \cos \theta = 1.59 / \cos 35 = 1.94 \text{ mm} \quad (\text{B.1})$$

For the top triangle:

$$\tan 70 = 1.94/y, y = 0.706 \text{ mm} \quad (\text{B.2})$$

For the middle triangle and law of sines:

$$\sin 35 / 0.706 = \sin 110 / z, z = 1.157 \text{ mm} \quad (\text{B.3})$$

For the bottom triangle:

$$\sin 35 = x / 1.157, x = 0.6638 \text{ mm} \quad (\text{B.4})$$

The centerline beam spacing (BS) is therefore:

$$BS = L + x = 1.94 + 0.6638 = 2.60 \text{ mm} \quad (\text{B.5})$$

A final compact form for BS in terms of  $\theta$  and  $t$  is:

$$BS = t / \cos \theta + t \times \sin (180 - 2\theta) / (\tan 2\theta \times \cos \theta) \quad (\text{B.6})$$

Equations (B.1) and (B.6) are graphed in Fig. 5.15.

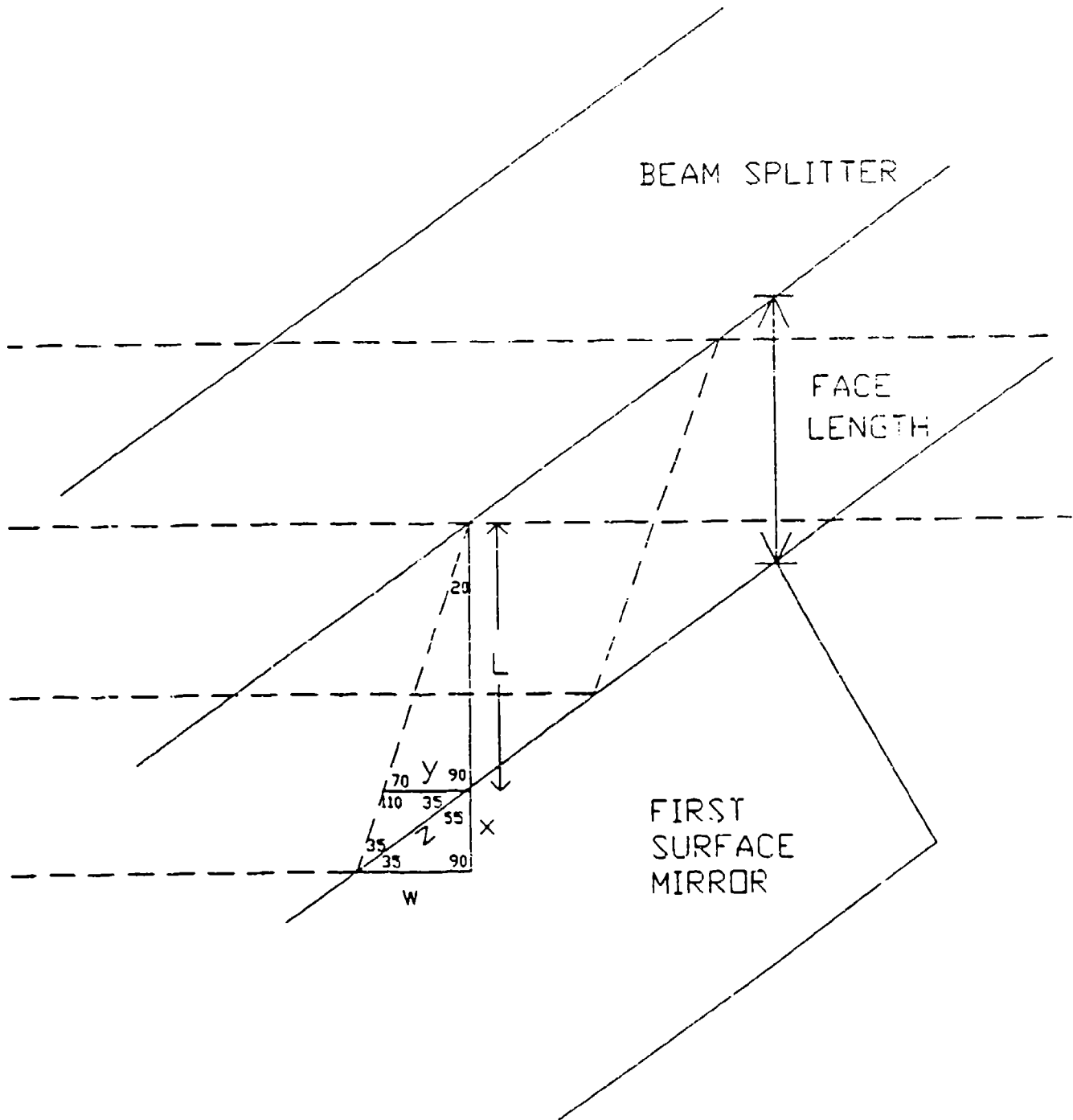


Figure B-1. Close-up of optics indicating relevant lengths and angles for determining face length and centerline beam spacing.

APPENDIX C  
STRESS AND REACTION HISTORIES

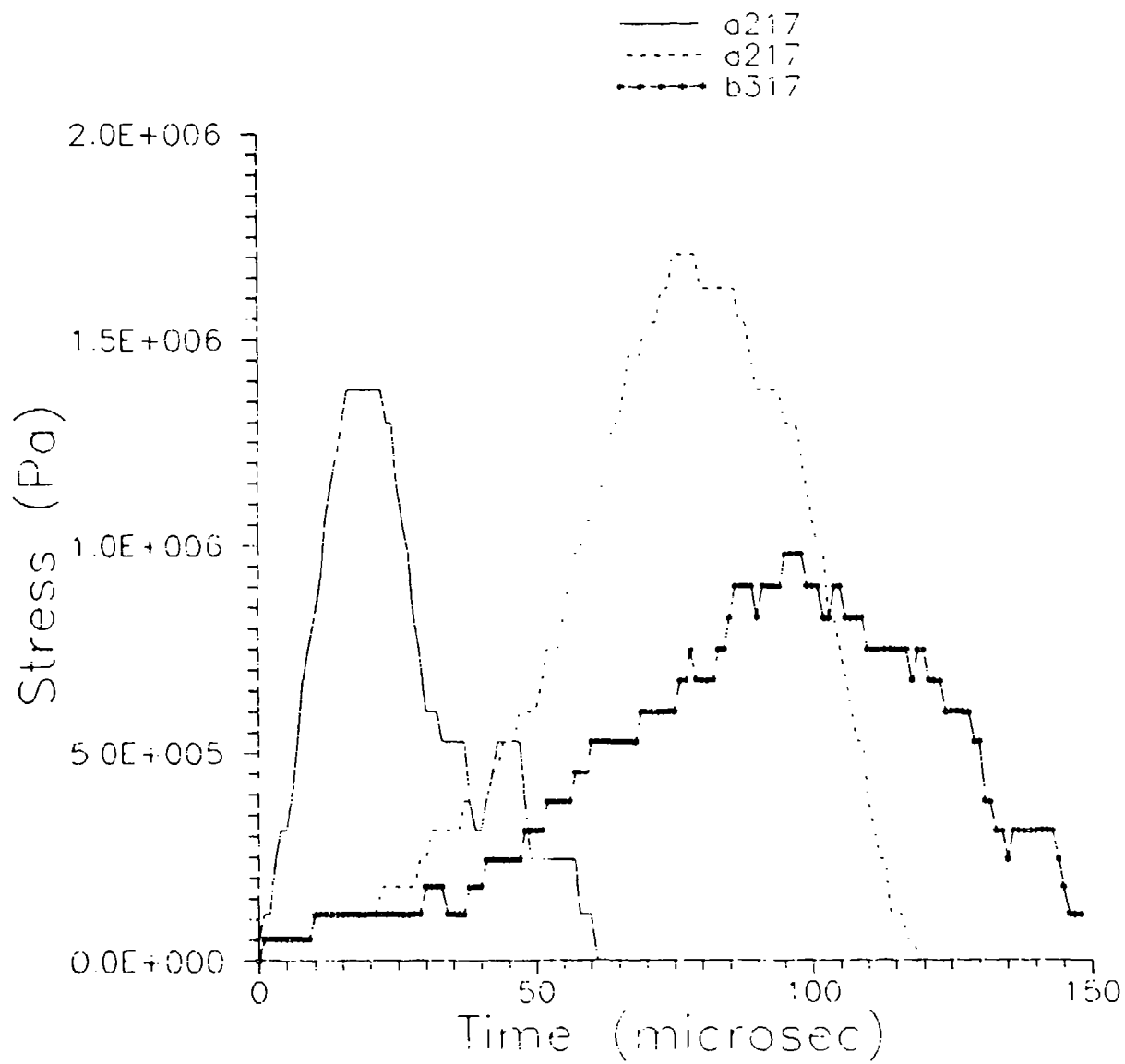


Figure C-1. Stress histories for inert samples at  $\approx 150$  m/s.

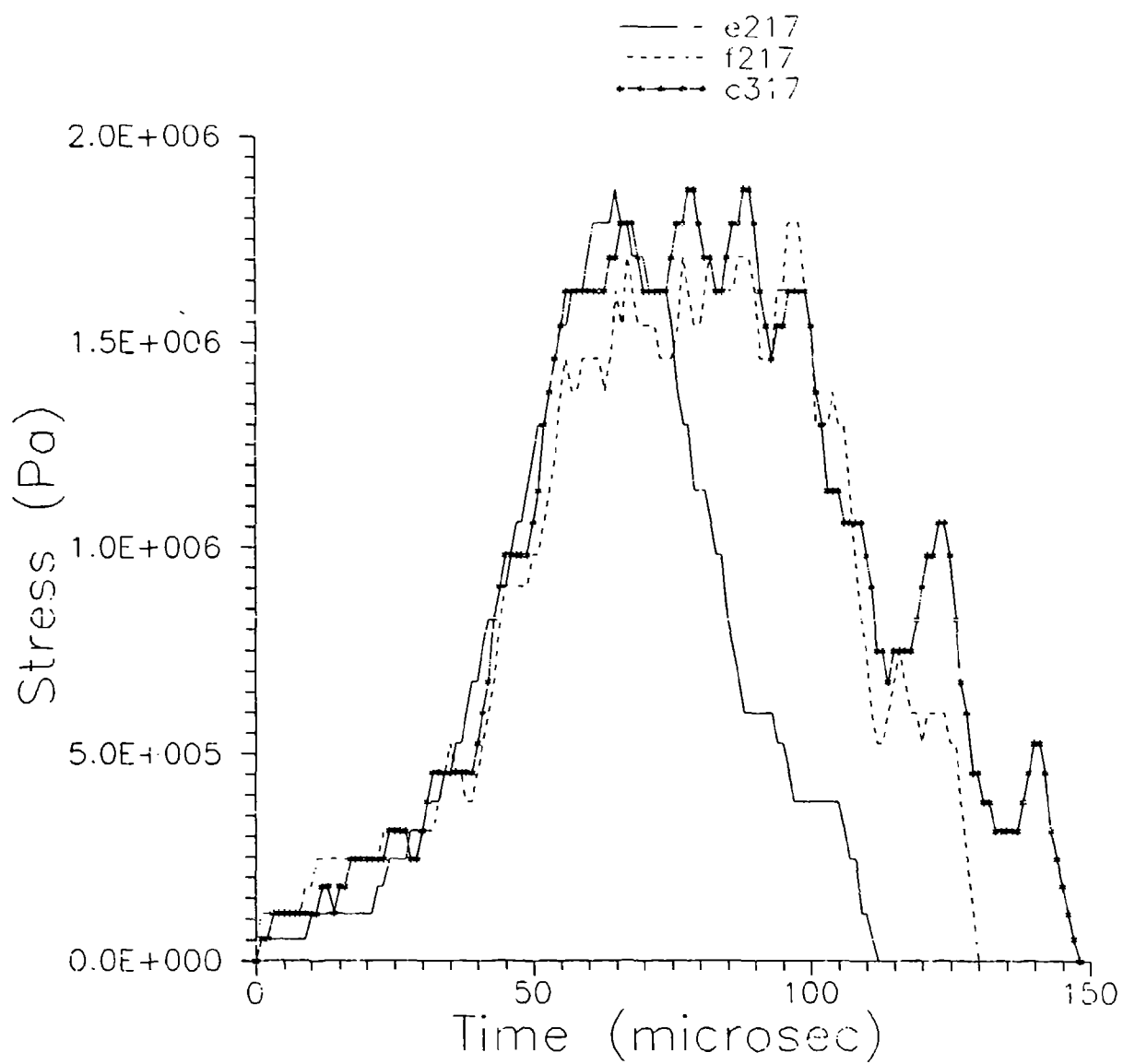


Figure C-2. Stress histories for inert samples at  $\approx 200$  m/s.



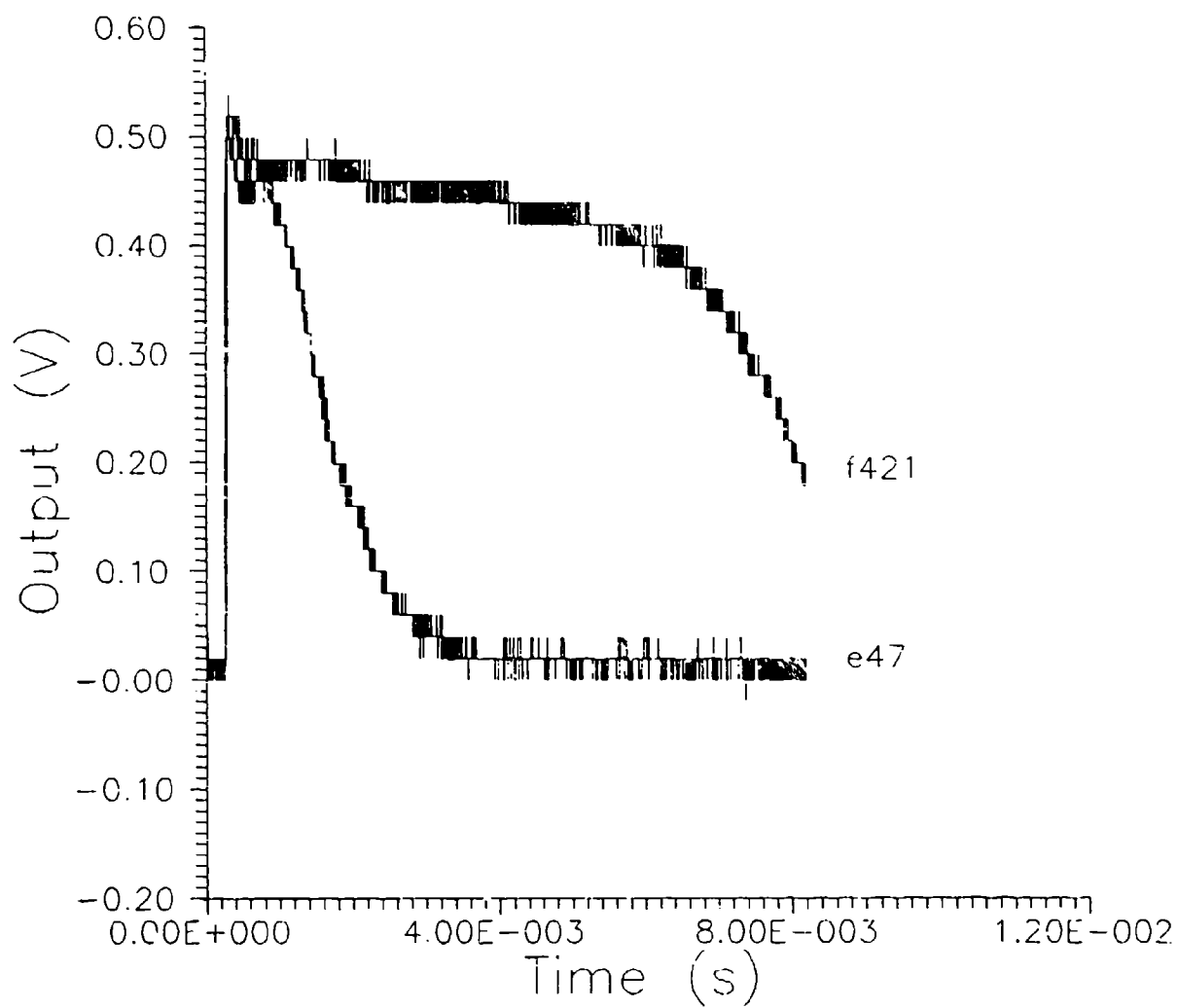


Figure C-3. Light traces for Arcadene-360 samples at  $\approx 150$  m/s.

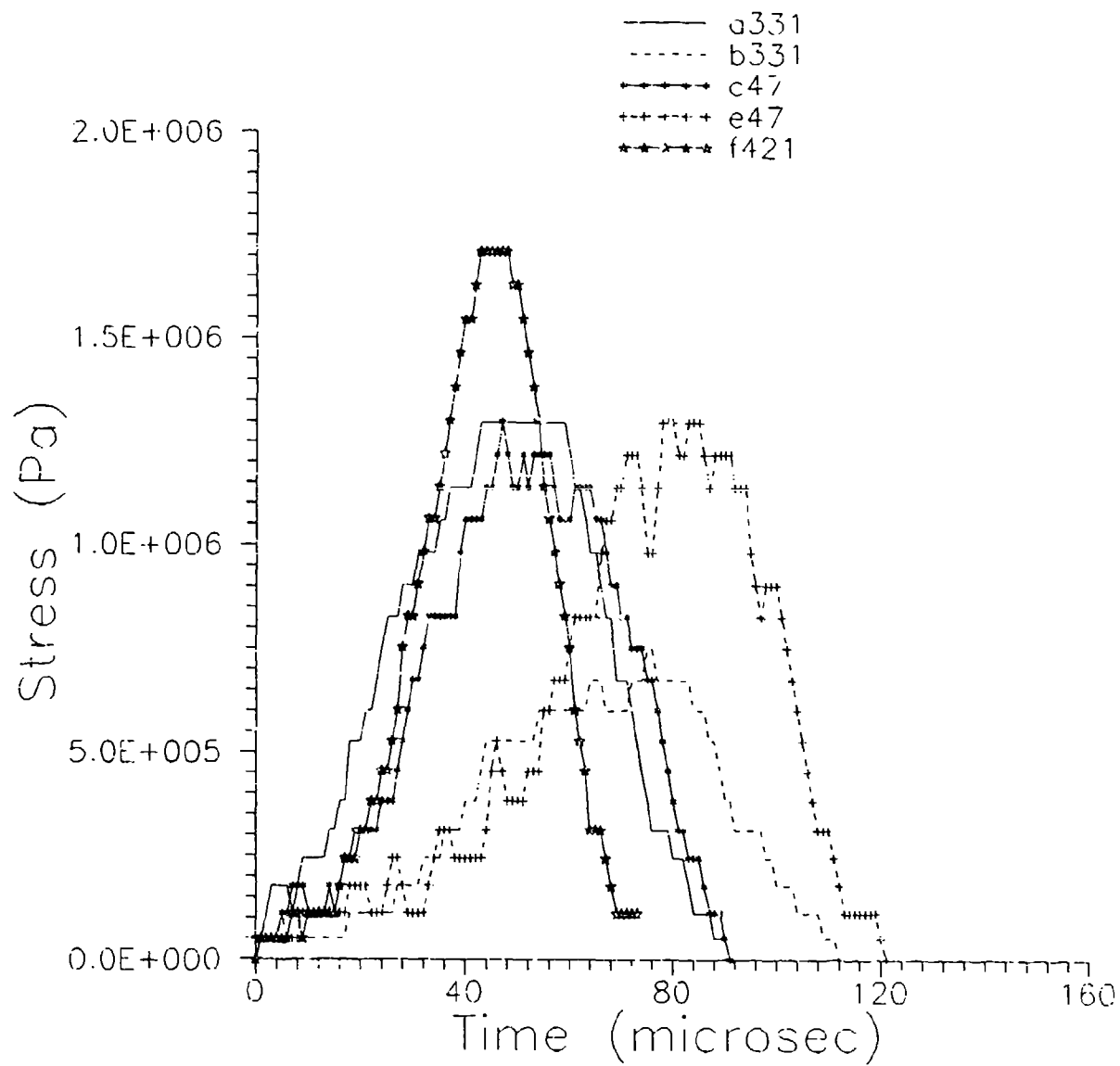


Figure C-4. Stress histories for Arcadene-360 samples at  $\approx 150$  m/s.

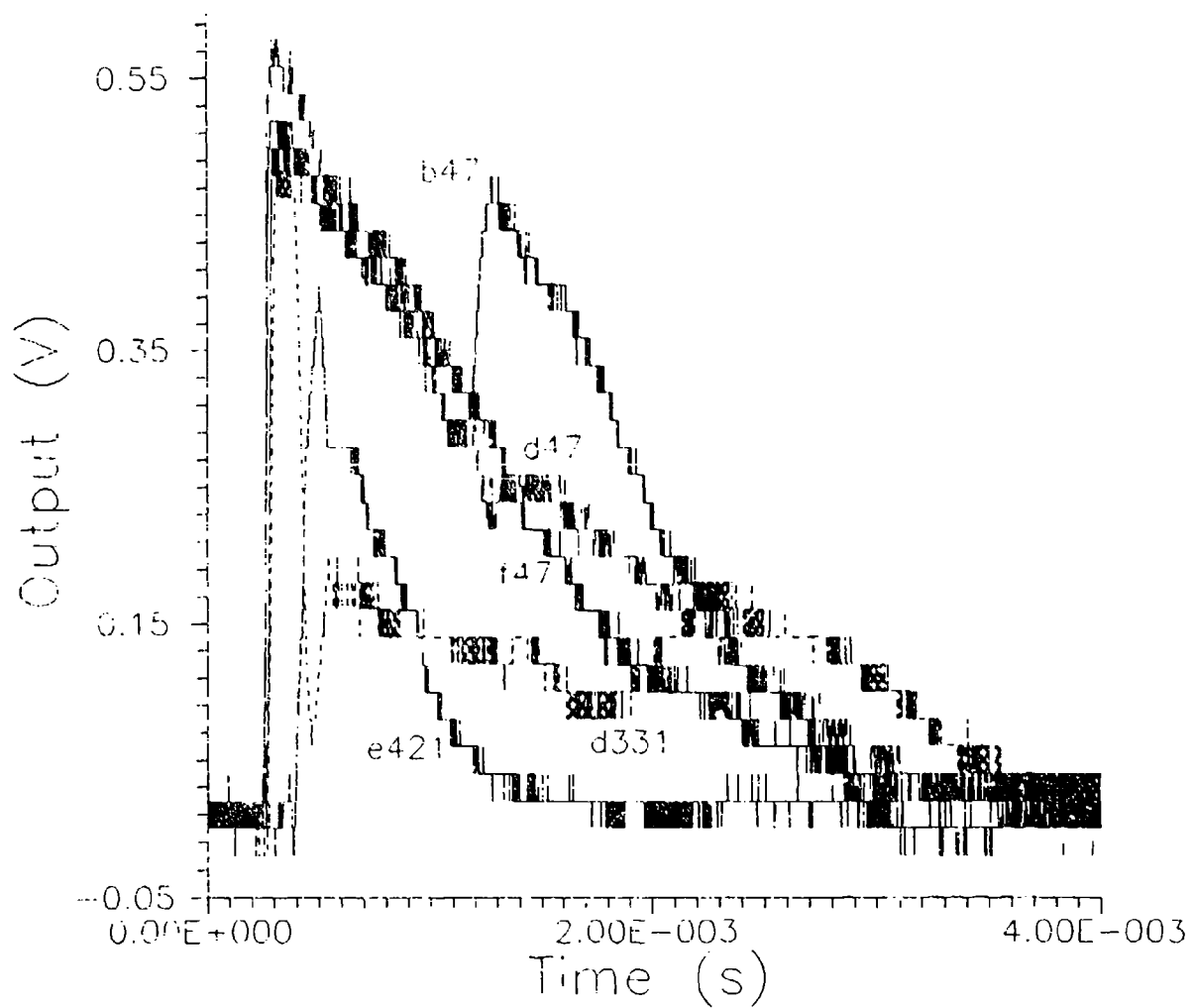


Figure C-5. Light traces for Arcadene-360 samples at  $\approx 260$  m/s.

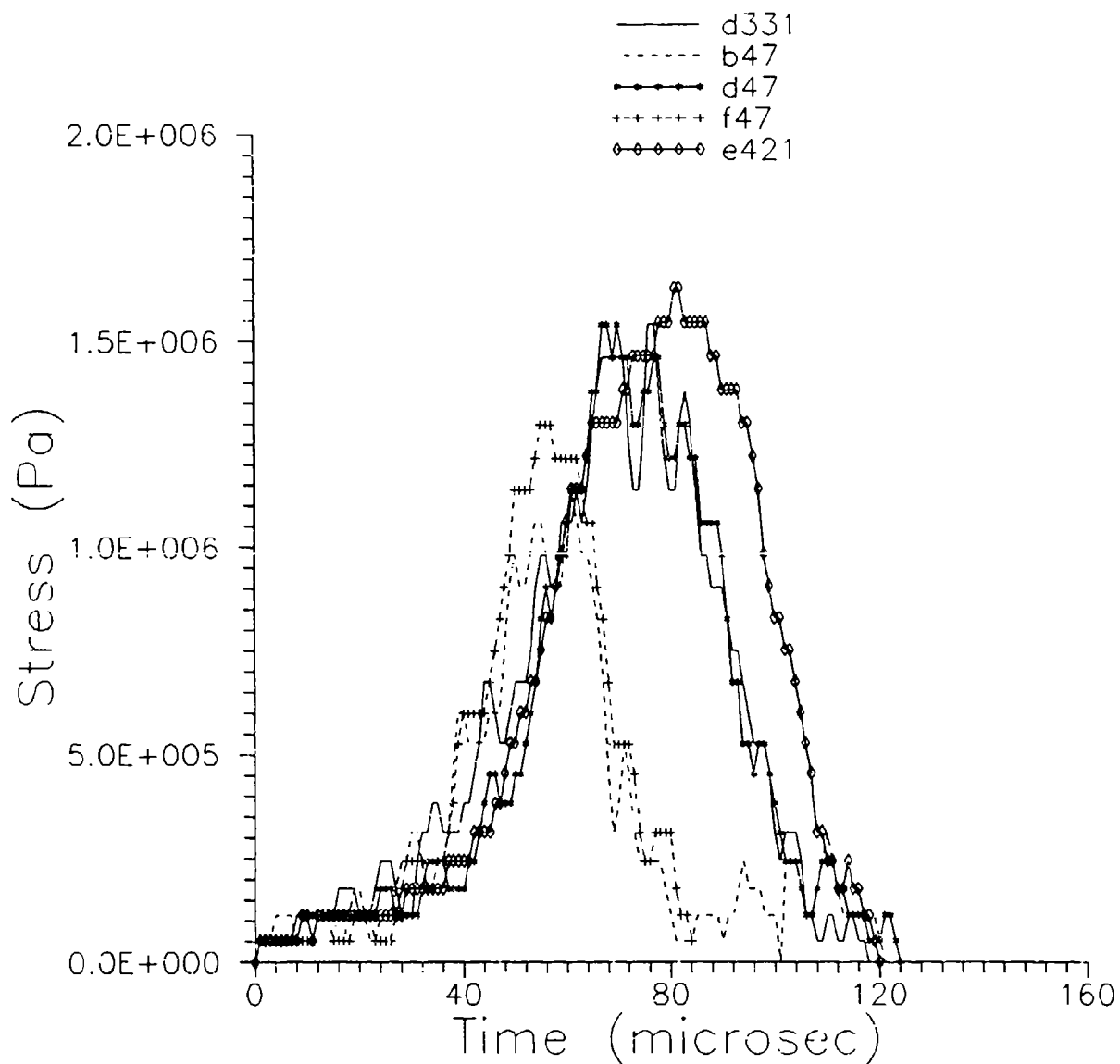


Figure C-6. Stress histories for Arcadene-360 samples at  $\approx 200$  m/s.

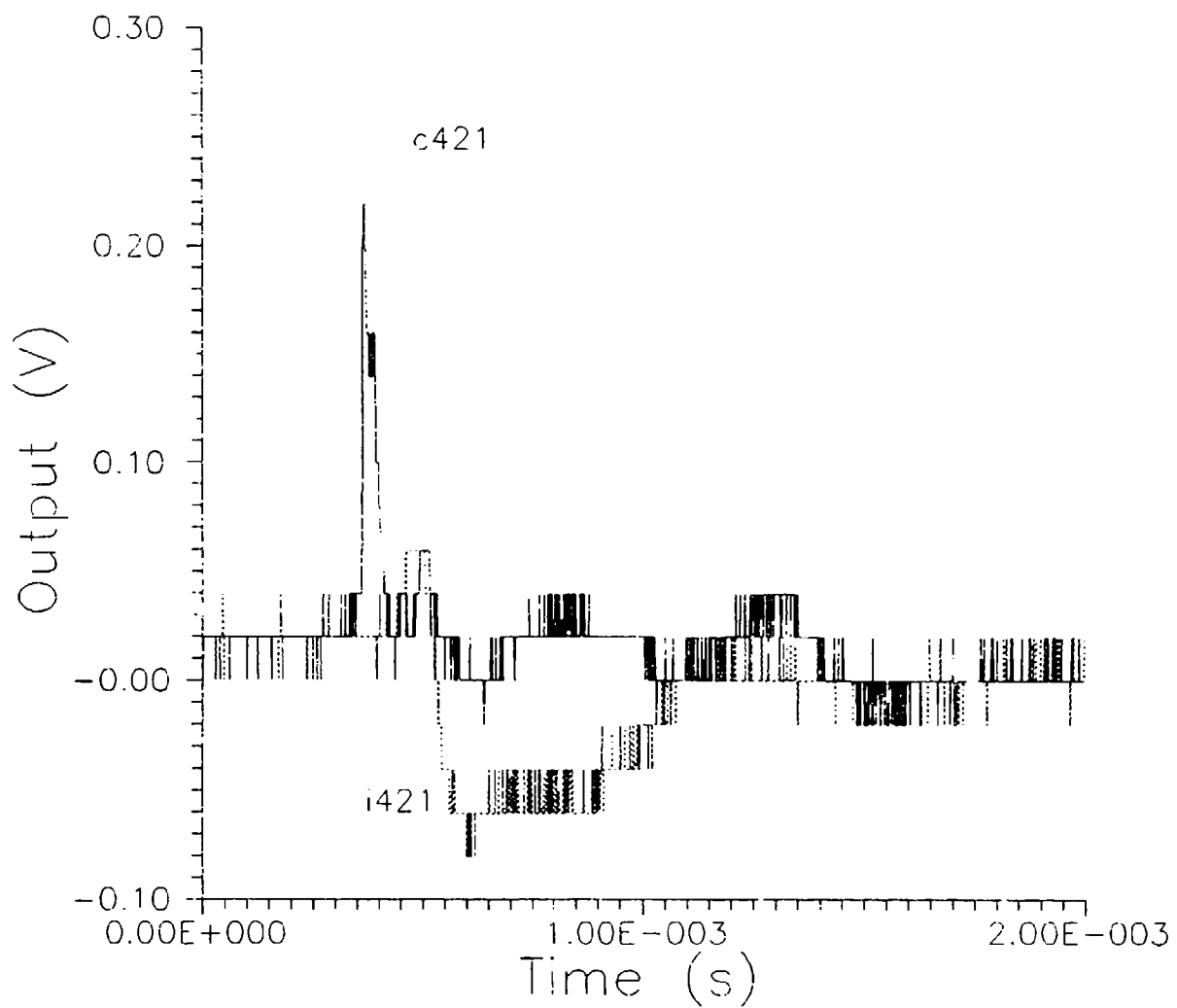


Figure C-7. Light traces for P3 samples at  $\approx 150$  m/s.

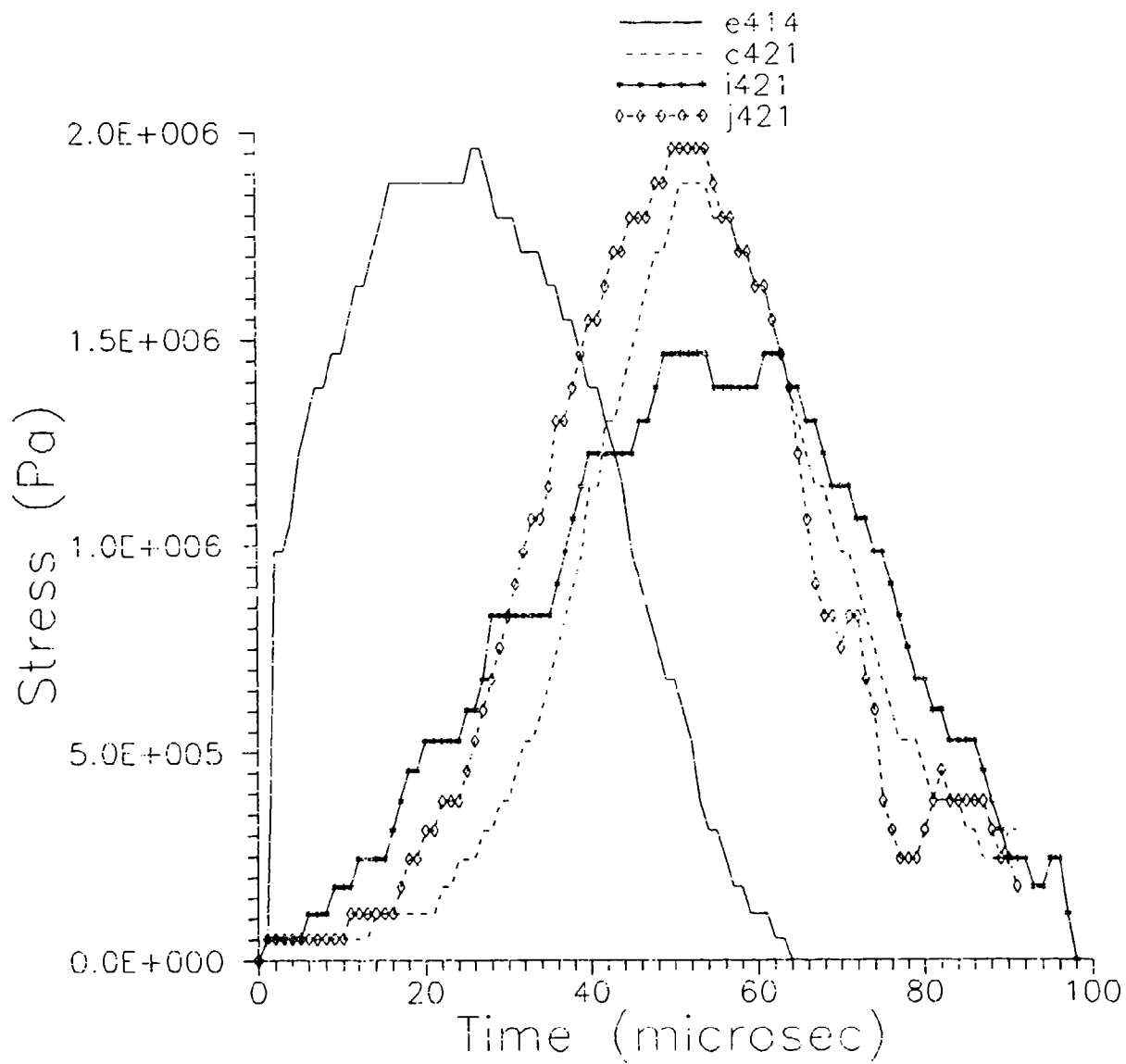


Figure C-8. Stress histories for P3 samples at  $\approx 150$  m/s.

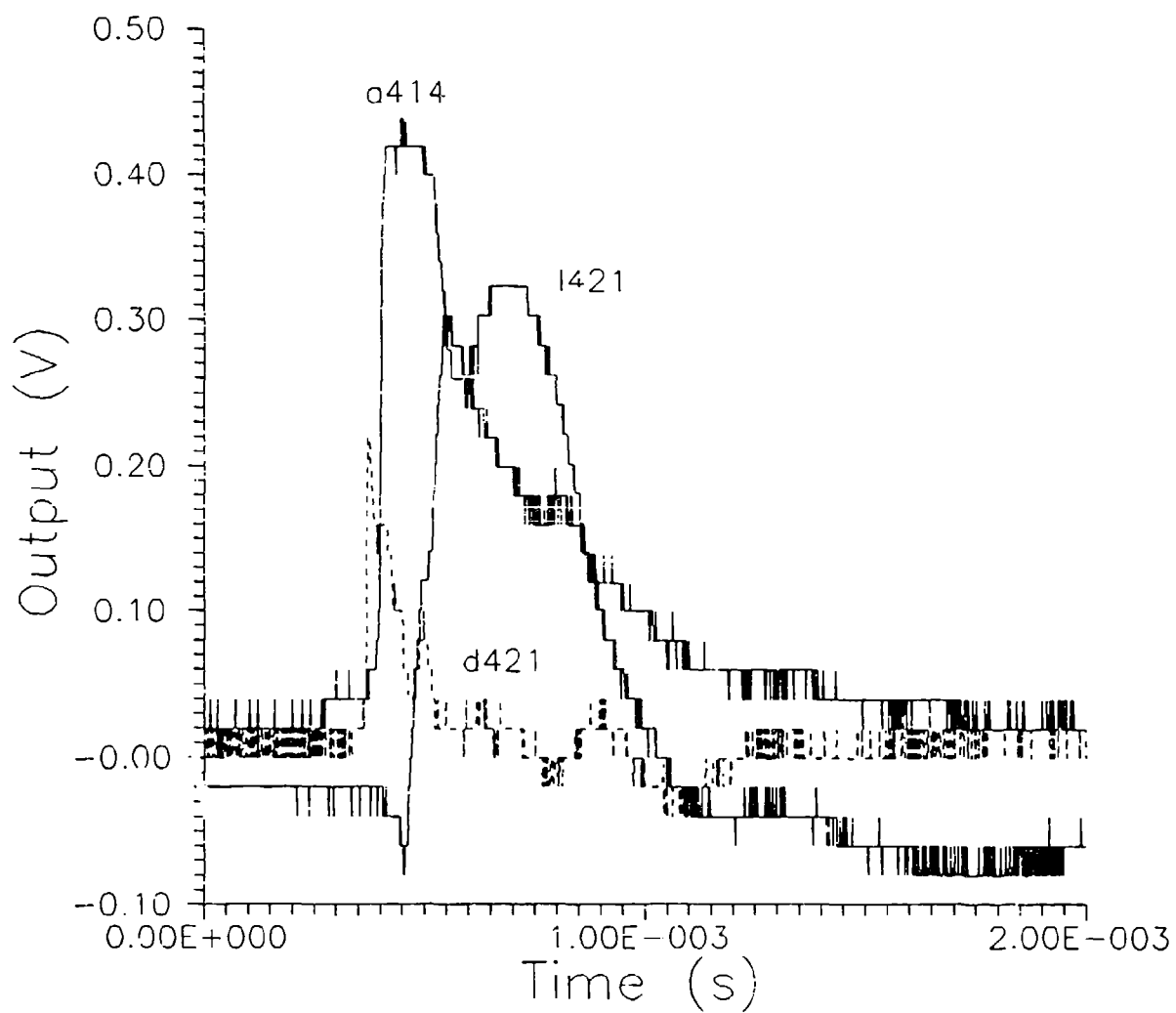


Figure C-9. Light traces for P3 samples at  $\approx 200$  m/s.

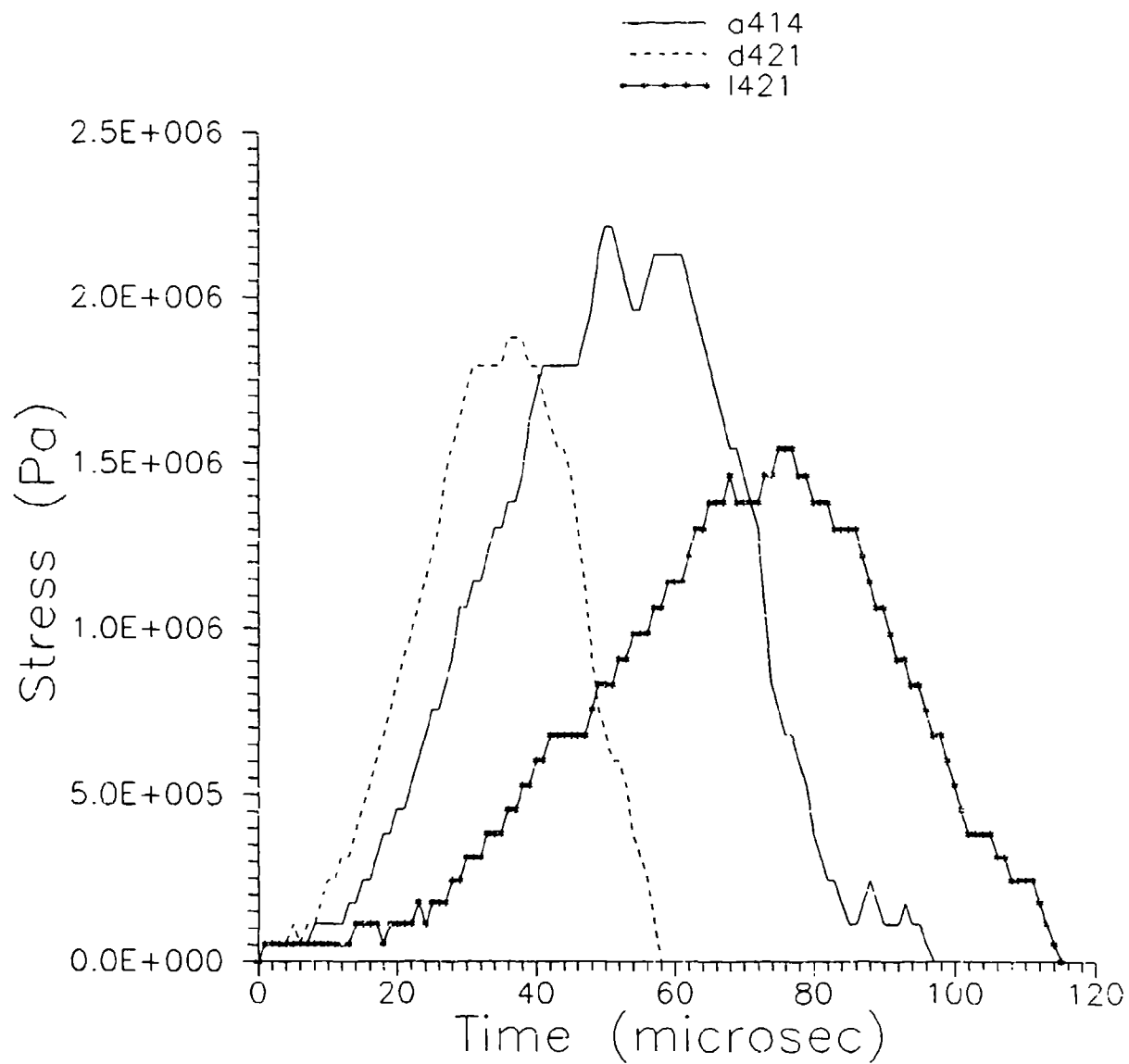


Figure C-10. Stress histories for P3 samples at  $\approx 200$  m/s.



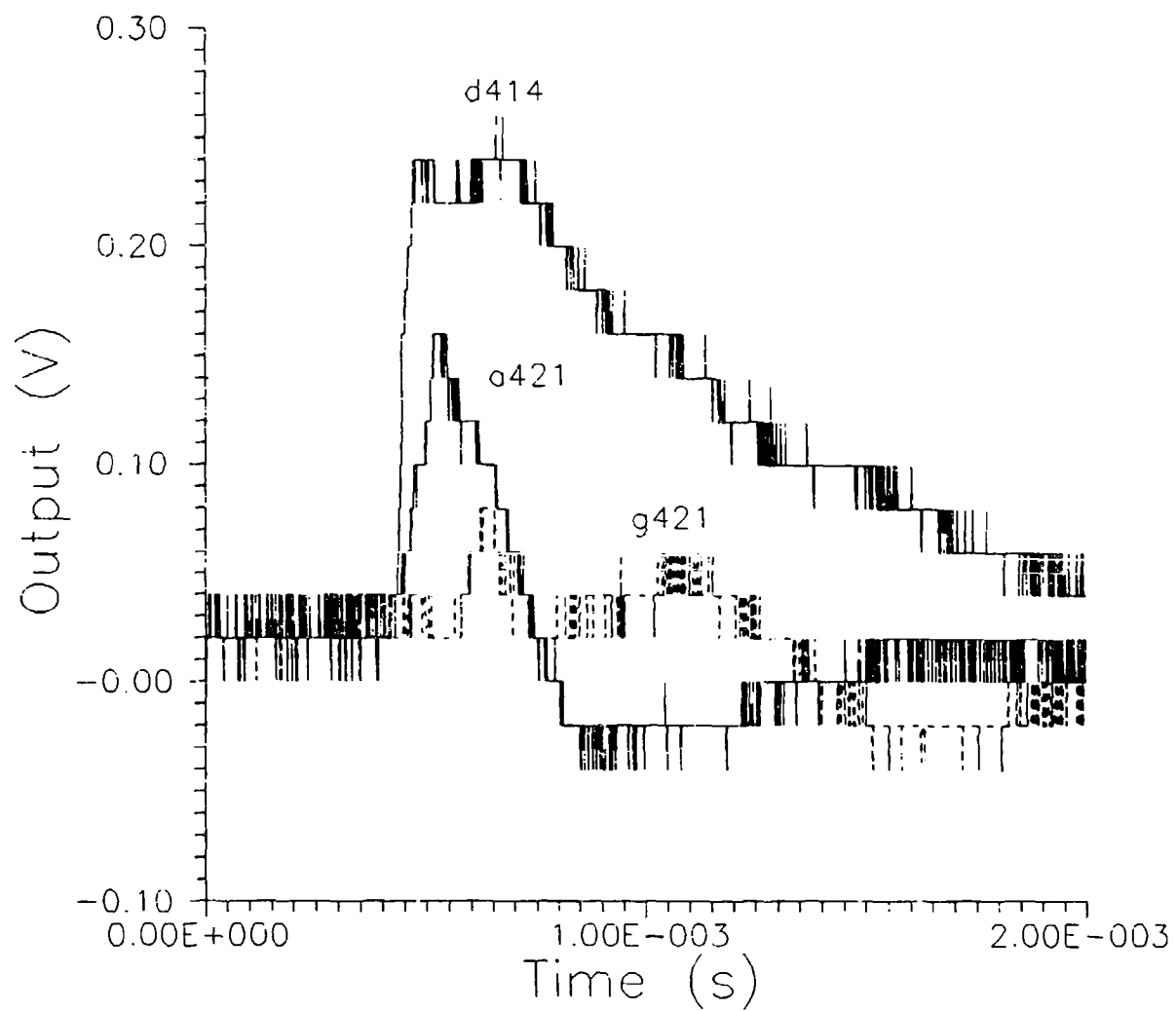


Figure C-11. Light traces for P8 samples at  $\approx 150$  m/s.

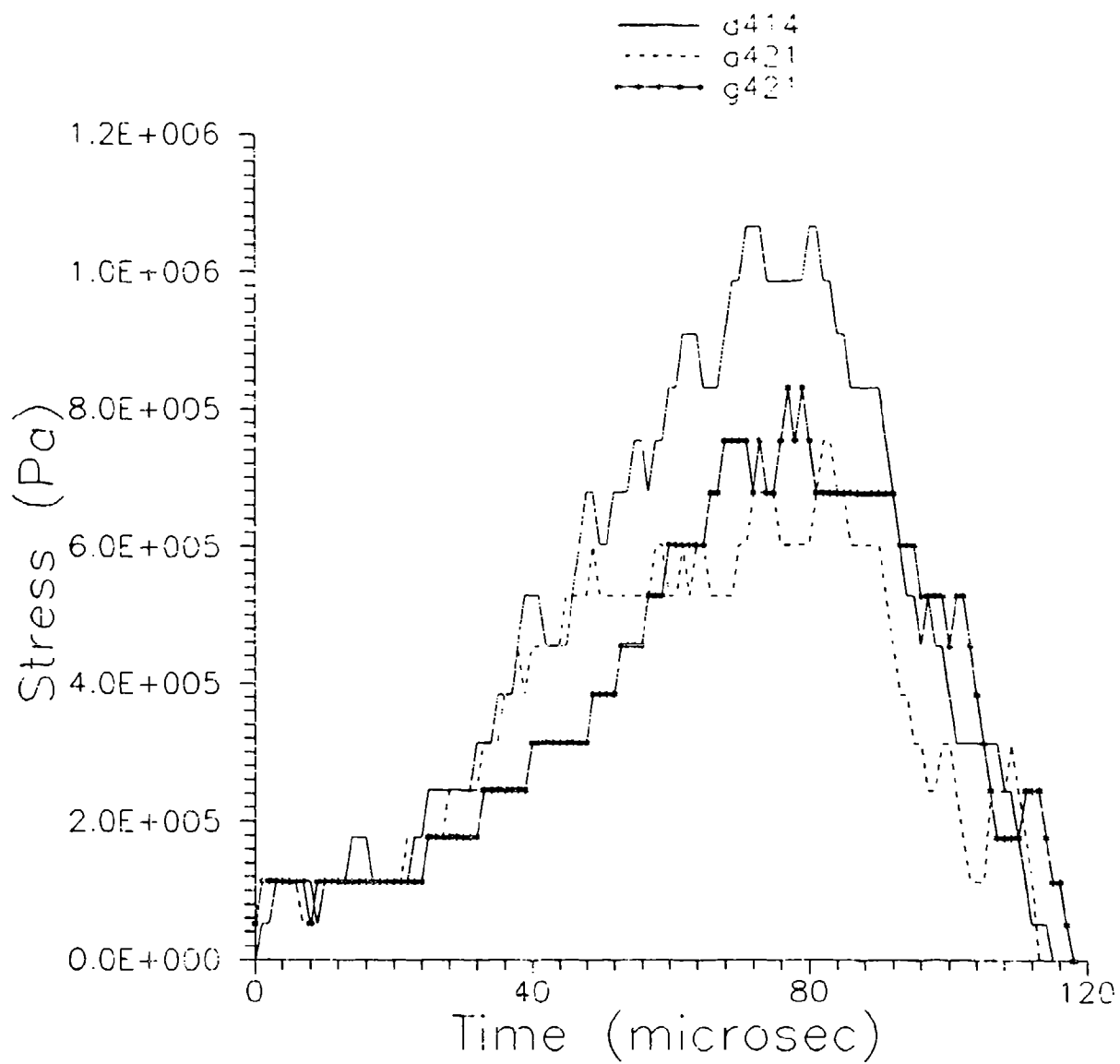


Figure C-12. Stress histories for P8 samples at  $\approx 150$  m/s.

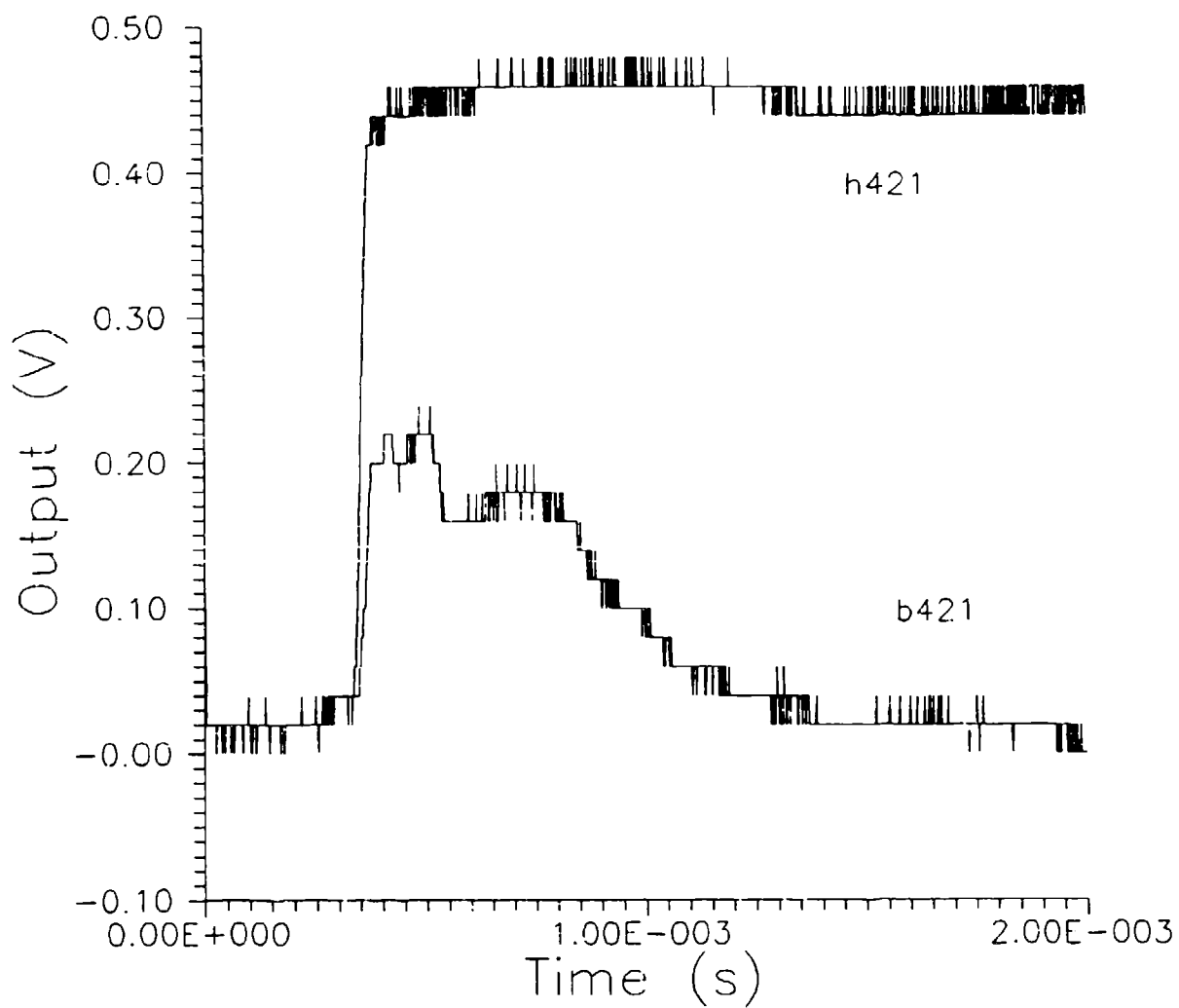


Figure C-13. Light traces for P8 samples at  $\approx 200$  m/s.

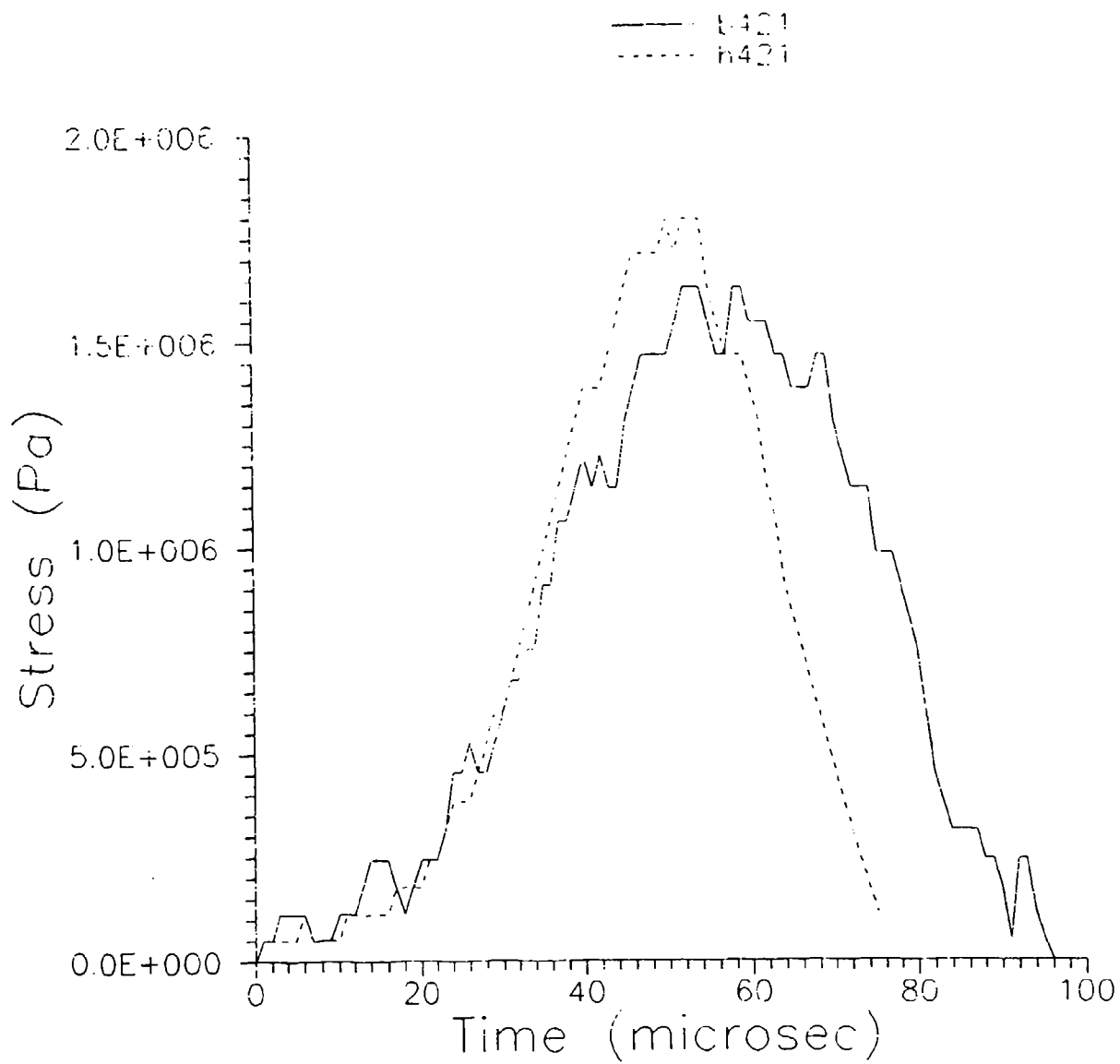


Figure C-14. Stress histories for P8 samples at  $\approx 200$  m/s.



# **APPENDIX D** **DERIVATION OF VELOCITY FROM STRESS HISTORY**

From Eq. (5.9)

$$P_p = 0.95 P_A = 0.95 \sigma(t)_A \quad (D.1)$$

Since stress equals force per unit area and from Newton's Law:

$$0.95 \sigma(t)_A = 0.95 F_p / A_p = m_p \times a_p / A_p \quad (D.2)$$

Solving for the acceleration:

$$a_p = 0.95 \sigma(t)_A A_p / m_p \quad (D.3)$$

Integrating this expression over time results in velocity:

$$v_p(t) = \int_0^t a_p dt = 0.95 (A_p / m_p) \int_0^t \sigma(t)_A dt \quad (D.4)$$

The change in projectile kinetic energy is:

$$\Delta E_{p,k} = 1/2 m_p (v_p^2(t) - v_p^2(0)) \quad (D.5)$$

From Baker and Mellor (1992) the change in sample kinetic energy is:

$$\Delta E_{s,k} = 1/2 m_s [v_p^2(t)(0.333 + 0.125(r_s^2(0) \times T_s(0)/T_s^3(t)))] \quad (D.6)$$

where  $T_s(0)$  and  $T_s(t)$  are the initial (6 or 12.7 mm) and current sample lengths, and  $r_s(0)$  is the initial sample radius (5 mm).

To determine the current sample length the incompressible assumption is invoked to define the initial sample length:

$$T_s(0) = Vol_s / \pi r_s^2(0) \quad (D.7)$$

and the current sample length is therefore:

$$T_s(t) = T_s(0) - v_p(t) \times t \quad (D.8)$$



## REPORT DOCUMENTATION PAGE

Form Approved

OMB No. 0704-0188

Public reporting burden for this collection of information is estimated to average 1 hour per response, including the time for reviewing instructions, searching existing data sources, gathering and maintaining the data needed, and completing and reviewing the collection of information. Send comments regarding this burden estimate or any other aspect of this collection of information, including suggestions for reducing this burden, to Washington Headquarters Services, Directorate for Information Operations and Reports, 1215 Jefferson Davis Highway, Suite 1204, Arlington, VA 22202-4302, and to the Office of Management and Budget, Paperwork Reduction Project (0704-0188), Washington, DC 20503.

1. AGENCY USE ONLY (Leave blank)		2. REPORT DATE June 30, 1994		3. REPORT TYPE AND DATES COVERED	
4. TITLE AND SUBTITLE  Shotgun/Drop-Weight Initiation of Energetic Materials Final Report				5. FUNDING NUMBERS	
6. AUTHOR(S)  K.P. Duffy, J.E. Miller and A.M. Mellor					
7. PERFORMING ORGANIZATION NAME(S) AND ADDRESS(ES)  Vanderbilt University Box 1592, Station B Nashville, TN 37235-1592				8. PERFORMING ORGANIZATION REPORT NUMBER	
9. SPONSORING/MONITORING AGENCY NAME(S) AND ADDRESS(ES)  U.S. Army Research Office P.O. Box 12211 Research Triangle Park, NC 27709-2211				10. SPONSORING/MONITORING AGENCY REPORT NUMBER	
11. SUPPLEMENTARY NOTES The views, opinions and/or findings contained in this report are those of the author(s) and should not be construed as an official Department of the Army position, policy, or decision, unless so designated by other documentation.					
12a. DISTRIBUTION/AVAILABILITY STATEMENT  Approved for public release; distribution unlimited.				12b. DISTRIBUTION CODE	
13. ABSTRACT (Maximum 200 words)  Shotgun impact tests were performed by firing plexiglas projectiles at 6 mm long by 12 mm diameter propellant samples at 150 and 200 m/s impact velocities. Three different HTPB/AP propellants were tested: an Army fielded munition and two research propellants. The feasibility of a new technique, laser obscuration, was evaluated for measuring the pre- and post-impact projectile velocity history. Using less than ideal optical components, the present system is able to measure the pre-impact velocity but does not provide adequate resolution of the crucial post-impact velocity. The limits of even state-of-the-art optical components coupled with the small length of the sample (6 mm) precludes using this type of laser system for future testing. A light detection system provided severity of and time to reaction information for the three propellants tested. The performance of PVDF stress gauges for determining critical energy was marginal with calculated values that qualitatively support lower velocity drop-weight results. For two of the three propellants, critical energy density decreased at the higher shotgun impact velocities as expected. Attempts were made to correlate the go/no go and severity of reaction response to several stress gauge output parameters, but due to the limited data obtained in this one-year program, no strong correlations were obtained.					
14. SUBJECT TERMS Shotgun impact, HTPB/AP propellants, critical energy, laser obscuration, PVDF stress gauge				15. NUMBER OF PAGES 113	
				16. PRICE CODE	
17. SECURITY CLASSIFICATION OF REPORT UNCLASSIFIED	18. SECURITY CLASSIFICATION OF THIS PAGE UNCLASSIFIED	19. SECURITY CLASSIFICATION OF ABSTRACT UNCLASSIFIED	20. LIMITATION OF ABSTRACT UL		